The Thermo-tectonic History of a Gneiss-Amphibolite Sequence, Iddefjord, Østfold

Bjørn Magnus Mowinckel Nilsen Narum

Master Thesis
Structural Geology and Tectonics
60 credits

Department of Geosciences
Faculty of Mathematics and Natural Sciences

UNIVERSITY OF OSLO

December 2016

UiO : Department of Geosciences
University of Oslo

The Thermo-tectonic History of a Gneiss-Amphibolite Sequence, Iddefjord, Østfold

Bjørn Magnus Mowinckel Nilsen Narum

Master Thesis, Autumn 2016

Supervisors: Prof. Fernando Corfu (UiO), Prof. Roy Helge Gabrielsen (UiO)

This work is published digitally through DUO - Digitale Utgivelser ved UiO

http://www.duo.uio.no/

Front page: Wire-cut outcrop of foliated biotite-gneiss, seen at Remmen, Halden, Østfold.

Abstract

The Iddefjord terrane of the Sveconorwegian Orogen, consists of rocks formed in an arc setting, mainly between 1650 and 1550 Ma (Åhäll and Connelly 2008), and affected by Sveconorwegian deformation and metamorphosis in varying degrees. At Remmen, near Halden (Østfold), 150 meters of diamond-wire-cut outcrops have been investigated. The study is based on traditional structural field analysis and utilizes U-Pb dating of zircon, monazite, titanite and rutile by ID-TIMS. The thermo-tectonic evolution, which includes plastic and brittle compressional and extensional events, was investigated. The Remmen outcrops display a sequence of biotite-gneiss, garnet amphibolite and several generations of pegmatite veins. The geometric and time relations between the biotite-gneiss and the garnet-amphibolite are prominent in the outcrops (see figure). In one area (C), the amphibolite consists of rectangular homogeneous boudins in the semi-chaotic foliated gneiss. In other parts of the outcrops (A), the amphibolite is migmatitic with internal foliated slivers of leucosome, defining lens-shaped bodies. The foliation in the gneiss dips towards the north, with large variance in the vicinity of the amphibolites, as stress shadows form on the sides of the boudins. This plastic deformation event was bracketed in time by two dated generations of pegmatite, as the oldest generation is constrained to the amphibolite boudin, while the youngest generation of pegmatite cuts through the gneiss and boudins borders.

Zircon data from the gneiss indicate protolith ages between 1.7 and 1.6 Ga, and discordant data for zircon in a migmatitic amphibolite suggest coeval formation. Monazite gives a metamorphic age 1554 ± 11 Ma. The area was strongly overprinted by Sveconorwegian deformation and metamorphism. This is well documented by zircon, titanite and rutile data from the garnet amphibolite rocks, indicating ages between 1040 and 1030 Ma for this event. The two latest pegmatite generations yield discrete ages of 1040.7 ± 4.2 and 1033.2 ± 1.2 Ma based on zircon and monazite, and thus constrain the time of formation of the main foliation in the gneiss. Titanite crystallization in the garnet amphibolite as well as one of the sampled pegmatites gives a crystallization age around 920 Ma, which corresponds to the time of intrusion of the Iddefjord granite, a part of the Bohus batholith. This late and low-U titanite likely formed by fluid induced mineral reactions that liberated Ti and Ca.

Brittle faults represent the youngest part of the deformation history. The faults vary in orientation and age, with cohesive and unchohesive fault rocks. Thin-sections of cataclasite show several stages of activation, and the youngest faults, containing a fault gouge, mark the end of a history of formation and deformation that spanned nearly 1700 million years.

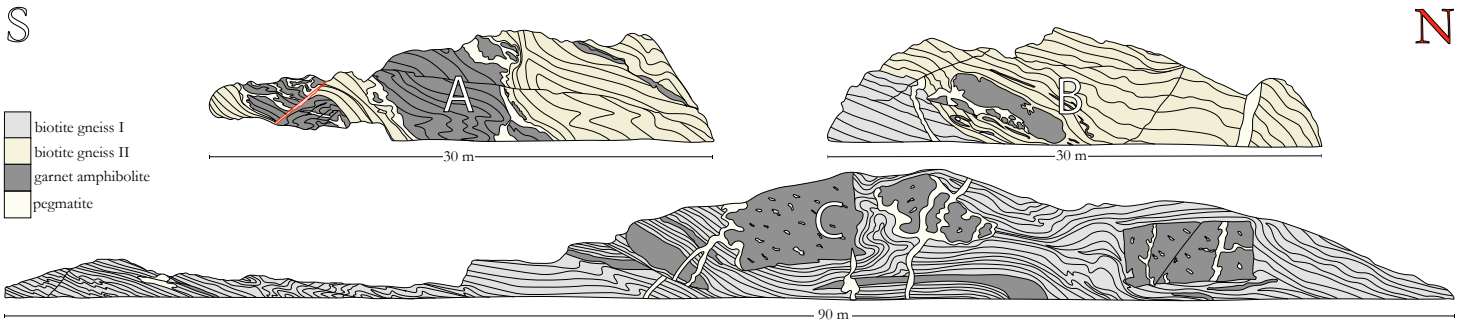

Acknowledgments

I would like to express my gratitude to my two main supervisors, Professor Fernando Corfu and Professor Roy Helge Gabrielsen, for useful comments, remarks and engagement through the learning process of this master thesis. The knowledge you possess is truly inspiring, and I'm grateful that you shared some of it with me.

Furthermore I would like to thank the people I have worked with at the TIMS-laboratory at the Department of Geosciences at the University of Oslo (UiO) for having warmly greeted me. I would also like to thank principal engineer Gunborg Bye Fjeld for the introduction to initial sample preparations.

To my fellow students, colleagues and friends at the University of Oslo, I would like to thank you for making the last five years a fantastic time.

At last, a special thanks goes to my family and loved ones who have supported me throughout the whole process.

Bjørn Magnus Mowinckel Nilsen Narum
December, 2016

Contents

Chapter 1: Introduction

1.1 Background

The study was initiated by Roy Helge Gabrielsen (UiO) that, after suggestions from Michael Heim (NMBU), initially visited the 150 meters of saw-cut outcrops located at Remmen, Halden (Østfold) **(map, appendix D)**. These pristine outcrops display a pervasively deformed amphibolite-gneiss sequence intruded by several pegmatite veins of presumably different generations **(fig 1.1)**, within the Gothian Stora Le-Marstrand formation. The formation lies within the Iddefjord Terrane, which is characterized by strong Sveconorwegian deformation.

The bedrock in Østfold is largely hidden by Quaternary deposits and only very seldom are there continuous exposures **(Graversen, 1973)**. Therefore, these outcrops represent a fantastic opportunity to study a small piece of a large puzzle, in great detail.

Figure 1.1: The outcrops (A, B & C) investigated in this study, located at Remmen, Halden (Østfold).

1.2 Aim of the study

The study is based on traditional structural field analysis and utilizes Pb-U dating of zircon, monazite, titanite and rutile by ID-TIMS, with the main goal to reveal the thermo-tectonic evolution of the outcrops.

The subordinate aims to achieve this are three-folded:

1. To capture the prominent time relations between the lithologies, the metamorphic events that deformed or formed them and if possible determine their genesis.

2. To prove that the pegmatite intrusions belongs to more than one generation, and with that, pinpoint the event of main deformation.

3. To correlate the ages derived in the study with established events in the region, and provide new data contributing to the tectonic evolution of the Østfold Gneiss-Complex.

Chapter 2: Regional geology

2.1 Introduction

In the following, the regional geology will be presented. First by the geological framework of the Fennoscandian Shield, followed by the presentation of the terranes of the Southern Scandinavian Domain. After this the evolution of the Sveconorwegian orogeny is presented, followed by a detailed description of the Stora Le-Marstrand formation situated in the Iddefjord terrane.

2.2 Geological framework

The Southwest Scandinavian Domain (SSD[1]) is situated south-west on the Fennoscandian Shield **(fig 2.1)(Gorbatschev and Bogdanova 1993)**. The Fennoscandian Shield (FS) constitutes the northwestern part of the East European Craton and consists of several domains with a regular temporal zonation, younging from the northeast to the southeast: the Archaean Domain in the northeast, the Svecofennian Domain in the central part, the Transscandinavian Igneous belt (TIB) and the Southwest Scandinavian Domain (SSD) in the southwest **(Gaál and Gorbatschev 1987)**.

The Archaean domain generally refers to the mosaic of Mesoarchaean to Neoarchaean cratonic fragments (>2.0 Ga) found in the northeast of the FS **(Lahtinen 2012)**. The Svecofennian Domain includes elements from the Paleoproterozoic orogenic evolution in Fennoscandia 2.0 - 1.8 Ga, which was a period of continental growth and accretion **(Lahtinen 2012, Roberts and Slagstad 2015)**. The TIB is a 1400km long array of batholiths extending from the southwestern Swedish coastline to the northwestern Norwegian coastline, comprises 1.85 to 1.65 Ga coarse monzodiorites and granites with an alkali-calcic chemistry, and transitions to alkaline rocks **(Högdahl, Andersson et al. 2004)**. The SSD is the westernmost crust accreted on the FS during the middle Proterozoic, mostly built up by rocks of Gothian age (1.75 - 1.50 Ga)**(Andersen 2005)**, reworked during several metamorphic events: Hallandian orogeny (1.5-1.4 Ga), Sveconorwegian orogeny (1.15-0.9 Ga), and Caledonian orogeny (0.6-0.4 Ga) **(Gaál and Gorbatschev 1987)**. The present-day metamorphic mineralogy in the SSD is largely controlled by Sveconorwegian deformation processes **(Andersen 2005)**. The SSD is separated from the Svecofennian Domain by the TIB in the east, as well as two Sveconorwegian shear zones: the Protogine Zone (PZ) and the Sveconorwegian Frontal Deformation Zone (SFDZ) **(Andersen 2005)**. The PZ is a belt of shearing and faulting, between the strongly foliated rocks of the SSD to the west and the better preserved Svecofennian terrains and the TIB to the east **(Gaál and Gorbatschev 1987)**. The SFDZ marks the easternmost limit of the Sveconorwegian deformation **(Wahlgren, Cruden et al. 1994)**.

The Sveconorwegian Belt (or Sveconorwegian Orogenic Belt) refers to the same domain as the SSD described above. This 500 km wide orogenic belt resulted from extensive magmatism and a collision between Fennoscandia and another major plate (possibly Amazonia), in late Mesoproterozoicum, and is subdivided into five units separated by crustal shear zones **(fig 2.2)**. These five units, from east to west, are: The Eastern segment, Iddefjord-, Kongsberg-, Bamble- and Telemarkian-Terrane. **(Bingen et al. 2008a, Bingen et al. 2008b)**.

[1]The SSD term is not frequently used in modern literature, although **Andersen (2005)** uses the term in his paper addressing regional nomenclature in the Fennoscandian Shield.

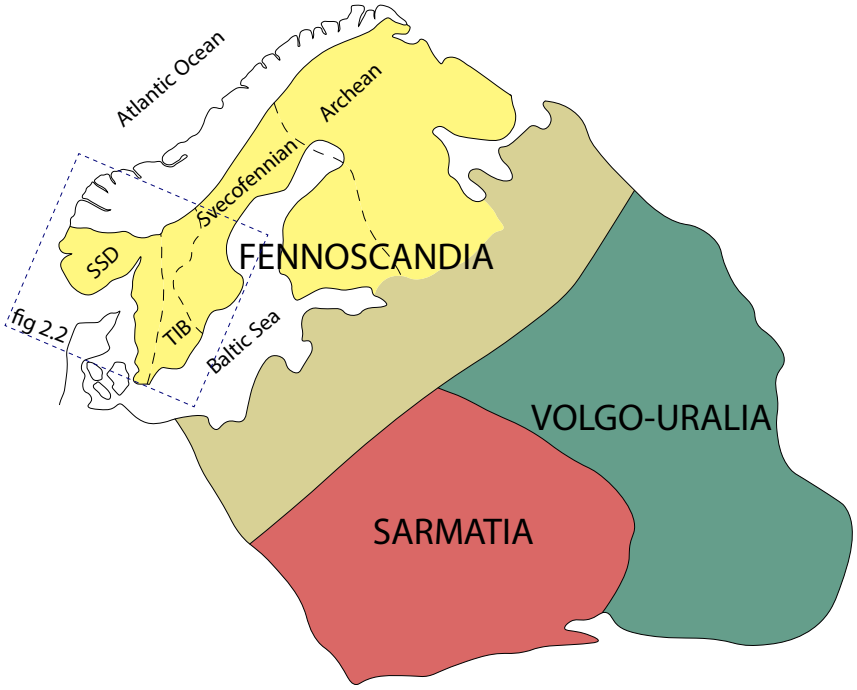

Figure 2.1: Simplified geologic map of emplacement of Fennoscandia within the East European Craton. Modified from **(Gorbatschev and Bogdovan 1993, Lahtinen 2012)**

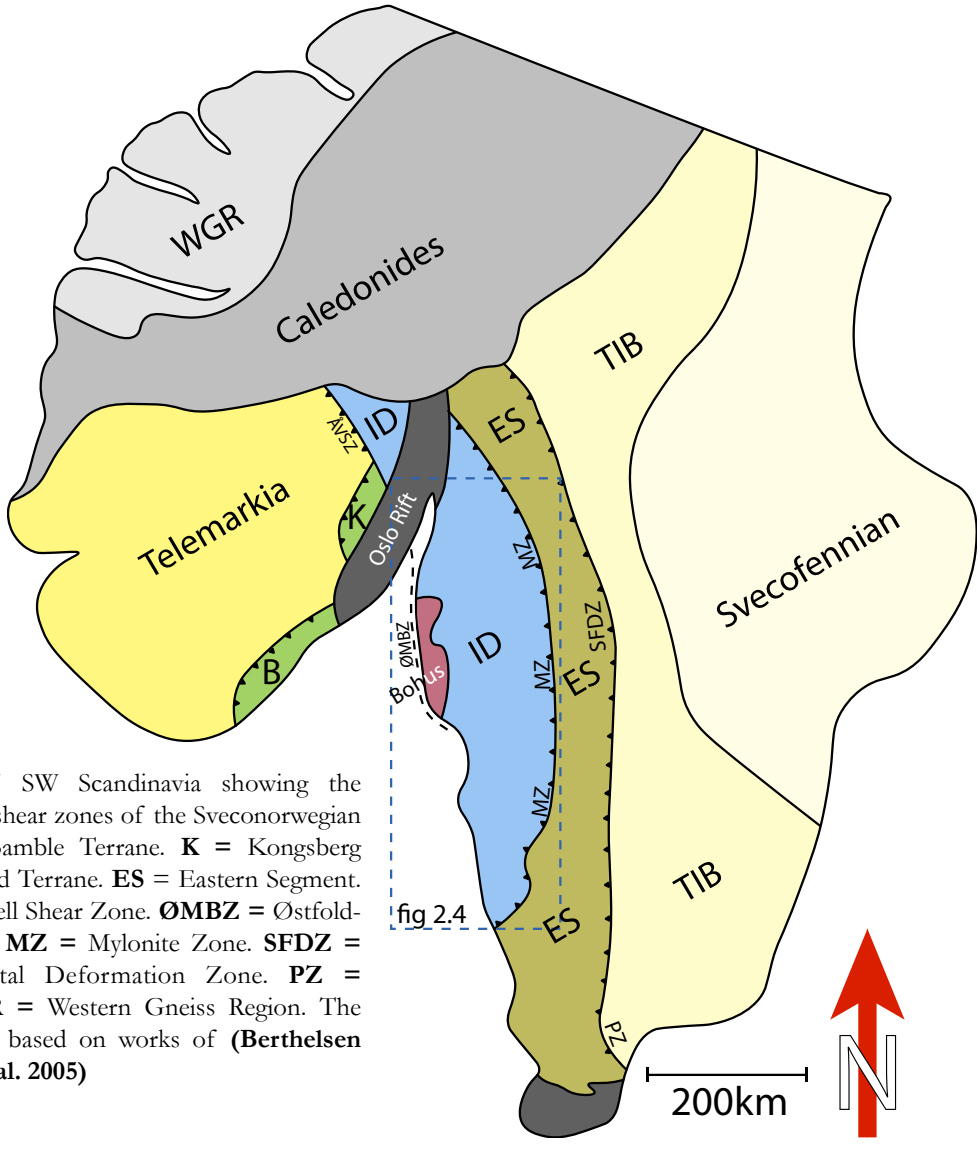

Figure 2.2: Map of SW Scandinavia showing the lithotectonic units and shear zones of the Sveconorwegian orogenic belt. **B** = Bamble Terrane. **K** = Kongsberg Terrane. **ID** = Iddefjord Terrane. **ES** = Eastern Segment. **ÅVSZ** = Åmot-Vardefjell Shear Zone. **ØMBZ** = Østfold-Marstrand Shear zone. **MZ** = Mylonite Zone. **SFDZ** = Sveconorwegian Frontal Deformation Zone. **PZ** = Protogine Zone. **WGR** = Western Gneiss Region. The figure is modified and based on works of **(Berthelsen 1980, Bingen, Skar et al. 2005)**

The nomenclature may vary, as some authors may prefer a non-genetic nomenclature as «blocks» instead of «terrane». This discussion is addressed by **Andersen (2005).** The general configuration of the terranes in the SSD and their genetical relation to each other is not consistent in the literature. Nonetheless, there is a consensus which will be the base for this presentation.

The Eastern Segment consists of gneissic granitoids rocks (1.80-1.64 Ga), compositionally similar, and related, to the rocks of the TIB **(Bingen et al. 2008b).** It is considered as a reworked Fennoscandian parautochthonous segment, and is bounded to the east by the SFDZ. A late Sveconorwegian high-pressure metamorphic overprint dated 0.97 Ga is characteristic, with locally eclogite-facies metamorphism. There are also evidence of pre-Sveconorwegian deformation connected to the Hallandian Orogeny in the segment **(Bingen et al. 2005)**.

The Iddefjord Terrane is situated to the west of the Eastern Segment, and extends from south of Gothenburg, to the Caledonian nappe front in the north, across the Late Palaeozoic Oslo rift. The terrane is truncated by the Mylonite Zone (MZ) to the east, and the Østfold-Marstrand and Åmot-Vardefjell Shear Zones to the west **(fig 2.1)(Bingen et al. 2005)**. The terrane comprises 1.66 - 1.52 Ga greenschist- to amphibolite-facies tholeiitic to calc-alkaline plutonic and volcanic rocks, associated with greywacke bearing metasedimentary sequences **(Bingen et al. 2005, Viola et al. 2011)**. A detailed map of the Iddefjord Terrane can be seen in **figure 2.4**, modified from **(Åhäll and Connelly 2008)**.

Two small terranes, the Bamble and Kongsberg terranes, are situated between the Telemarkian and Iddefjord terranes **(fig 2.1)**. They are made up of 1.57 - 1.46 Ga plutonic suites associated with metasedimentary complexes. The Kongsberg Terrane hosts 1.2 Ga mafic intrusions, and Bamble host mafic intrusion complexes in four periodes between 1.2 - 0.9 Ga **(Bingen et al. 2008b)**. Based on geophysical data both terranes are considered as two tectonic wedges formed during a collision between the Telemarkian and Iddefjord Terrane, overlying the Telemarkian Terrane **(Andersson et al. 1996)**.

To the west, the Telemarkia Terrane is situated. The Terrane is truncated by the Åmot-Vardefjell and Saggrenda-Sokna shear zones to the east, the Kristiansand-Porsgrunn shear zone to the south-east and the Caledonian nappe front in the north **(fig 2.1)(Bingen et al. 2005)**. The Telemarkia Terrane is characterized by 1.52 - 1.48 Ga volcanic and plutonic suites associated with quartzite-bearing metasedimentary sequences. It also contain several pre-Sveconorwegian deformed magmatic suites, and Sveconorwegian pre-,syn-, and post-collisional plutonic suites **(Bingen et al. 2008c)**.

2.3 The evolution of the Sveconorwegian Orogeny

Despite the well documented petrologic, geochemical, geochronological and (to an extent) structural data in the Sveconorwegian orogen, the evolution of the orogen is not fully understood. Hence, different models for the orogenic evolution are centers for discussions. In this chapter the four-phase model by **Bingen et al. (2008b)** will be presented, promoting the conventional continent-continent collisional tectonics. The non-collisional accretionary model for the Sveconorwegian orogen by **Slagstad et al. (2013),** will also be discussed briefly.

2.3.1 The four-phase model

Arendal phase (1140-1080 Ma)

The earliest metamorphic event connected the Sveconorwegian Orogeny, is referred to as the Arendal phase (1140-1080 Ma), interpreted as a collisional event between Telemarkia and Iddefjorden Terranes, that produced an orogenic wedge consisting of the Bamble and Kongsberg Terranes. The phase is characterized by the early formation of granulites in the Bamble terrain near Arendal (1140-1125 Ma), and the later propagation of high-grade metamorphism (1110-1080 Ma) detected in Kongsberg and Iddefjorden Terranes. The last major event connected to this earliest Sveconorwegian event, was the thrusting of the Bamble Terrane onto the Telemarkia ramp **(Bingen et al. 2008b)**.

Agder phase (1050-980 Ma)

«The main Sveconorwegian event» took place between 1050 and 980 Ma, and is known as the Agder phase. The Agder phase is thought to represent a continent-continent collision between Fennoscandia and possibly Amazonia (or another continent), resulting in crustal thickening and imbrication in the central part of the orogen, including deformation, metamorphism and magmatism in the Iddefjorden and Telemarkia Terranes. High-pressure amphibolite- to granulite-facies metamorphism is recorded in the Iddefjord Terrane between 1050 and 1030 Ma, at the same time as granodiorite plutons intrude in the

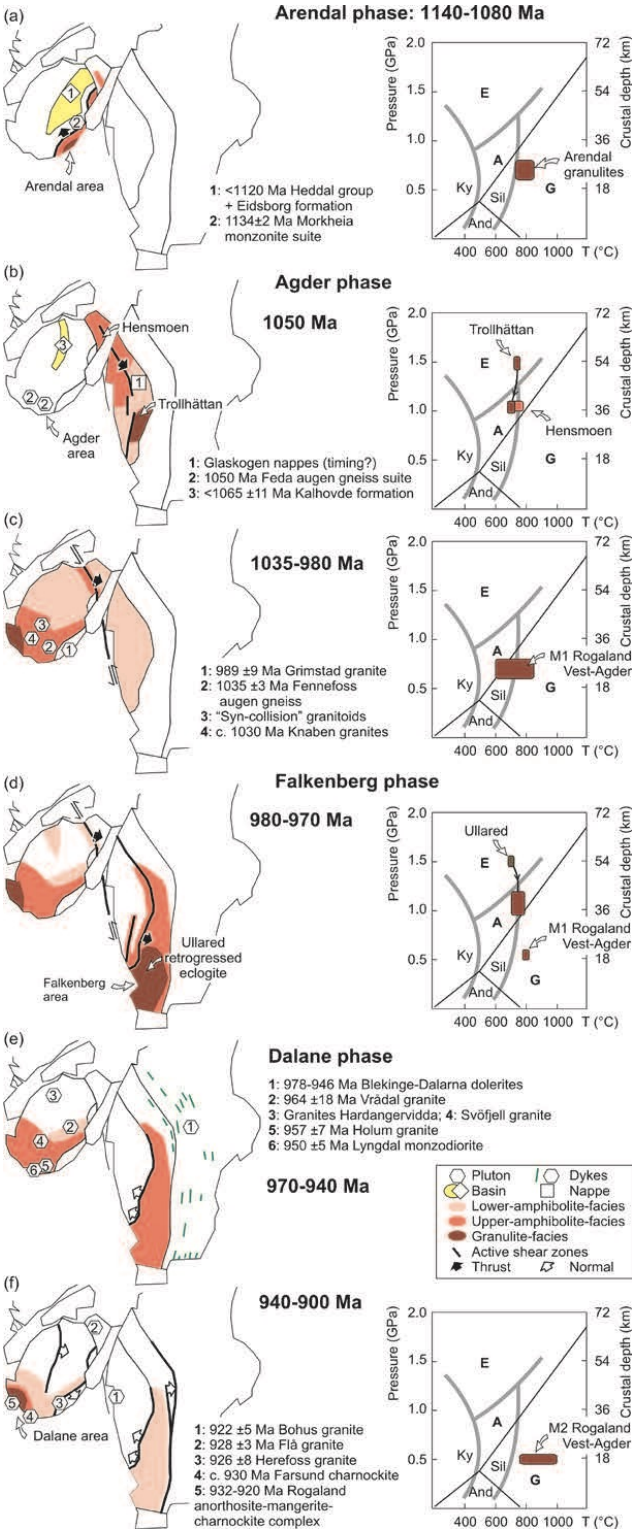

Figure 2.3 → : Sketchmaps showing the distribution of metamorphism, magmatic rocks and sedimentary basins during the Sveconorwegian orogeny. For each time slice, metamorphism is illustrated in the pressure-temperature space. **(a)** Arendal phase: 1140-1080Ma **(b, c)** Agder phase: 1050-980 Ma. **(d)** Falkenberg phase: 980-970Ma. **(e, f)** Dalane phase: 970 - 900 Ma. Illustration from **(Bingen et al. 2008b).**

Telemarkian Terrane. Telemarkia experienced crustal thickning after this, at the same time as unroofing in Iddefjorden. In general significant pressure contrasts are seen between the two terranes, as Iddefjord terrane has a higher metamorphic signature **(Bingen et al. 2008b)**.

Falkenberg phase (980-970 Ma)

As the orogeny propagated eastwards it eventually reached the Fennoscandian parautochthonous Eastern Segment between 980 and 970 Ma. This metamorphic «step» into the foreland defines a third phase, known as the Falkenberg phase. The crustal thickening propagated eastwards, with a burial depth of the Fennoscandian crust of at least 50 km, producing Eclogite in the Eastern Segment. The event represents the last evidence of convergence in the Sveconorwegian belt **(Bingen et al.2008b)**.

Dalane phase (970-900 Ma)

A period of relaxation, gravitational collapse and extension between 970 and 900 Ma, is known as the Dalane phase, and marks the end of the Sveconorwegian orogeny. The phase is characterized by the large volumes of post collisional magmatism that peaked between 930 and 920 Ma, with intrusion of the Rogaland AMC complex in western Telemarkia terrane, and the Bohus and Flå plutons in the Iddefjord terrane. The source of magmatism is suggested to be related to upwelling of hot lithospheric mantle to the base of the crust at the end of the orogenic cycle **(Bingen et al. 2008b)**.

2.3.2 The non-collisional model

Slagstad et al. (2013) challenge the conventional view that the Sveconorwegian orogeny resulted from continent-continent collision. They argue that recently interpreted long lived magmatic intrusions in western parts of the Telemarkia Terrane, such as the Sirdal Magmatic Belt (SMB), are incompatible with the established continent-continent model. Instead, a long lived accretionary model of Andean-type is suggested, dividing the orogeny into three periods; 1) 1.05 - 1.02 Ga, 2) 1.02 - 0.99 Ga and 3) 0.99 - 0.92 Ga. The first period was characterized by continuous magmatism due to mantle upwelling forming a mafic underplate. The second period was characterized by a pause in magmatism, caused by flattening of the subducting slab. The third period was again characterized by magmatism and the formation of igneous suites, caused by delamination and partial melting of the lower crust **(Slagstad et al. 2013)**.

Möller et al. (2013) consider the proposed model by **Slagstad et al. (2013)** problematic, and argues that the model ignores several key observations, as the formation of eclogites in the Eastern Segment, promoting a continent-continent collision.

2.4 Stora Le-Marstrand Formation

The Iddefjord terrane comprises six major crustal units; **1)** Supractrustal rocks of Horred fomation (ca 1.66 Ga), **2)** Volcanic, volcano-clastic and sedimentary rocks of the Gothenburg suite and Åmål belt (1634-1594 Ma), **3)** Granitoid intrusions of the Hisingen Suite (1588-1522 Ma), **4)** Stora Le-Marstrand formation (SLM, 1.59-1.55 Ga) **5)** Volcanic and sedimentary rocks of the Dal formation (Ca 1.1 Ga) and **6)** The granitic rocks of the Bohus pluton (ca. 920 Ma) **(Åhäll et al. 1995, Åhäll and Connelly 2008)**.

The SLM formation forms a 20-50km wide belt (N-S) between Gothenburg in SW Sweden to the Caledonian nappe front in SE Norway, within the Iddefjord Terrane **(fig 2.4)**. It is comprised of metamorphosed greywacke-type sediments with widespread metabasalt. Migmatization is related to Gothian deformation, and Sveconorwegian reworking is mostly confined to areas of folding and shear zones **(Åhäll et al. 1998, Åhäll and Connelly 2008)**. Traditionally the supracrustal rocks of the SLM have been considered belonging to a single unit, however recent data from **Åhäll and Connelly (2008)** require at least two distinct packages, which they refer to as SLM-1 and SLM-2.

The SLM-1 rocks include metabasalts and volcaniclastic rocks: banded amphibolites, pillow basalts, mafic to intermediate dykes and felsic layers interpreted as volcaniclastic **(Åhäll and Connelly 2008)**. The best preserved SLM-1 rocks are found north of Gothenburg. Nd isotopic data from metasediments investigated by **Åhäll and Daly (1989)** show both a juvenile signature and a continental affinity. Basalts investigated by **Brewer (1998)** show trace element signatures of an oceanic arc-setting. This indicates two different sources, and a proximity to the Fennoscadian margin. **Åhäll and Connelly (2008)** concludes with deposition and deformation of the SLM-1 rocks in a mature back-arc setting or connected to the formation of an island arc proximal to western Fennoscandia ~ 1.59 Ga.

The SLM-2 rocks are supracrustal rocks deposited after 1.56 Ga, >25 m.y. after the formation of SLM-1. They are found in western parts of the belt. Similar to SLM-1, the SLM-2 rocks were deposited in a mature back-arc setting or during the fomation of an island arc in proximity of western Fennoscandia **(Åhäll and**

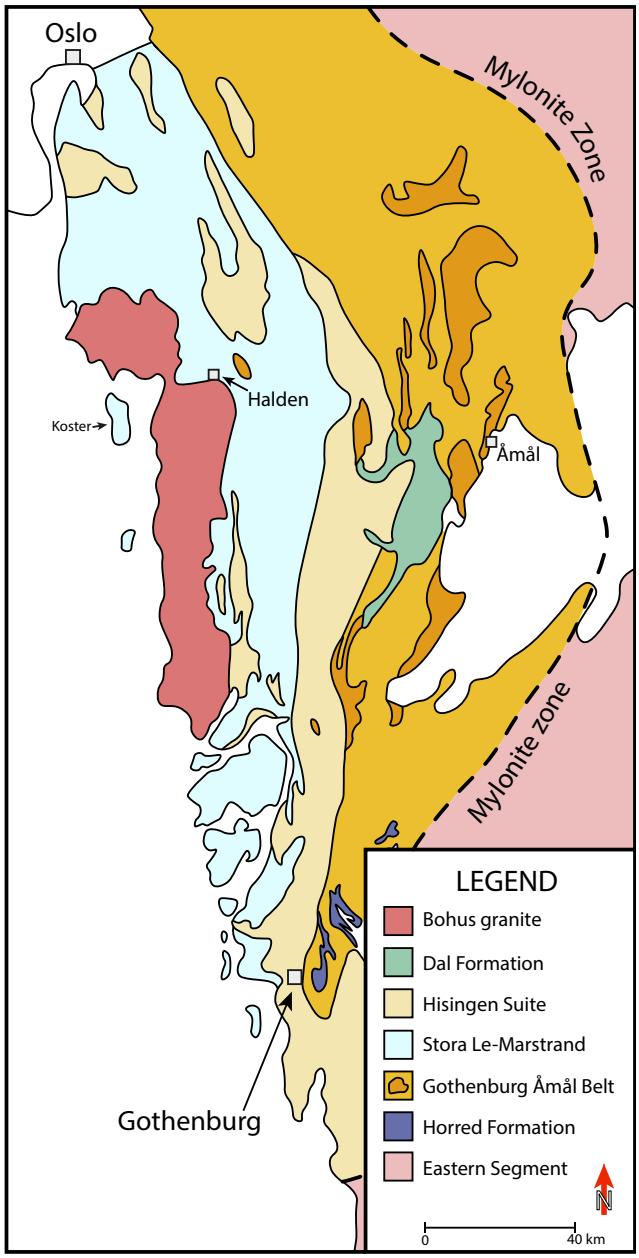

Figure 2.4: Geological map of the Iddefjord terrane showing major crustal units. Simplified and modified from **(Åhäll and Connelly 2008).** Halden is marked at the boarder between the Bohus granite and the SLM unit. Island of Koster is straight west.

Connelly 2008). Granodiorite dikes at Koster Island intruding 1545 ± 5 Ma, cross-cutts SLM-2 rocks, bracketing the accretion of SLM-2 rock to Fennoscandia between 1.56 Ga and 1545 ± 5 Ma **(Åhäll and Connelly 2008).**

Chapter 3: Geochronology - Theoretical foundation

3.1 U-Pb dating

The radioactive decay series from uranium (*U)* and thorium (*Th*) to lead (*Pb*) plays the main role in quantifying geologic time, and forms the foundation of several geochronological isotopic dating methods. *U* occurs in nature as ^{238}U, ^{235}U and ^{234}U, and *Th* occurs as ^{232}Th. These principal isotopes of *U* and *Th* are each parent of a chain of radioactive daughter isotopes, ending with a stable *Pb* isotope. The decay series from ^{238}U (uranium series) include ^{234}U as an intermediate daughter and ends in stable ^{206}Pb. The decay of ^{235}U (actinium series) ends up in stable ^{207}Pb, and the decay series from ^{232}Th ends up in stable ^{208}Pb **(Faure and Mensing 2005)**. These radioactive decay series can be expressed by the following equations respectively, with associated half-life constants from **(Steiger and Jäger 1977)**:

$$^{238}U \rightarrow {}^{206}Pb + 8\alpha + 6\beta- \ (T_{1/2} = 4468\ Myr) \quad (1)$$

$$^{235}U \rightarrow {}^{207}Pb + 7\alpha + 4\beta- \ (T_{1/2} = 703\ Myr) \quad (2)$$

$$^{232}\mathrm{Th} \rightarrow {}^{208}Pb + 6\alpha + 4\beta- \ (T_{1/2} = 14010\ Myr) \quad (3)$$

The parent isotopes do not decay directly to *Pb,* but follow a sequence of intermediate daughter isotopes. These chains of daughter isotopes, known as decay chains, can be seen in **figure 3.1 (Schoene 2014)**. Despite the fact that 43 isotopes of 12 elements are formed intermediately, none of them is a member of more than one decay chain, hence each decay chain always leads to the formation of a specific stable *Pb* isotope **(Faure and Mensing 2005)**. The half lives of ^{238}U and ^{235}U are long enough to span across the history of our planet, and at the same time short enough that both parent and daughter isotopes can be measured in a sample relatively easily. The knowledge of the paired nature of the decay systems of *U* (equation 1 & 2) provides an internal test of accuracy. The two possible ages ($^{238}/_{206}$ & $^{235}/_{207}$) provided in the a given sample, should agree if the system has been closed to mobility of parent or daughter **(Davis et al. 2003)**.

For a mineral to give a meaningful *U-Pb* age (concordant age) these three conditions must be satisfied: 1) *U* was incorporated in the mineral structure during crystallization. 2) Correct values for unradiogenic *Pb* is used for the initial mineral composition. 3) The mineral is able to retain *U, Pb* and intermediate daughters. Furthermore it is a advantage if the mineral has a structure that is not compatible with incorporation of *Pb* during crystallization. This produces a high *U*/*Pb*-ratio which is more robust against initial *Pb* composition, which cannot be differentiated from radiogenic *Pb* in a sample **(Augland 2012)**

Several minerals incorporate enough *U* in their structure to be datable, but do not always fulfill the condition of retentiveness with respect to *U, Pb* and intermediate daughters **(Faure and Mensing 2005)**. In this thesis *U-Pb* ages has been collected from four minerals: Zircon, Monazite, Titanite and Rutile. These will therefore be described in detail in this chapter.

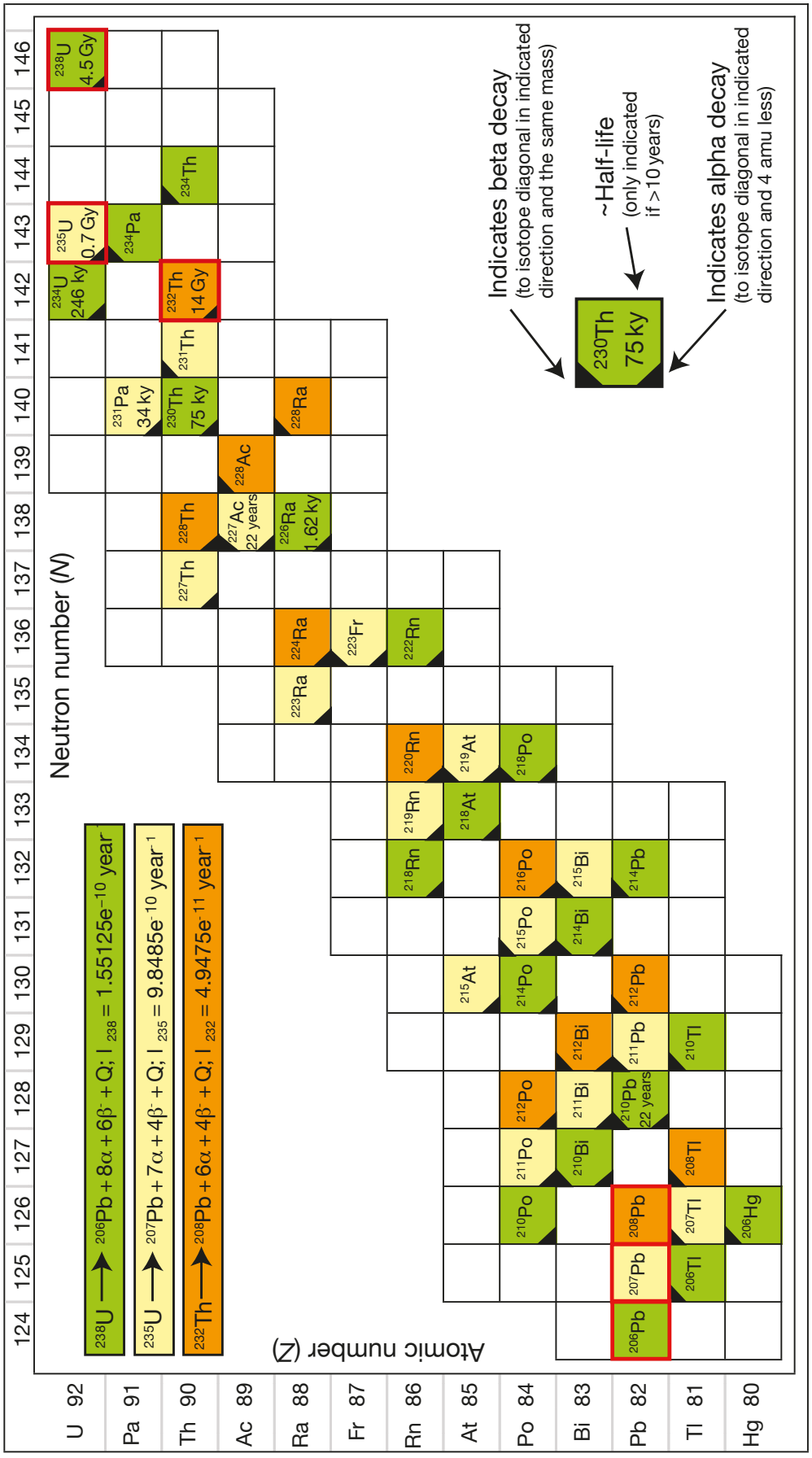

Figure 3.1: Illustration of the *U-Th-Pb* decay chains. Each isotope is color-coded to its parent isotope. Parent and stable daughter isotope are outlined in red. Equations for each decay chain with associated decay constants can be seen in the top left corner. α is an alpha particle, β is a beta particle, and Q is energy released during the decay. Figure from **(Schoene 2014)**.

3.2 Zircon

«The wide utilization of the U-Pb geochronometer would not have been possible without the mineral zircon»

- Davis 2003

Zircon ($ZrSiO_4$) is the most widely used geochronometer, and is a common accessory mineral in felsic magmatic rocks and also locally found in mafic intrusives **(Augland 2012)**. Zircon contains much more *U* than its host rocks, due to the isomorphous replacement of Zr^{4+} with U^{4+}, at the same time strongly discriminating against *Pb* during crystallization, due to similarities and differences in ionic radius respectively **(Parrish and Noble 2003)**. Zircon also has a very high retention temperature for *Pb* (usually >900˚C), and is a though mineral capable of surviving a high-grade metamorphic event and a possible remelting **(Cherniak and Watson 2003, Augland 2012)**. However, zircon can also grow during metamorphic events. In metamorphic rocks, zircon commonly contain a old core with record of the protolith, and zonation(s) of metamorphic overgrowth(s) dating metamorphic event(s). It also has a chemical stability at surface conditions and a hardness >7.5 that allows it to survive sedimentary cycles. Detrital zircons can be used to infer about the sediment source(s) **(Augland 2012)**. All these capabilities makes zircon an ideal mineral for *U-Pb* dating, of both protolithic and metamorphic age.

Zircons are extremely variable in terms of both internal and external features. These features reflect the geologic history of the mineral, and especially the relevant episodes of magmatic and metamorphic crystallization **(Corfu et al. 2003)**. In this study zircon has been retrieved from all of the lithological units, with variable morphology and texture, from low quality metamict grains to prismatic high quality grains **(see fig 3.2)**.

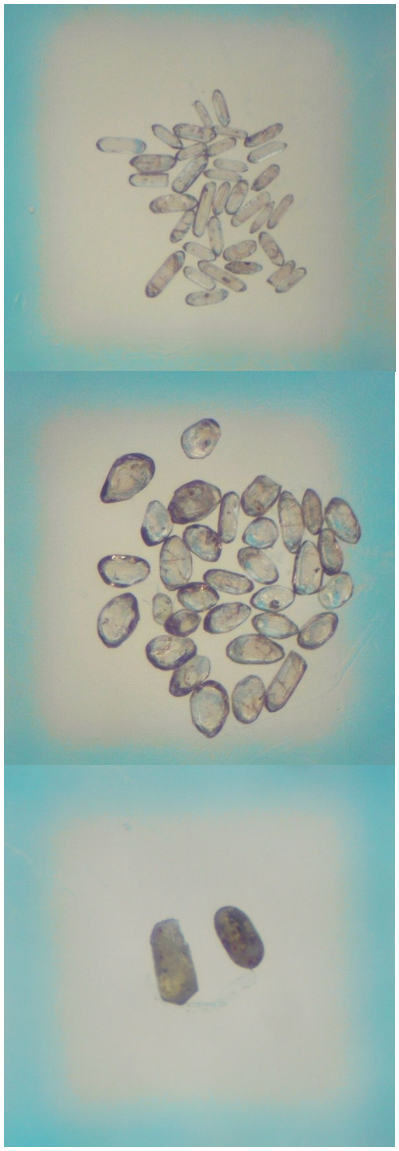

Figure 3.2: Composite image of three set of zircon populations from the study. The pictures are the same scale, and each frame represents $1mm^2$. **Top**: euhedral zircon crystals from sample BN15-02 (gneiss). **Middle:** Rounded zircon crystals, also from BN15-02 (gneiss). **Bottom**: Two metamict zircon grains from sample BN15-07 (Pegmatite).

3.3 Monazite

Monazite (LREE(PO_4); LREE = light rare-earth ions like La, Ce, Nd etc.) is a useful geochronometer, where U^{4+} and Th^{4+} can substitute the REE-site via coupled substitution. Monazite typically contains high amounts of Th^{4+} (up to 20wt% ThO_2) and comparably lower contents of *U* (up to 2 wt% UO_2), and tend not to incorporate Pb^{2+} during crystallization, but can accept *Pb* in same position as *U* and *Th,* leading to good retention of *Pb* and closure temperature ≈ 900˚C **(Harrison et al. 2002, Augland 2012)**. Monazite occurs as an accessory mineral in magmatic rocks and because of a wide stability field it grows during metamorphism, prominent above grennschist grade. The common appearance in metapelitic rocks makes monazite ideal for dating metamorphic events **(Spear and Pyle 2002, Augland 2012)**. In this study monazite has been used to date gneiss and pegmatite. An example can be seen in **figure 3.3.**

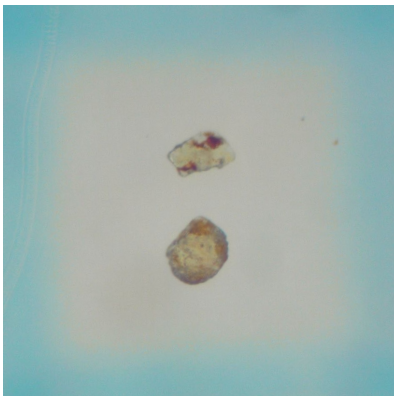

Figure 3.3: Example of how monazite can look like in an sample. These two grains are picked in sample BN15-07 (pegmatite) in the study. The frame represents 1mm².

3.4 Rutile

Rutile (TiO_2) commonly occurs as an accesory mineral in both metamorphic and igneous rocks that may incorporate U4+ in its structure **(Augland 2012, Kooijman et al. 2010)**. The closure temperature of rutile is distinctly lower than the closure temperature of zircon and monazite (400-600˚C), hence carefull interpretation of the data is required. The low closure temperature means that rutile often date cooling of a rock and not crystallization of a magma or peak metamorphism. Rutile may also incorporate Pb2+ during crystallization, necessitating accurate measurement of an unradiogenic Pb isotope (normally 204Pb) for what is known as "common lead correction" **(Augland 2012)**. The measured 204Pb makes it possible to exclude common lead affected data from further calculations. In this study rutile has been used to date an amphibolite. An example can seen in **figure 3.4.**

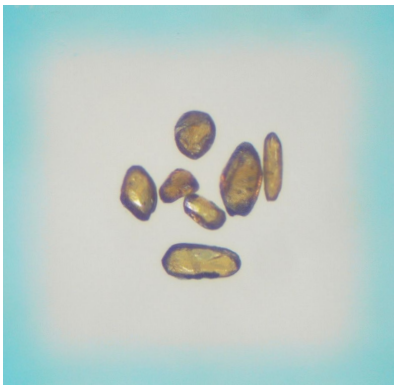

Figure 3.4: Example of how rutile grains can look like in an sample. The grains shown are picked in sample BN15-06 (amphibolite) in the study. The frame represents 1mm².

3.5 Titanite

Titanite or Sphene ($CaTiSiO_5$) occurs as both an igneous and a metamorphic mineral, with similar properties as zircon an monazite. It incorporates U through substitutuion with Ti4+, but far less than than the other analyzed minerals, hence no single grain analysis were done with this mineral. Titanite also has a fairly low closure temperature (>625˚C; **Dickin 2003**) compared to monazite and zircon, yet high enough to also preserve evidence of multiple growth events **(Augland 2012)**. An important note is that titanite needs corrections for common Pb (like rutile), because of the incorporation of Pb2+ during crystallization. In this study Titanite has been used to date amphibolite and pegmatite. An example of can be seen in **figure 3.5.**

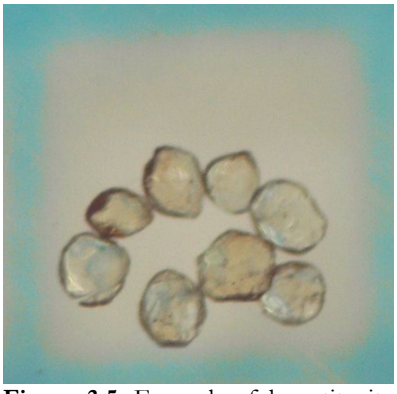

Figure 3.5: Example of how titanite grains can look like in an sample. The grains shown are picked in sample BN15-09 (amphibolite) in the study. The frame represents 1mm².

3.6 The Wetherill Concordia

«essential for every earth scientist with an interest in geologic time»
- Schoene 2014

Different graphical representation methods can be used to display the potential numerous variables in calculated *U-Pb* data from a sample. In this study the Wetherill concordia plot has been used, after **Wetherill (1956)**. The concordia diagram plots 206Pb/238U versus 207Pb/235U from the same analysis. The curve is non-linear due to the different half-lives of 238U and 235U, and represents a set of solutions of the equations:

$$^{206Pb}/_{238U} = (e^{\lambda 238 t} - 1) \qquad (4)$$

$$^{207Pb}/_{235U} = (e^{\lambda 235 t} - 1) \qquad (5)$$

Points on the concordia curve are calculated for the same values of t, hence the points refer to where 206Pb/238U and 207Pb/235U both correspond to the same date **(Schoene 2014)**. The calculated data from a sample will plot on the concordia curve if the sample remained in a closed system since the time of formation. Such an ideal sample is *concordent*. Samples that do not plot on the concordia curve are *discordant*, and have been affected by either external or internal factors leading to a loss in radiogenic *Pb*. The discordant samples will plot on a discordia line, that will intercept the concordia curve at two places; one yielding the age of the rock, and the other yielding the age of led loss **(Philpotts and Ague 2009, Schoene 2014)**. **Figure 3.6** shows an example of a Wetherill concordia with variable plots from a zircon sample, and what they could represent.

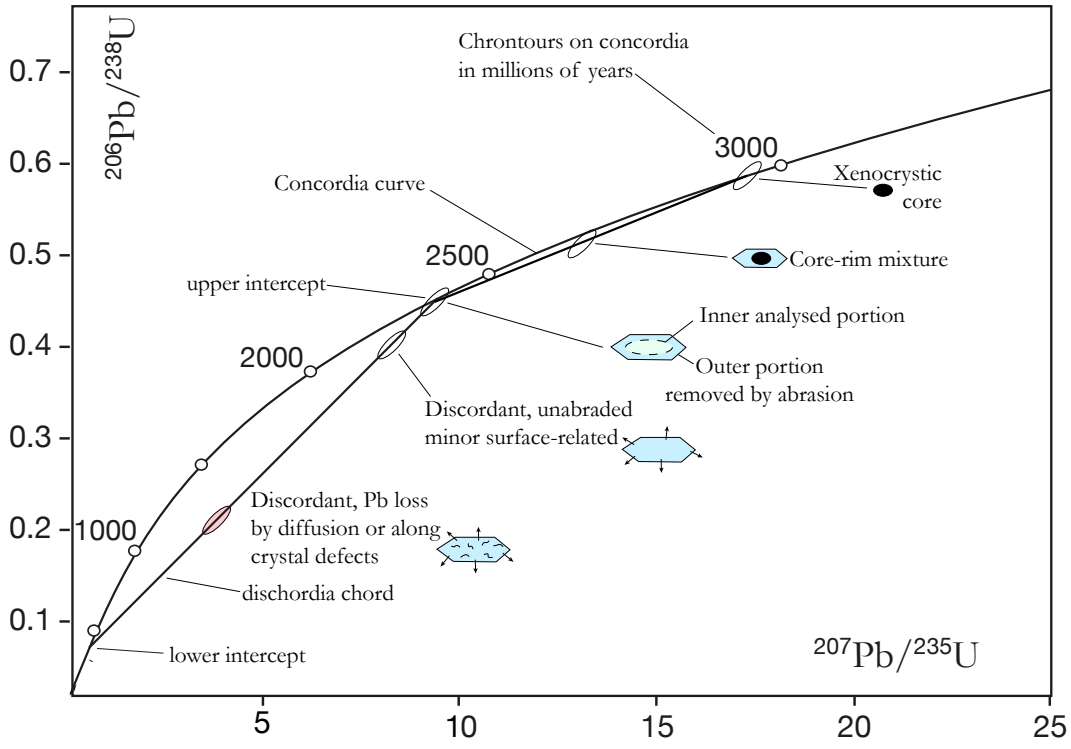

Figure 3.6: Illustrates common situations encountered during analysis of zircon, including inherited grains, mixed-age crystals that may define a chord, concordant data, and discordant analyses with Pb-loss. Modified from **Parrish and Noble (2003).**

3.7 The mass spectrometer (TIMS)

To use radiogenic isotopes as dating tools, they must be separated from non-radiogenic isotopes. This is done in a «mass spectrometer», of which several types exist (i.e ICP-MS, SIMS, TIMS etc). In this study a Thermal Ionization Mass Spectrometer (TIMS) has been used, and the very fundamentals about the machine will be explained in simplicity in this chapter. For sample preparation, and procedures leading up the the actual «loading» of the sample in the machine, please see **chapter 4: methods.**

The ID-TIMS consist of three essential parts: (1) a source of a monoenergetic beam of ions, (2) an electromagnet and (3) an ionic collector, **Figure 3.7.** The whole system operates in high vacuum. The source consists of a filament containing the sample, that starts to emit Pb^{+} and UO^{2+} ions as it gets heated to approximately 1300°C by an applied electric current. An high voltage module (anode) accelerates the ions in the direction of the electromagnet. As the ions pass the electromagnet, their trajectory is changed by a magnetic field proportional to their charge-to-mass ratio. Effectively this means that the trajectory of the lighter ions will be changed more than the trajectory of the heavier ions, permitting individual counting of the ions since they are separated according to mass. The counting is done either by a Faraday cup collector (if the intensity is big enough) or by an SEM collector (secondary electron multiplier).

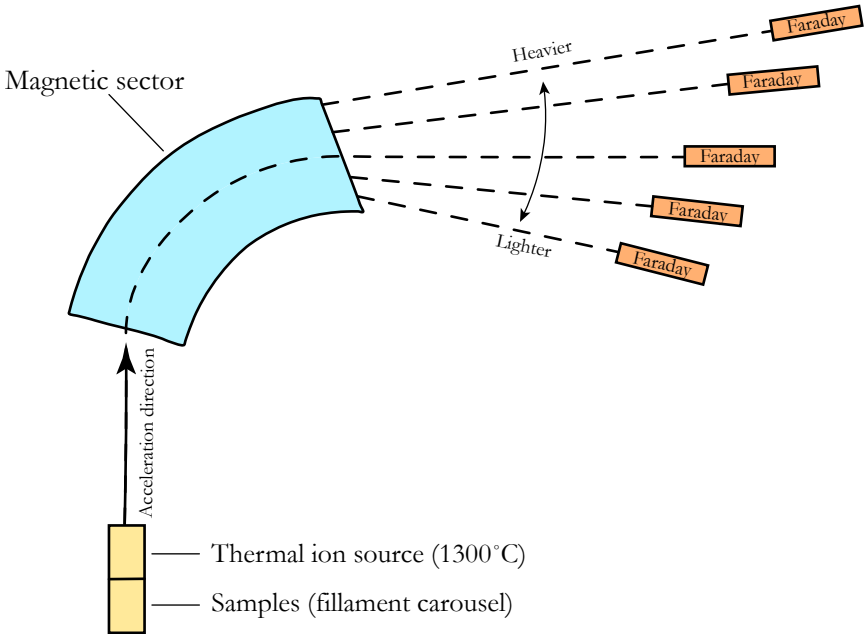

Figure 3.7: Simplified sketch of the «design» of mass spectrometer. First module is the sample chamber, next is the heat source followed by an arrow indicating the acceleration direction. Then the magnet module bends the trajectory of the the ions according to their charge-to-mass ratio, before they are collected by the faraday cups where each one represents a different ion.

Chapter 4: Methods

4.1 Introduction

The methods used in the study are presented in this chapter. Traditional fieldwork is a central element of the thesis, consisting of recording the field relations, sketching the outcrops and taking samples for analytical work. Thin-sections were produced for all samples, and for selected samples mineral separation was performed followed by U-Pb dating of zircons, titanites, monazites and rutiles using ID-TIMS (Isotope Dilution Thermal Ionization Mass Spectrometry). For an overview se **table 4.1.**

4.2 Field work

Geological fieldwork was conducted on 7 different occasions in the period between June 2015 and August 2016. The compact field area (described in detail in **chapter 5**) is easily accessible, and for that reason no longer field trips were considered necessary. Because of the lack of outcrops in the area around the studied roadcut it was not possible to map a large area around the outcrops with the tools available.

The first days of fieldwork were primarily used to get a good overview of the outcrops. This was achieved by sketching the outcrops in detail and by making a large photomosaic. The photomosaic made it possible to "re-visit" the outcrops when a physical visit was not possible. Both sketches and photos were later processed in professional imaging software provided by Adobe (Bridge, Photoshop and Illustrator), mainly with the intention of presenting graphics of as high quality as possible. By the help of a compass, a camera and a scale, structural data were also documented **(chapter 5.2 & 5.3)**. For the latter, the strike and dip direction method was applied, rather than using dip and dip-direction. In addition to this, a hand held lens and a geologic hammer were used to examine the rocks in detail. After an overview was achieved, samples were strategically collected.

4.3 Sampling

The field-area is presented in **chapter 5**, and an overview figure is found in appendix **D.** It is advised to take a look at both to get a better understanding for the following descriptions of exact sampling locations **(fig 4.1)**.

Samples from the outcrops have been collected with the purpose of doing mineralogical/petrological thin-sections descriptions, and for age determination, using ID-TIMS (geochronology). The sampled lithologies have been chosen, with the intention to investigate the thermo-tectonic history (metamorphic/structural) of the rocks. With that in mind, samples have been collected from outcrop A and outcrop C, using traditional field methods (hammer and chisel). In addition engine drilling with diamond core-bit was used for the pegmatite samples. The sampling sites were selected bearing in mind the results of preliminary lithological descriptions.

All sampled lithologies has been given the prefix BN15-, followed by an serial number. The samples are stored at the Department of Geosciences, University of Oslo (Sem Sælandsvei 1, Oslo), and are available for additional investigations.

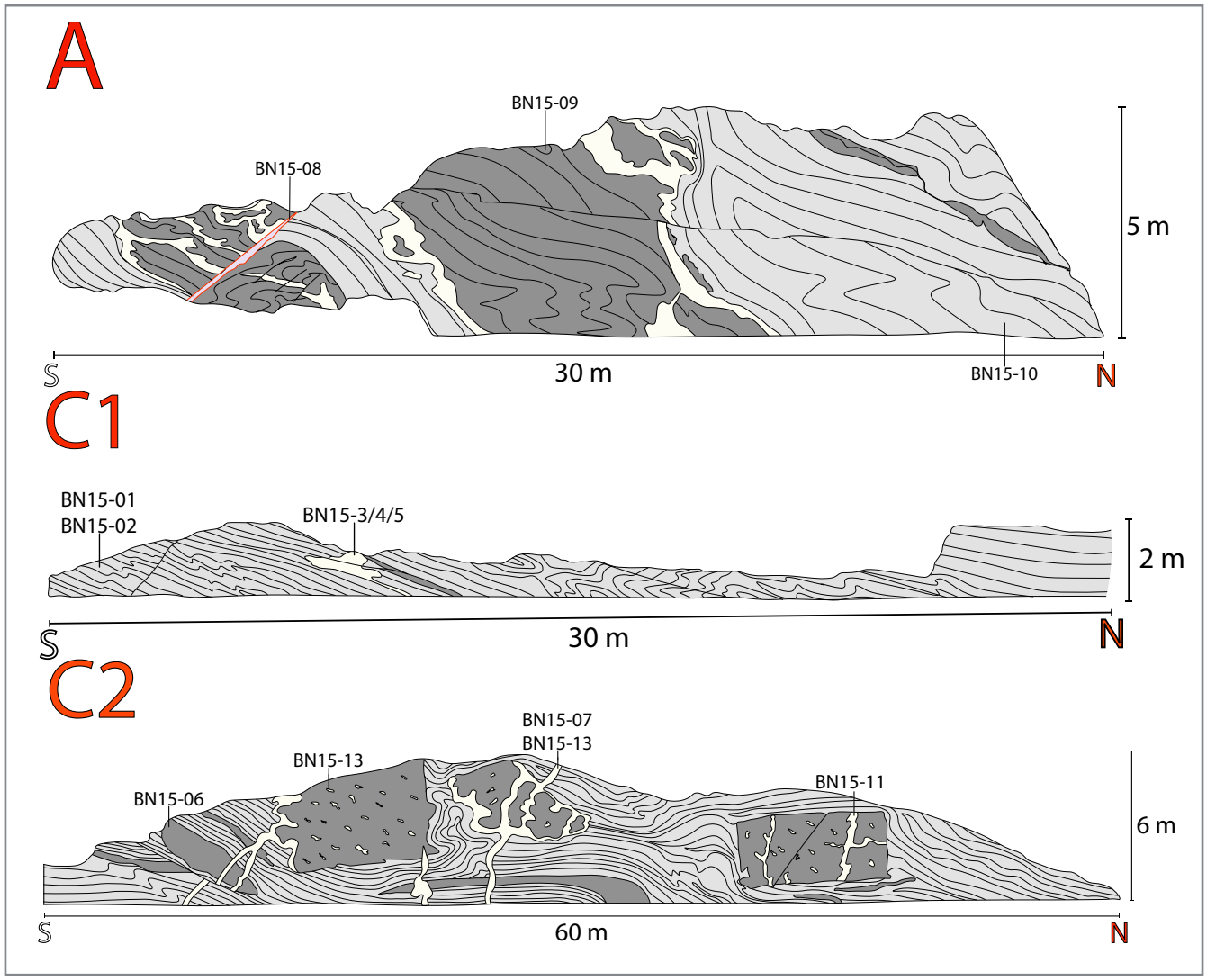

Fig 4.1: Positions of the samples collected in outcrop A and C (Outcrop C has been divided into C1 and C2 for illustrational purposes in this figure only). No samples have been collected from outcrop B, therefore it is not included in the figure. All samples have been collected using a hammer or engine-drill at the top of the outcrops, to preserve the surfaces as much as possible.

Sample	Lithology	Sector	Thin-section	ID-TIMS
BN15-01	Biotite-gneiss I	C1	-	Yes
BN15-02	Biotite-gneiss I	C1	Yes	Yes
BN15-3/4/5	Pegmatite	C1	-	Yes
BN15-06	Amphibolite	C2	Yes	Yes
BN15-07	Pegmatite	C2	-	Yes
BN15-08	Cataclasite	A	Yes	Yes
BN15-09	Amphibolite	A	Yes	Yes
BN15-10	Biotite-gneiss II	A	Yes	Yes
BN15-11	Pegmatite	C2	Yes	Yes
BN15-12	Pegmatite	C2	Yes	Yes
BN15-13	Pegmatite	C2	Yes	-

Table 4.1: Sample BN15-01 and sample BN15-02 are considered identical, and therefore only one thin section was produced. The BN15-3/4/5 sample contain three samples taken from the same pegmatite vein. Pegmatite BN15-07 and BN15-12 is from the same vein, and therefore only thin sections from one of the samples was produced. The BN15-13 pegmatite was only used for thin section due to difficulties separating the pegmatite lens and gneiss in the crushing process.

4.4 Sample preparation

A total of 13 samples were collected for either petrographic descriptions or geochronological analysis by ID-TIMS, or both. Both methods requires sample preparations, which will be presented here.

4.4.1 Thin section

A 0.5cm thick slice of a preferred section in each sample were cut with a diamond saw to fit on a microscope glass slide. The sample was then handed to Mr Salahalldin Akhavan, at the thin section laboratory at the Department of Geosciences at UiO. After several rounds of grinding and polishing, the end result was a 30 μm thin slice of each sample glued to a glass slide. The produced thin sections were then studied and described using a transmitted light microscope, using Plane Polarized light and Cross Polarized light for petrographic observations.

4.4.2 Mineral separation

The selected samples for geochronological analysis, had to be prepared before they could be analyzed. The first step in this series of preparations, was mineral separation.

The solid rock samples were first washed and then crushed into smaller pieces with a jaw crusher followed by a crushing in a retsch cross beater mill. The crushed material was then washed across a Wilfley table, with the purpose of separating off the lightest minerals together with dust from the crushing process, and enriching the heavier mineral grains. The remaining fraction was then dried before manual separation using a 250 μm sieve, enabling the smallest grains to pass. The grains < 250 μm then went through a magnetic free fall separation to extract the magnetic grains. The remaining non-magnetic fraction was then separated using heavy liquid (diiodemethane 3.325 g mL^{-1}), where only the minerals of greater density than the liquid were able to sink down and were then drained out. This heavy and final fraction was then investigated under a a binocular microscope, were grains of interest were picked out with the help of tweezers in alcohol. For one sample (BN15-09) a Frantz isodynamic separator had to be used, due to the amount of magnetic material remaining after heavy liquid separation. The «Frantz» is a more sophisticated magnetic separator, and by using different angles and magnetic forces the amount of sample material was decreased, making further investigation under the microscope easier.

4.4.3 Abrasion

After picking the grains of interest, abrasion was the next step in the preparation procedures. The idea behind abrasion, is to get rid of the parts of the grains that have most likely experienced lead loss. For monazite, titanite, rutile and metamict-zircon, marginal areas of the grains were removed using air-abrasion, using the method described by **(Krogh 1982)**. For the best looking zircon grains (on basis of morphology, color and transparency), chemical-abrasion (annealing) was used. This method selectively dissolves damaged or altered domains of the zircon, regardless of their position within the grain **(Schoene 2014)**. The method improves precision and accuracy considerably, but can only be applied to not too strongly metamict zircons. Other grains would dissolve completely. The method is described in detail by **(Mattinson 2005)**.

4.4.4 ID-TIMS

Mineral samples were washed in dilute HNO_3, H_2O and acetone, in a ultrasonic bath to remove any contamination. The samples were then put on a hot plate to dry before weighing. Each sample was weighed on a microscale, before they were spiked with a mixed ^{202}Pb-^{205}Pb-^{235}U tracer and dissolved in teflon bombs in a oven at c.195˚C for 5 days (zircon and rutile) or teflon savillex-vials on a hotplate at c. 125˚C for 5 days (monazite and titanite). Isotope dilution (ID-) refers to the process of spiking a sample with a known quantity of tracer isotopes, used to determine the U-Pb ratio during the measurements, to convert ratios measured by mass spectrometry to moles of sample isotopes **(Schoene 2014)**. The zircon, titanite and rutile were dissolved in HF and a drop of HNO_3, while the monazite was dissolved in 6N HCl. Zircon samples weighing more than 0.001 mg, and monazite, titanite and rutile samples were chemically separated using micro-columns and anion-exchange resin, following the method outlined by **(Krogh 1973)**. The resin in the columns retains U and Pb, as other cations get washed out. Columns with zircon, monazite and titanite were treated with HCl, while

columns with rutile solution were treated with HCl and HBr. U and Pb were extracted using HCl and H_2O and added a drop of H_2PO_4. The extracted solution was then dried down and loaded on a Re filament with silica gel, ready for measuring. A summarizing sketch showing the most essential operations of the ID-TIMS method can be seen in **figure 4.2**.

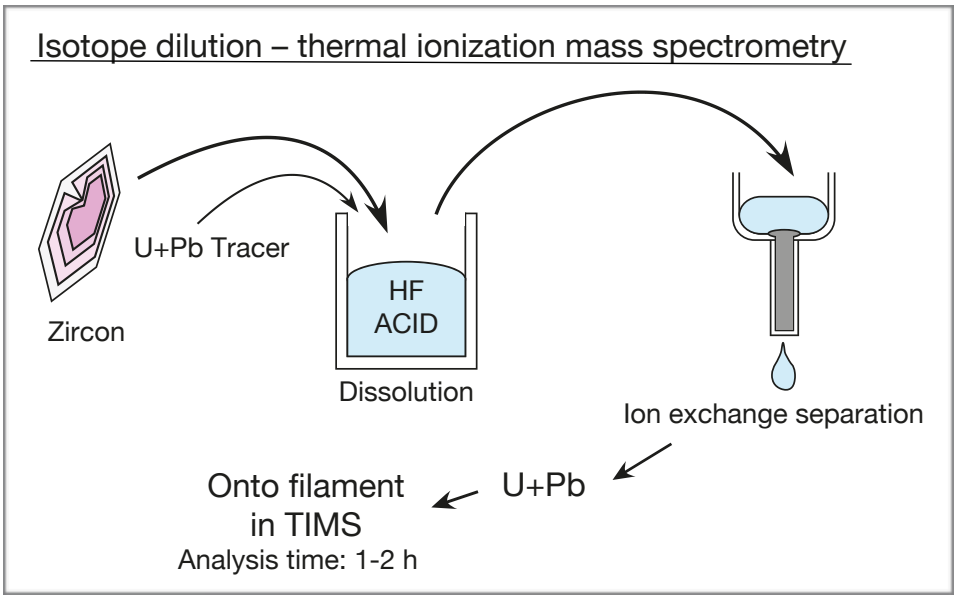

Figure 4.2: Simplified sketch of the ID-TIMS method. The grain and the tracer goes in the teflon bomb for dilution, followed by the micro-column containing the resin that retains U and Pb. Modified from **(Schoene 2014)**.

Chapter 5: Descriptions

5.1 Introduction

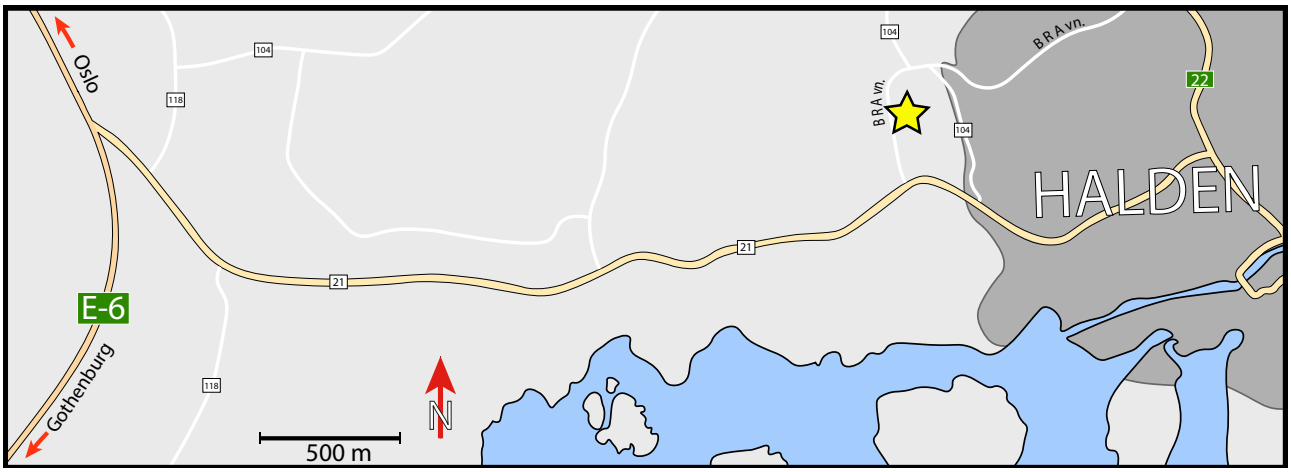

Figure 5.1: Map of the territory north of Iddefjord. The location of the field-area is marked with a yellow star, 2 km west of Halden city center.

For a better overview of the field-area it is advised to fold-out the complementary figure, found in appendix D. A compressed sketch of only the outcrop-surfaces, with lithological interpretations, can be seen in figure 5.2.

In this chapter the field-descriptions will be presented in two parts. First with a lithological description on macro- and micro-scale, followed by a systematic presentation of the structures observed in field. The field area comprises a 250 meters long (in total), and 6 meters high (at the highest), roadcut oriented directly N-S, located across the street of the University College of Østfold, in Halden. The roadcut consists of three pristine saw-cut outcrops, and displays a cross-section through gneisses and amphibolites of Paleoproterozoic to Mesoproterozoic age, in the Østfold segment of the SLM formation **(Larsson 1956, Lundegårdh 1958).** The latter is dominated by paragneisses intruded by plutonic bodies (now orthogneisses) during successive stages **(Graversen & Pedersen 1999).** In a map showing the bedrock of the Oslo-Region by **Berthelsen et al. (1996)**, the area is mapped as an biotite-muscovite-gneiss within the Østfold complex, truncated by the Iddefjord granite to the west and south, and the Ørje Mylonite Zone to the east and north.

The three individual outcrops are labeled A, B and C, from south to north respectively **(fig 5.2)**. These vertical walls of rock have been cut with a helical diamond wire, similar to the technique used in marble quarries, i.e. in the Apuan Alps in Italy. First, a horizontal drill hole is made along the base of the intended section. Second, a vertical hole is drilled straight down from the top at one end until it meets the horizontal hole, creating a path for a diamond wire to be thread. Then the wire saws its way through the rock as it is being rotated by heavy machinery. From a geologist's perspective this method of forming roadcuts is highly appreciated and the quality of the outcrops makes detailed observations possible.

> Four main lithologies are identified in the outcrops: Two grey to light grey biotite-gneisses, several dark amphibolite clasts and light veins of intruding pegmatites (see fig 5.2).

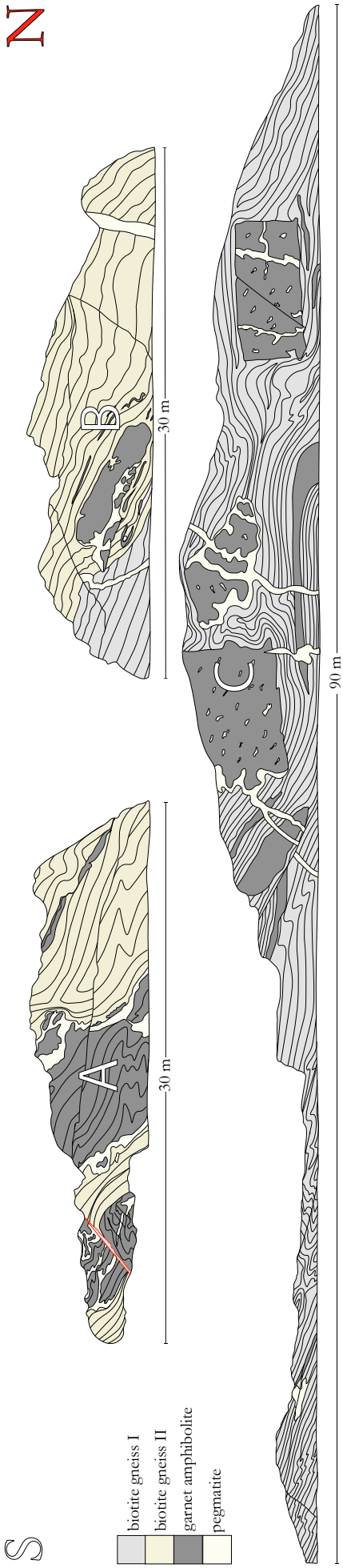

Figure 5.2: Sketch of the observed outcrops, with lithological interpretations. The sketches are to scale, presenting outcrops A, B and C from south to north respectively. The figure is based on hand drawn sketches from the field-book, re-worked in Adobe Illustrator.

5.2 Lithological descriptions

5.2.1 Biotite-gneiss I

Macroscopic description: The rock is mainly composed of white quartz and gray feldspathic minerals, together with dark minerals, most of which are biotite. The general grain size is fine to medium, and the gneissic texture is defined by the concentration of the minerals in bands. The described sample can be seen in **figure 5.3.** This gray gneiss is the main lithologic unit in outcrop C. It is also observed near the base in the southern part of outcrop B **(see fig 5.2)**. This is the darkest of the two observed gneisses in the outcrops, and the border between them is characterized by a rapid change in the orientation of the foliation, as well as a change in color. Contrasts between light and slightly darker bands defines a foliation. The foliation is dipping gently towards the north in the segment observed in outcrop B and the southern part of outcrop C. Further north in outcrop C the orientation of the foliation gets more variable with disharmonic folds connected to the presence of large amphibolite bodies.

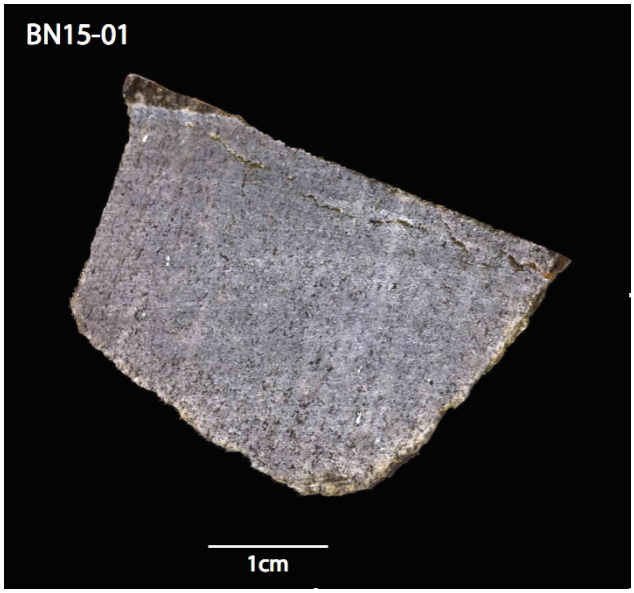

Figure 5.3: Hand sample of biotite-gneiss I (BN15-01 & BN15-02).

On top of the southern part of outcrop C, a few surfaces were available for measurements. The surfaces measured, and the lineation can be seen in **figure 5.4.** The foliation gave following orientations (strike/dip): 286/18, 276/15 and 288/16. A lineation was also measured (trend/ plunge): 330/18. The data have been plotted in stereonet **(fig 5.5)**.

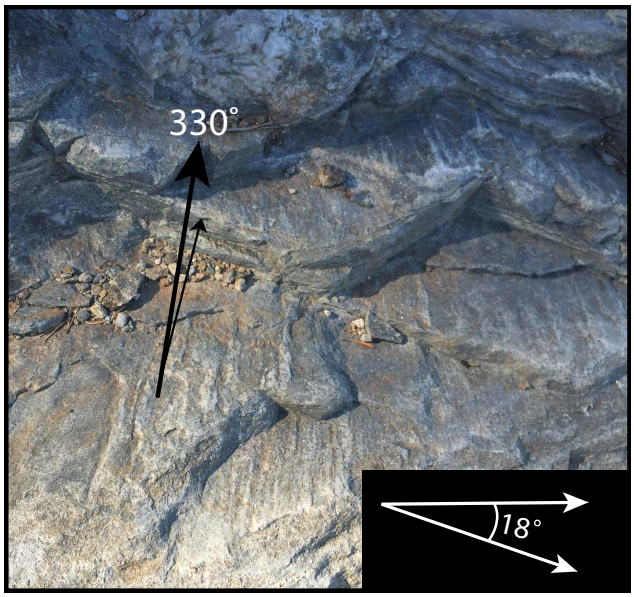

Figure 5.4: Lineation measured on foliation surfaces on top of outcrop C. The trend of the lineation is 330°, and the plunge is 18°.

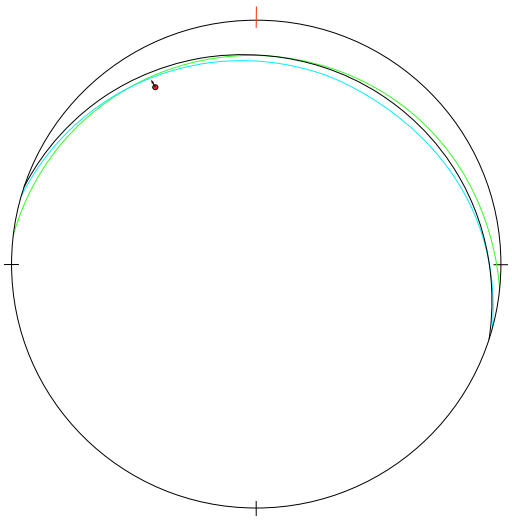

Figure 5.5 (to the left): Stereonet plot of measured strike and dip of the foliation in biotite-gneiss I. One point of measured trend and plunge (330/18) on the observed lineation is also plotted.

Microscopic description (in order of abundance): Quartz is the dominant matrix mineral, forming a granular mosaic of anhedral colorless grains in PPL, 0.2-1 mm across. The grains exhibit weak undulose extinction in XPL and cover 40% of the sample. Plagioclase occurs as 0.5-3mm large trains of anhedral grains with gray body color in PPL, constituting approximately 20% of the rock. Secondary growth of sericite is seen in most of the grains, but polysynthetic twinning can be seen in XPL where the plagioclase is less altered. Alkali feldspar makes up 20% of the sample as colorless anhedral grains in PPL, 1-2mm across, and crosshatched twinning in XPL. 5-10% of the section consists of platy tabular grains of biotite, displaying pleochroism upon rotation, with body colors from light to dark brown in PPL. The biotite grains have a preferred orientation. Muscovite makes up >1% of the sample, 2_{nd} order pink to blue interference color in XPL, and no preferred orientation, platy habit. Opaque phases make up 5% of the sample. Zircon and monazite occur as accessory phases.

Classification: Based on the investigations described above, the rock is classified as an biotite-gneiss, with <10% biotite.

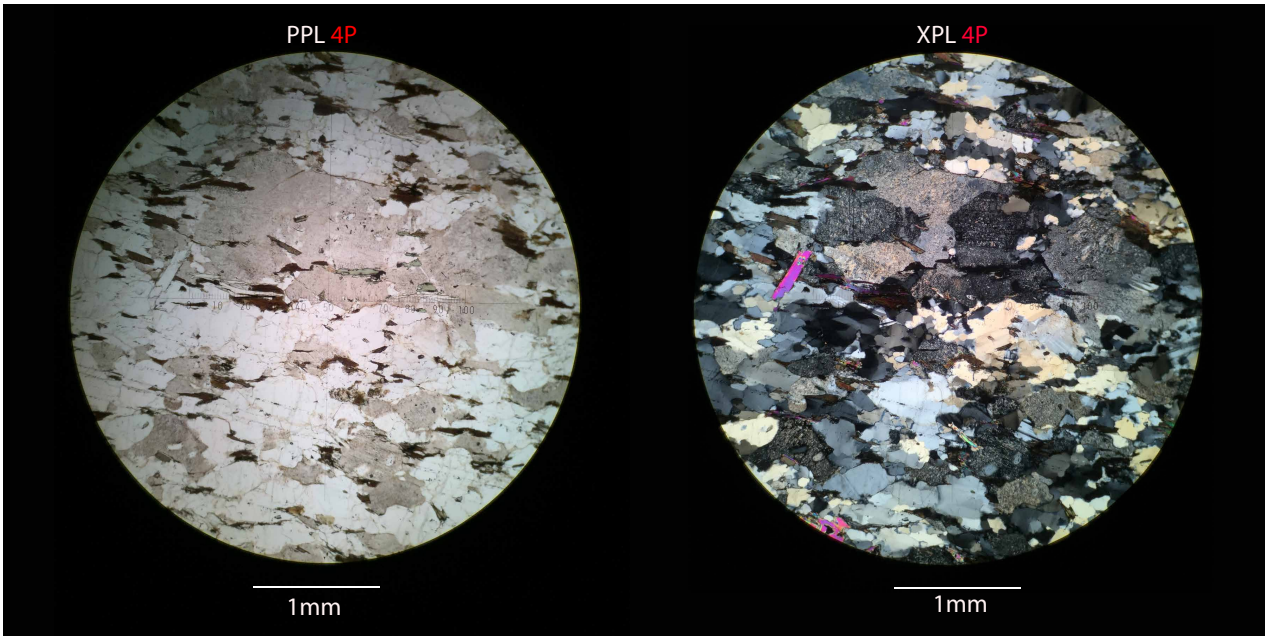

Figure 5.6: Biotite-gneiss I, sample BN15-01. Representative region of the thin section as seen through the ocular of the microscope in PPL **(left)** and XPL **(right)**. Magnification 4P.

5.2.2 Biotite-gneiss II

Macroscopic description: The rock is composed of the same minerals as the biotite-gneiss I, described above. The banding of the minerals is not as well defined as in biotite-gneiss I, and the grain size is in general coarser, especially for the lighter minerals. The amount of light minerals is increased. The described sample can be seen in **figure 5.7**. This grey gneiss is the main lithology in outcrops A and B. This gneiss has a slightly lighter hue than the biotite-gneiss I, described above. The border between the biotite-gneisses can be seen in **figure 5.8** Mainly because of the higher amount of lighter materials. The rock looks very deformed, and the grain size is larger compared to the first biotite gneiss. A foliation caused by repetitive layers of light and slightly darker minerals is observed in this rock as well, but the orientation is quite variable within small distances. Measurements of the foliation show quite divergent results in strike **(table 5.1)**, the dip is only measurable in the wall of the outcrop, and therefore estimated ≥40°.

Table 5.1: Foliation measurements

Southern Segment of outcrop A	Northern segment of outcrop A
224°	269°
237°	280°
232°	279°

(Dip measurements, ≥40°)

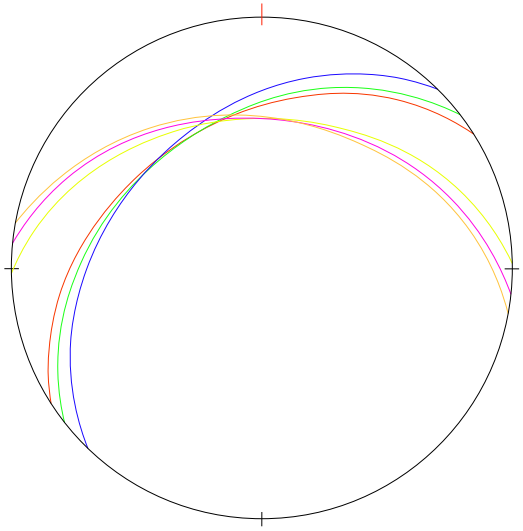

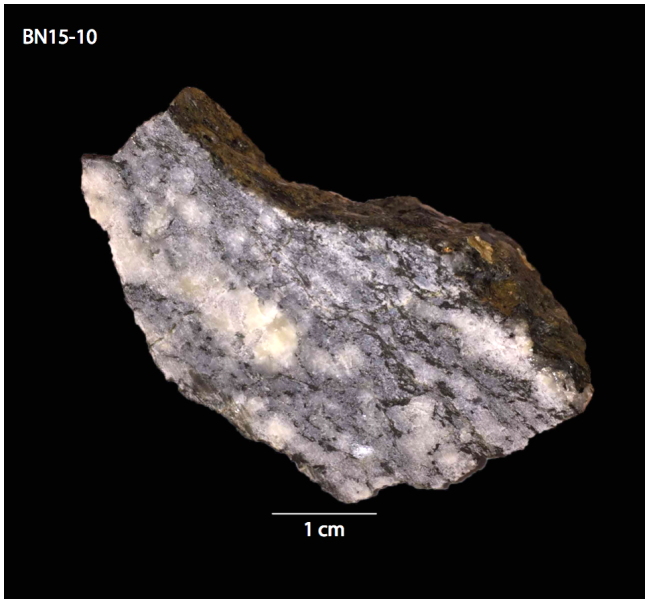

Figure 5.7: Hand sample of biotite-gneiss II (BN15-10).

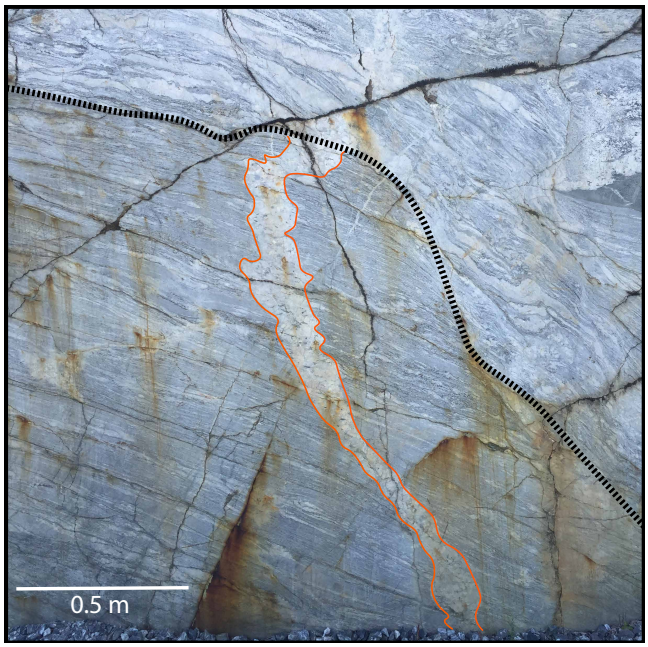

Figure 5.8: The boundary between biotite-gneiss I (bottom) and biotite-gneiss II (top), seen in southern part of outcrop B.

Figure 5.9 (to the left): Stereonet plot of measurements presented in **table 5.1,** with the estimated dip ≥40°.

Microscopic description (in order of abundance): Quartz is the dominant matrix mineral, makes up ≥50% of the sample, and makes a mosaic of colorless anhedral grains in PPL. Grain size up to 2mm in diameter, and weak undulose extinction. Plagioclase occurs as 1-3mm large anhedral grains with gray color in PPL, covering approximately 25% of the section. Secondary growth of sericite covers most of the grains, but polysynthetic twinning can be seen in XPL where the plagioclase is less altered. Smaller amounts of alkali feldspar can be observed with cross-hatched twinning in XPL. Mica occurs in the matrix and in cracks. ≥10% of the sample is made up of mica (90% biotite, 10% muscovite). Opaque phases make up >2% of the sample, with a variety of grain shapes from anhedral to perfect cubic (Pyrite). Zircon appears as an accessory phase.

Classification: Based on the investigations described above, the rock is classified as an biotite-gneiss, with <10% biotite.

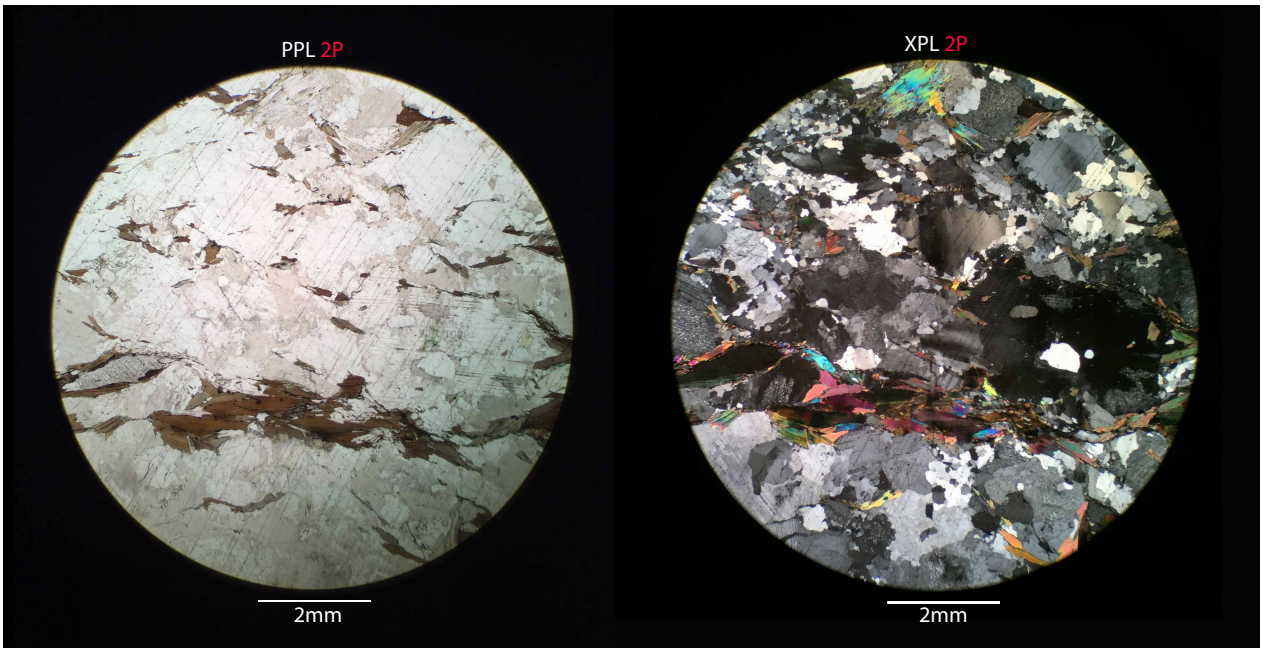

Figure 5.10: Biotite-gneiss II, sample BN15-10. Representative region of the thin section as seen through the ocular of the microscope in PPL **(left)** and XPL **(right)**. Magnification 2P. Scratching from the polishing of the thin sections can be seen oriented NE-SW (especially in PPL).

5.2.3 Garnet-amphibolite

Macroscopic description: The darkest lithology in the observed outcrops, standing out from the surrounding gneisses and the intruding pegmatites. The rock is fine grained and contains high amounts of hornblende, which can be seen on weathered surfaces and fresh fractures. Igneous origin and much more homogenous than the other observed lithologies. The rock occurs as isolated, lens-shaped fishes, blocks or boudin-like bodies in all three outcrops, with contrasting sizes from 0.5 - 8 meters (longest horizontal axis). Some of the bodies look massive and homogenous on the macro-scale, while others are internally deformed and contain slivers of light lithologies (see below). The amphibolite invariably contains red garnet, ranging in size from 0.2-1.0 cm across.

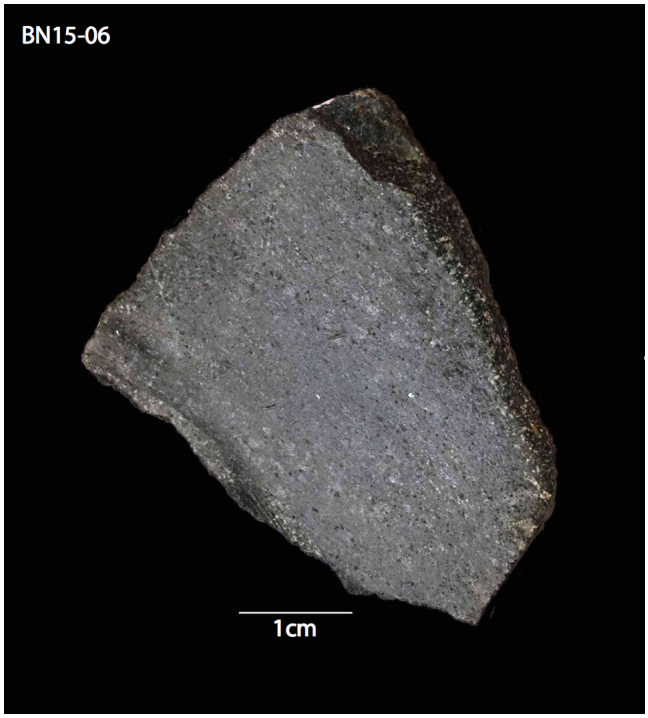

Figure 5.11: Hand specimen of Garnet-amphibolite from outcrop C (BN15-06).

In outcrop C, large rectangular amphibolite bodies can be seen **(fig 5.13)**. Disregarding the pegmatite intrusions, these are the least deformed and most homogenous amphibolites observed in the roadcut, with no internal foliation, marginal amounts of light minerals and a small grain size. A hand specimen of this rock can be seen in **figure 5.11**. In outcrop A and B on the other hand, the amphibolite bodies are less homogenous and more sub-rounded in form **(fig 5.14)**. Most are incapsulated by coarse grained pegmatite veins, and contain slivers of light materials, making it possible to observe a internal deformation. The main mineral is hornblende, but also significant amounts of quartz and feldspars in slivers. The grain size is fine to medium grained. A hand specimen of this rock can be seen in **figure 5.12**.

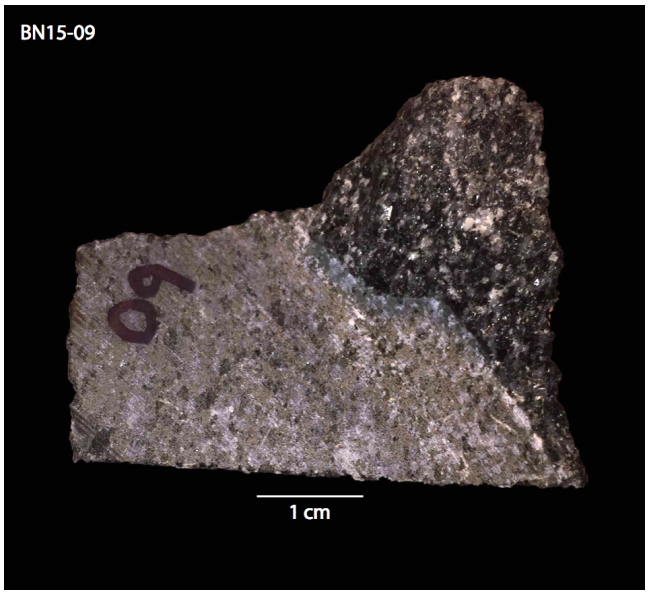

Figure 5.12: Hand specimen of Garnet-amphibolite from outcrop A (BN15-09).

Microscopic description (in order of abundance): With the differences in mind, two samples were described at the microscopic scale, separately. BN15-09 (from section A) and BN15-06 (from section C). For further details regarding sample positioning see **figure 4.1**, in the methods chapter.

(BN15-06) Subhedral to euhedral amphibole grains, 0.5 mm across with distinct 60/120 cleavages make up ≤70% of the sample. Pleochroic body color from green to pale brownish green, indicating hornblende. Smaller amounts of Augite occur, with simple twinning and pale yellow interference color. 0.1-1mm anhedral colorless grains of quartz occur in 5% of the sample, with undulose extinction in XPL. Plagioclase with secondary growth of sericite makes up >5% of the sample. Anhedral crystal shape, 0.1-1mm across, colorless in PPL. Large fractured porphyroblasts of garnet, 1,5-2,5mm across, occurs in zones in the thin section. Approximately 5% of the sample consists of garnet, believed to be Almandine. The fractured pieces are replaced at their rims by unidentified microcrystalline growth. High amounts of opaque phases (5%), 0.05-0.2mm across, mostly hematite and some ilmenite. Approximately 20% of the opaque grains have a microcrystalline rim/corona of an anisotropic mineral with high interference colour. Platy tabular grains of brown biotite make up >5% of the sample. Rutile, zircon and titanite occur as accessory phases.

(BN15-09) Anhedral 0.5-2 mm large Amphibole makes up ≥50% of the sample. Pleochroism from green to pale brownish green, indicating hornblende, with distinct 60/120 cleavage. Quartz occurs as colorless anhedral grains, 0.1-0.5mm across, and covers 20% of the sample. It has weak undulose extinction and uniaxial positive conoscopic figure in XPL. Plagioclase is seen in <20% of the sample, anhedral grains 0.5-2mm across, and heavily overgrown by secondary sericite. Less altered grains display polysynthetic twinning in XPL. Opaque phases make up ≤5% of the sample. Zircon and titanite occurs as accessory phases.

Classification: Based on the investigations described above, both rocks are classified as garnet-amphibolites (with almandine garnets).

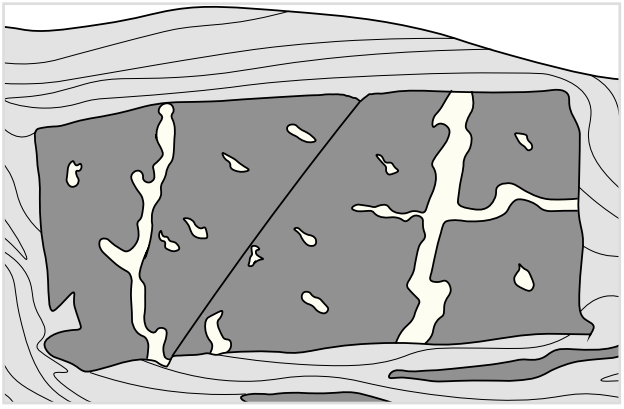

Figure 5.13: Sketch of rectangular garnet-amphibolite observed in outcrop C. Homogenous without internal foliation, similar to sample BN15-06. The body is 6 x 2.5 meters.

Figure 5.14: Sketch of the garnet-amphibolite body observed in outcrop A. Contains slivers of light material indicating an internal foliation seen in the sketch, similar to sample BN15-09. The body is 7.5 x 4 meters.

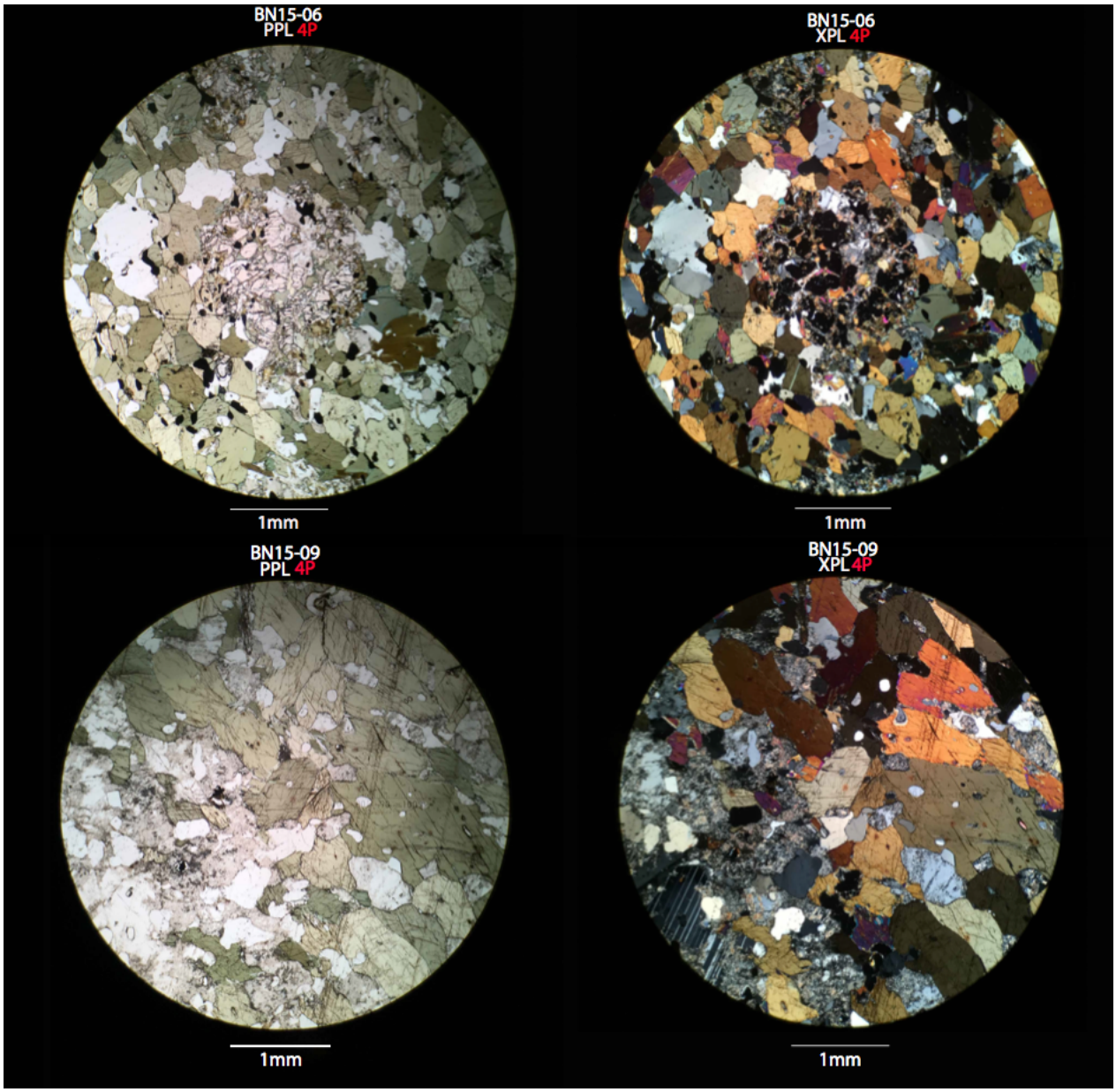

Figure 5.15: Garnet-amphibolite samples BN15-06 **(top)** and BN15-09 **(bottom).** Representative regions of the thin sections are seen through the ocular of the microscope in PPL **(left)** and XPL **(right)**. Magnification 4P. In the BN15-06 sample a large broken garnet grain can be seen.

5.2.4 Pegmatites

The pegmatites are easily distinguished from the surrounding lithologies as the lightest rock in the outcrops. Observed as veins or lenses of coarse grained intrusions, in all three outcrops, cutting through one or more of the surrounding lithologies. The diversity in the appearance of the pegmatites and how they relate to the surrounding lithologies is well displayed in outcrop C. The observations indicate three or possibly four different generations of pegmatites:

Gen. A) «Patches» or lenses of smaller pegmatites within the rectangular garnet-amphibolite bodies in outcrop C. Sample BN15-13.

Figure 5.16: Sketch of «patch»-pegmatite constrained in a rectangular amphibolite body in outcrop C. Pegmatite generation A.

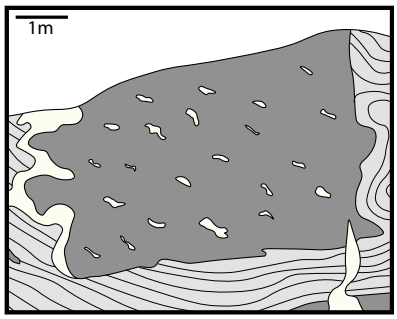

Gen. B) Pegmatite veins constrained within the amphibolite bodies themselves, not cutting into the gneiss. Observed in the northernmost rectangular amphibolite body in outcrop C. Sample BN15-11.

Figure 5.17: Sketch of pegmatite generation B.

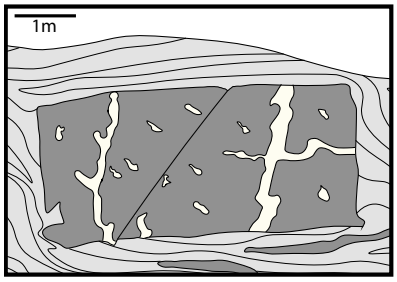

Gen. C) Pegmatite veins in outcrop C cutting through the whole outcrop and its lithologies, seemingly unaffected by later deformation. Sample BN15-12.

Figure 5.18: Sketch of observed pegmatite vein cutting through the lithologies. Generation C.

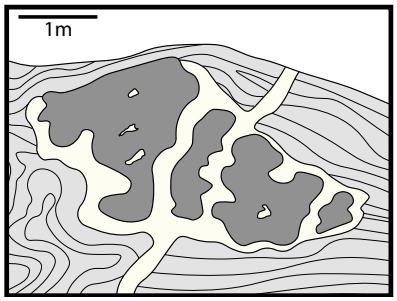

Possible Gen. X) Pegmatite patch in the gneiss of outcrop C, with a pinkish hue different from the other observed pegmatite generations. Only seen at one place in the outcrop. No samples has been taken of this generation.

Description in outcrop: Grain sizes vary from under 1 cm to 7-8 cm, generally related to the size of the intruding vein. The largest vein is seen in the northern part of outcrop B, measuring 60 cm across and cutting steeply through the gneiss. The other veins observed are typically 10-30 cm wide, or even smaller. In hand specimen the different samples of pegmatite shares several features. They are mainly composed of coarse grains of quartz and feldspars. The sample of pegmatite generation C is the coarsest (BN15-12). It also contains several large grains of muscovite, which are not seen in the other samples. The samples of pegmatite generation A and B (BN15-11 and BN15-13 respectively), look very similar in hand specimen. Both are milky white in color, and contain inclusions of the surrounding amphibolite. The described sample can be seen in **figure 5.19**.

Description of thin section: With these differences in mind, the three sampled generations of pegmatites (A, B & C) will be described individually. It is important to be aware that a thin section study may not give a representative result when describing very coarse grained rocks, i.e. pegmatites. The coarser the rock, the less grains fit in the thin section, and therefore less grains are available for description.

Gen. A: (BN15-13) Quartz occurs as 0.1-0.4 cm large anhedral colorless grains in PPL. Plagioclase occurs as altered grains of sericite, with a barely visible twinning in XPL. The plagioclase and quartz occurs in equal amount (50/50).

Gen. B: (BN15-11) Quartz occurs as 0.5-1.0 cm large anhedral colorless grains in PPL, and covers 60% of the sample. The remaining 40% are covered by plagioclase, which is observed as gray subhedral grains in PPL, and characteristic parallel twinning in XPL. The grains are altered to sericite in some places, and are 1.0 cm across. Smaller cracks in the plagioclase are filled with quartz.

Gen. C: (BN15-12) Alkali-feldspars cover 60% of the sample, where one single grain of microcline with crosshatched twinning covers nearly half of the thin-section. One large grain of muscovite, 1,5 cm long with vivid 2nd order interference colors covers 20%. Altered grains of Plagioclase, now microcrystalline sericite, is seen in 5-10% of the sample, and some smaller grains of quartz.

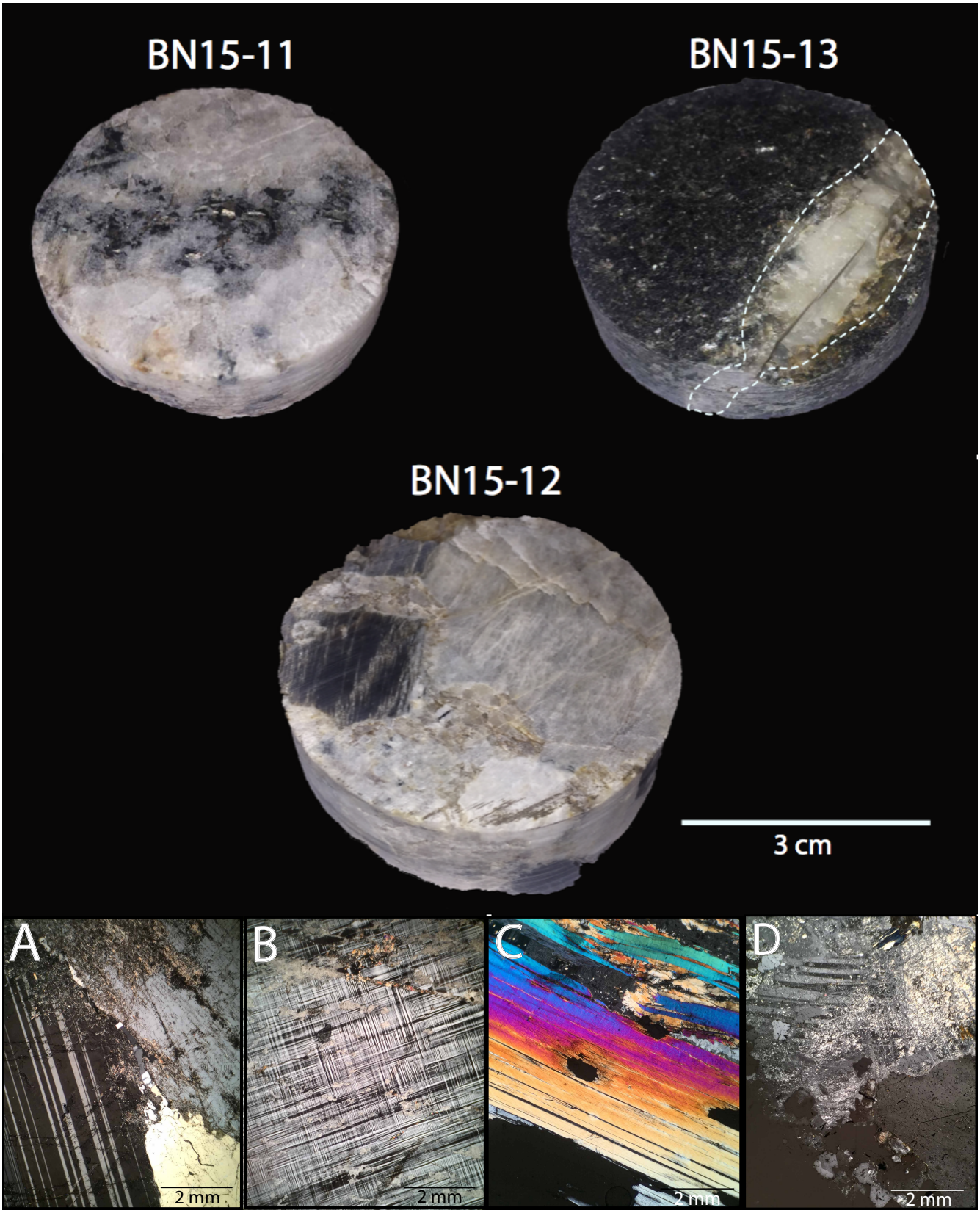

Figure 5.19: The three pegmatite samples collected in outcrop C. **Top)** Pictures of the pegmatite samples. **A)** BN15-11 (XPL). Two large grains of plagioclase, together with a quartz grain down to the right. Sericite overgrowth on the plagioclase in the top left corner. **B)** BN15-12 (XPL). One large grain of microcline covers the field of view, displaying characteristic tartanplaid twinning. **C)** BN15-12 (XPL). Large muscovite grain, the same grain as the large «quadratic» grain seen on the picture of sample BN15-12 above. **D)** BN15-13 (XPL). A feldspar grain gradually altered to sericite. A large quartz grain is seen down to the right, with some smaller inclusions.

5.3 Structural descriptions

5.3.1 Introduction

The outcrops display an array of structures formed under shifting p,T-conditions and strain rates and intensities. In this subchapter these structures will be described, starting with the oldest traceable (high p,T, visco-plastic) to the youngest (low p,T, brittle) deformation events. The structures that will be outlined are shear zones with shear indicators (porphyroclasts, porphyroblasts), folds, boudins and faults, in that order **(fig 5.20)**. Where the folds, boudins and faults contain important information regarding the thermo-tectonic evolution will be discussed in **chapter 7**. Observations on the macro- and micro-scales are included in the descriptions.

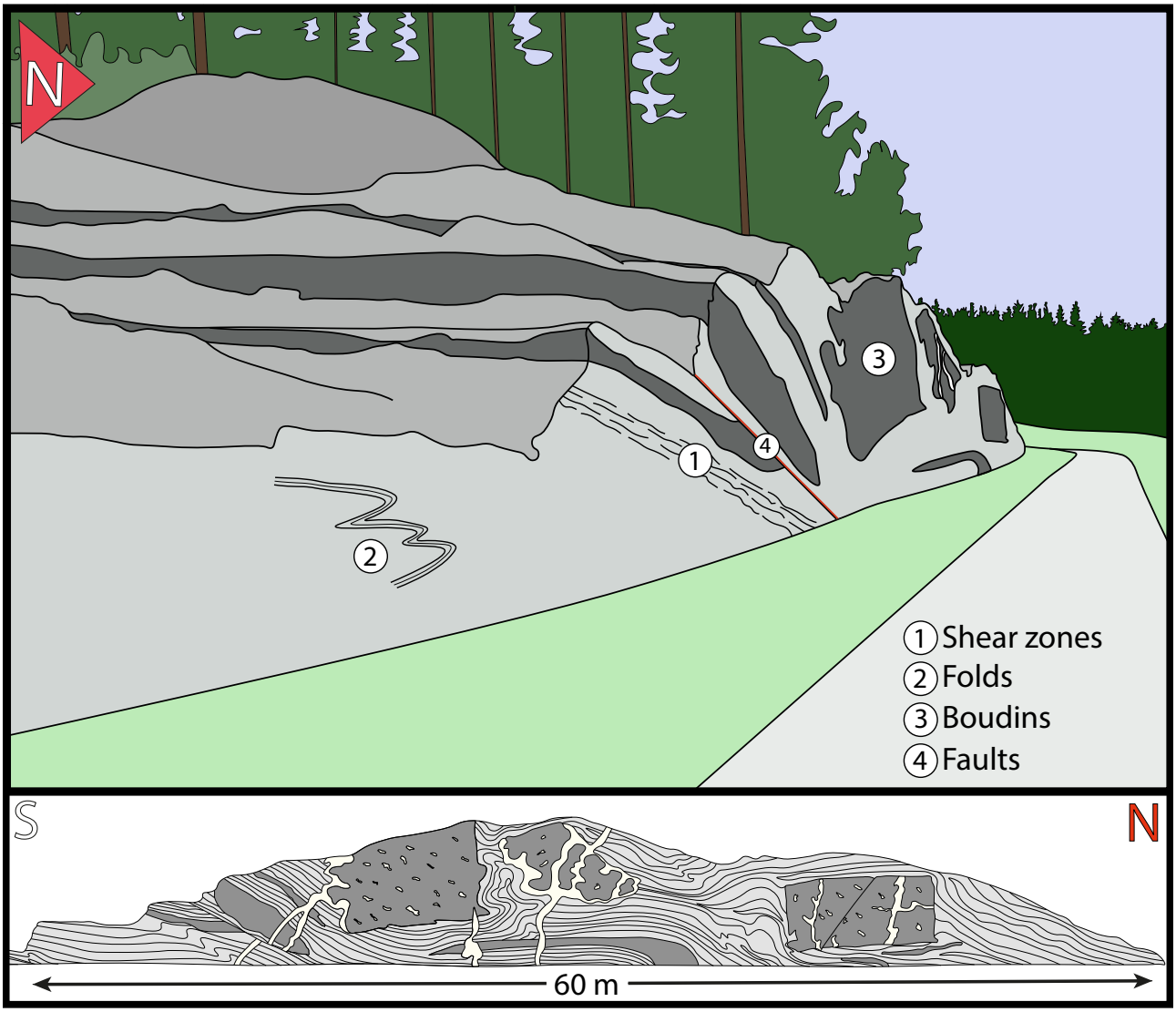

Figure 5.20: Illustration of the structures that will be outlined in the following descriptions, observed in the northern half of outcrop C. **1)** Shear zones, **2)** Folds, **3)** Boudins, **4)** Faults. The sketch on the **top** is for illustrative purpose. The sketch on the **bottom** shows the observed structures in the outcrop and is to scale.

5.3.2 Shear zones

Tabular zones with notably higher strain than the surrounding rock are seen several places in the outcrops, on the cm to meter scale. The zones can be subdivided into those only containing a visco-plastic deformation element (ductile), and those containing a visco-plastic and a brittle element (semi-ductile). The visco-plastic high-strain zones are the biggest in the outcrops and mostly dipping towards north **(fig 5.21A)**. The high-strain zones with both visco-plastic and brittle components are typically observed as 1-2cm thick zones with a high density of sharp discontinuities (cracks) oriented normal to each other in the center, stepping away towards left and right **(fig 5.21B).**

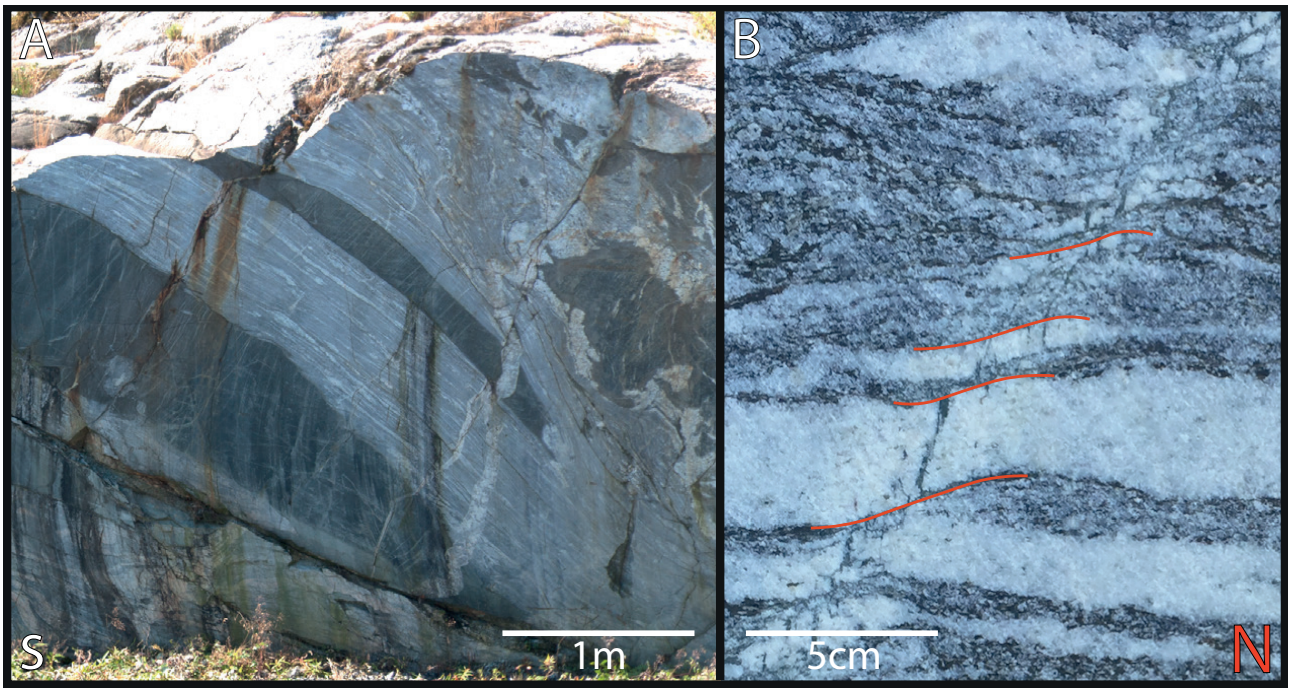

Figure 5.21: A) Ductile shear-zone dipping towards north. A pegmatite vein can be seen as it cuts across the zone, giving a relative age younger than the deformation. **B)** Semi-ductile shear-zone on the cm-scale. Visco-plastic deformation elements marked with red, and brittle step-away fractures can be seen in the center.

5.3.3 Shear indicators

Porphyroclasts and porphyroblasts are observed embedded within high-strain zones. These small scale macroscopic indicators of coaxial and non-coaxial deformation consist of feldspars and quartz, with variance in size, from 1 to 15 cm in diameter.

Porphyroclasts are observed in relation to s-c structures. These slip surfaces or shear bands obliquely transects (and rotates) the foliation in the biotite gneiss observed in affiliation to feldspar and quartz rich veins exposed to extension. The s-c structures observed indicate a polarity in shear sense, with movements in both directions. In **figure 5.22A** an example of this can be seen. Textbook examples of clasts with symmetric tails, asymmetric tail and tails showing a rotational component are also observed. In **figure 5.22B**, an example of a clast is seen. The tail on the right side of the clast indicate an anti clockwise rotation (δ-type candidate), while the tail on the left side is more symmetric (ϕ-type candidate).

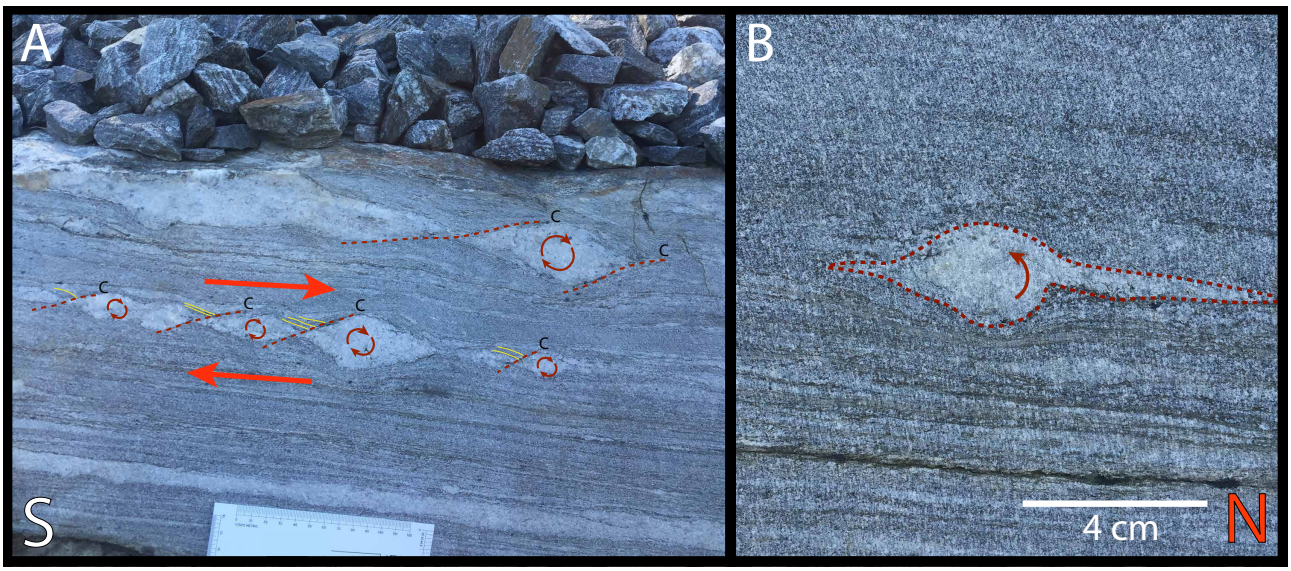

Figure 5.22: Composite figure of shear sense indicators observed in the center of outcrop C. **(A)** Shear bands transecting the foliation in the biotite gneiss and rotation of the clasts. Indicating a top towards the north movement. **(B)** Example of clast seen in the center of outcrop C.

Porphyroblasts are observed in both the biotite-gneiss (blasts of quartz and feldspar) and in the garnet-amphibolite (garnet). The porphyroblasts observed in the biotite-gneiss bear many resemblances to the porphyroclasts seen in the same rock, but the blasts display a texture of grains affected by grain-size enlargement during metamorphism and deformation **(fig 5.23A)**. The porphyroblasts seen in the amphibolites consist of singular grains of garnet, with variance in size from 0.2-1.0 cm in diameter. The garnets generally appears fractured with secondary growths, but in one pristine grain, trains of quartz and opaque minerals possibly indicating an primary foliation (S0) were observed **(fig 5.23B)**.

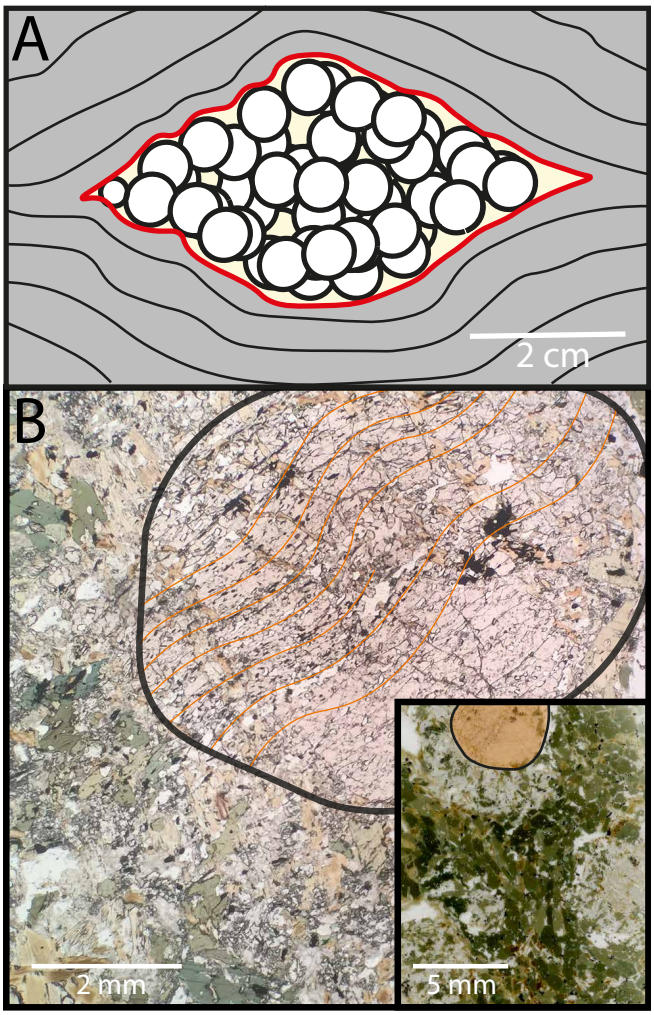

Figure 5.23 → : Composite figure of the porphyroblasts seen in the biotite-gneiss and in the garnet-amphibolite. **A)** Illustration showing a porphyroblast in the gneiss consisting of coarse grains of quarts and feldspar. **B)**

5.3.4 Folds

As described in **chapter 5.2** (lithologic descriptions) the biotite-gneiss is characterized by a pronounced and variably oriented foliation. All three outcrops display folds with variable orientation, in which two fold-populations are identified.

Fold population FA

Macroscopic shear-folds occur on the cm- to meter-scale in the biotite-gneiss, the garnet-amphibolite and in the contact zone between these two lithologies (figure x). These folds are observed in the saw-cut walls, and only an estimated orientation of the fold-axes can be derived, with a strike to the NW-SE, with top-to-the-NE and –SW contraction. At one location, at the top of the southern part of outcrop C, two recumbent tight folds are found, with measured fold axes plunging 322° and 318° top-to-the-NE contraction and axial planes dipping 10° and 5° towards SW **(fig 5.24 and fig 5.25)**. The curvature of the inner arc matches the curvature of the outer arc, making them class 2 folds after Ramsay´s **(1967)** classification **(fig 5.25)**. These folds are interpreted to represent the same fold-population as the shear-folds observed in the saw-cut walls, and their relation and geometry are shown in **figures 5.24 and 5.26**.

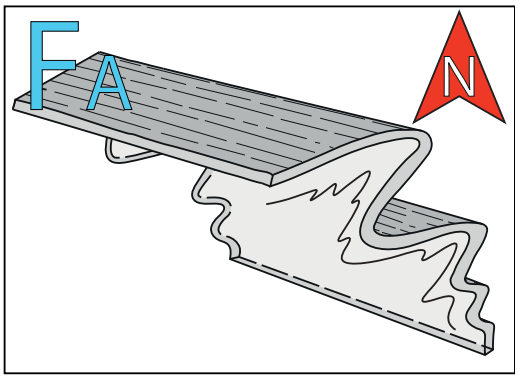

Figure 5.24: Conceptual sketch of fold population FA.

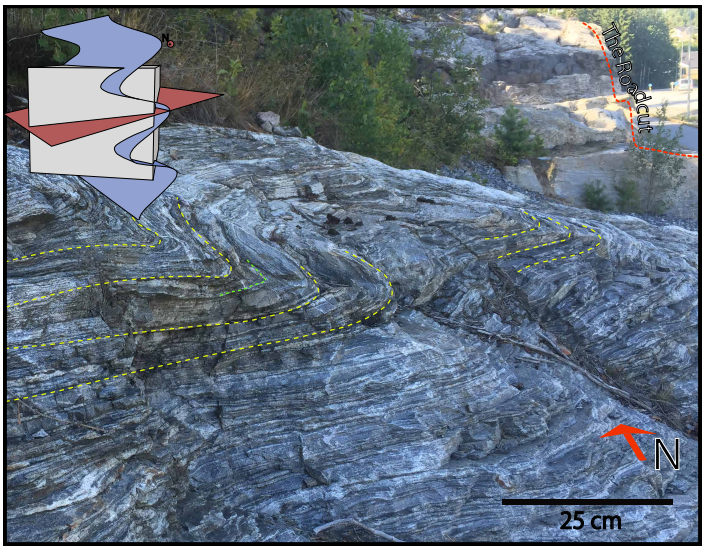

Figure 5.25: Fold-population FA, as seen on top of the southern part of outcrop C. A 3D model showing the orientation of the folds can be seen. The blue layer represents the folded surface and the red indicates the orientation of the fold-hinge. The depth in the figure is oriented straight towards N.

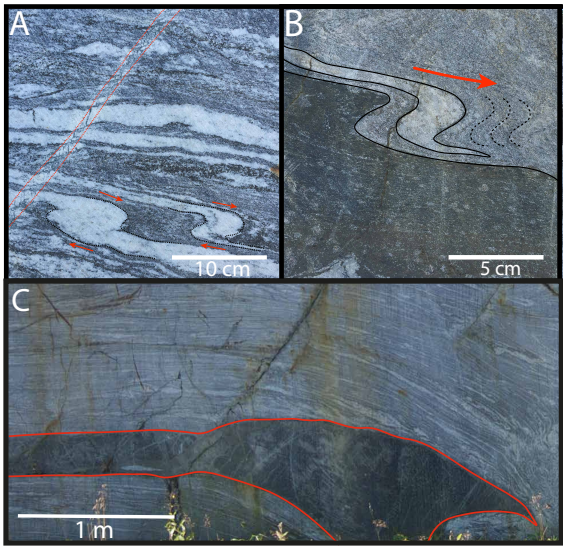

Figure 5.26: Composite figure of small scale folding in the outcrops. **(A)** Folding of two thin layers or veins of feldspar and quartz, converging towards north. A 2 cm thick zone of focused strain stepping down left is also seen. Picture from outcrop A. **(B)** Folding of the contact between garnet-amphibolite and biotite gneiss. Picture from outcrop A. **(C)** Folded garnet-amphibolite boudin, seen in outcrop C.

Fold population FB

Disharmonic neck-folds have been described separately although these may be contemporaneous with fold-population FA, but the conditions are different. This fold type is constrained to the shadow-areas behind the short flanks of the garnet-amphibolite boudins **(fig 5.27)**.

Figure 5.27 → : Disharmonic folds referred to as fold-population FB, here seen at the short-flank of a rectangular garnet-amphibolite boudin in outcrop C. A corner on the boudin is marked in red to point out visco-plastic deformation.

5.3.5 Fragmented garnet-amphibolites

Garnet-amphibolite boudins are seen throughout the whole roadcut, but they are especially prominent in outcrop C **(fig 5.28)**. Boudins with different geometry, from rectangular to lens-shaped, are observed. Classically the geometry largely reflect the strain geometry during formation. In three dimensions the boudins are observed as continuous layers in the section oriented W-E **(fig 5.28)**.

Two large rectangular boudins are seen in the outcrop, one near the center and a second in the northern part of the outcrop **(fig 5.28)**. These boudins measures 8x4 meters and 6x2.5 meters, respectively, and stand in strong contrast to the disharmonic folded biotite gneiss surrounding them. Their geometry strongly promoted brittle deformation mechanisms during formation. «Premature» extensional cracks are also seen in the boudins.

Immediately underneath the rectangular boudin in the center of the outcrop, a strongly strained and thin lozenge-shaped mafic body is seen **(fig 5.28)**. This body stand in strong contrast to the rectangular boudins, and certainly contain a larger component of visco-plastic deformation.

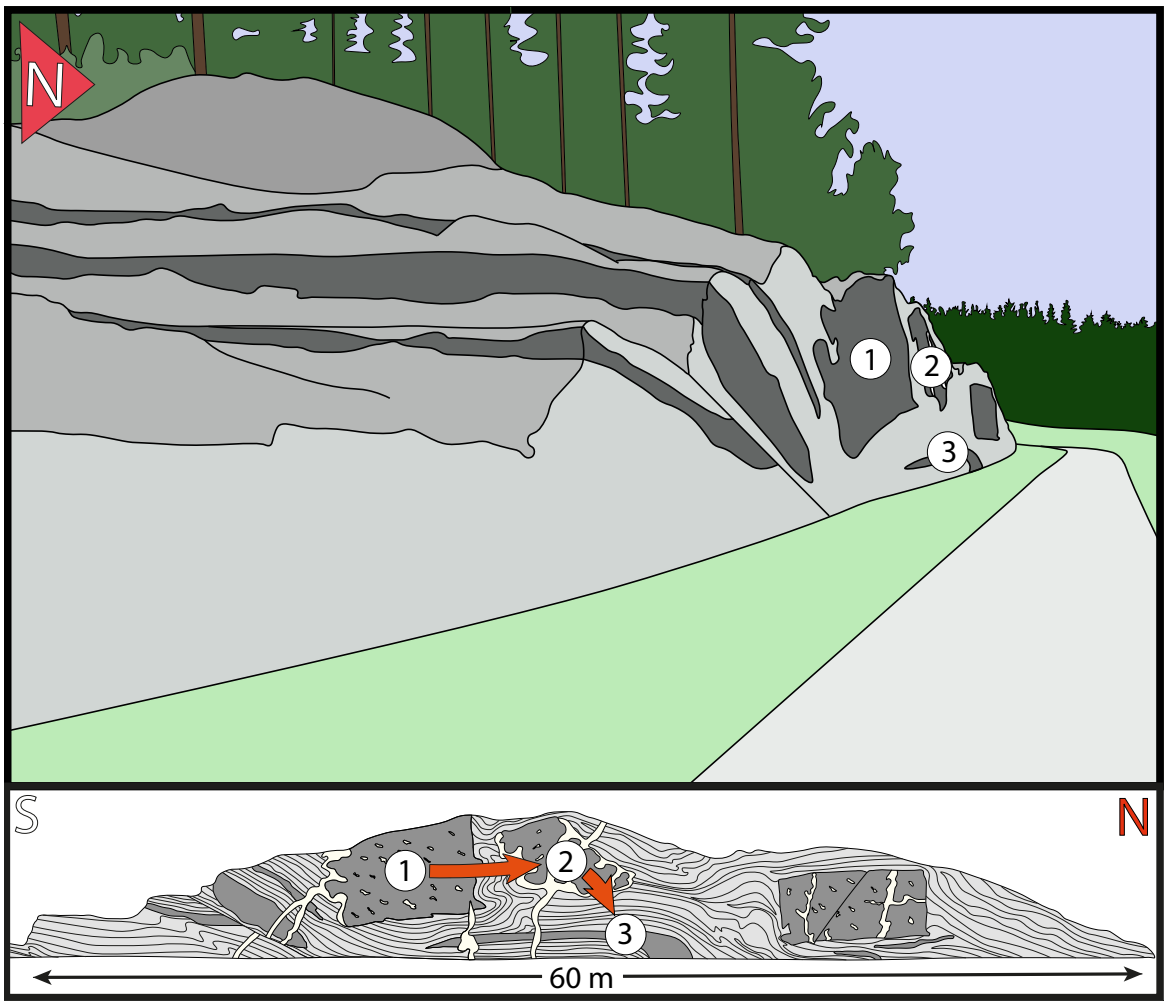

Figure 5.28: Illustration showing the different geometries of the garnet-amphibolite boudins observed in outcrop C. The numbers indicates increasing strain component, from 1 to 3, low to high.

5.3.6 Faults

Faults appear as discontinuities in the lithologies throughout the outcrops observed, with differences in orientation, fault anatomy, initial stress configuration and formation depth. The faults observed are separated into two «sub-categories»; faults containing a cohesive fault-rock and faults containing a uncohesive fault-rock (gouge). Examples of both are seen in all outcrops (A, B and C)

Faults with a cohesive fault-rock

The prime example, and the biggest fault with a cohesive fault core observed, is found in the southern part of outcrop A **(fig 5.29)**. The planar fault core, which consist of an ultracataclasite, dips 40° towards the south, and the fault core varies in thickness from 1 to 12 cm. Above the fault core, several drag-folds can be seen in the hanging wall, indicating an normal movements towards the south for the hanging wall **(fig 5.29A)**. In the footwall, several small synthetic faults can be seen, cutting through the internal folds in the garnet amphibolite **(fig 5.29B)**. This effectively makes it possible to measure absolute movement, which varies between 8-12 cm. Sample BN15-08 has been taken from the large fault core, for thin-section examination **(fig 5.28)**, and age calculation **(chapter 6)**. The thin-section

examination shows that the fault rock is non-foliated and consist of 90-100% matrix of grain size <0.1 mm. Making it a ultracataclasite after **Braathen et. al (2004)** classification scheme for fault rocks. Several lenses of less deformed fragments from the host rock or neighbor lithologies can be observed, consisting mainly of plagioclase and quartz. Lenses consisting of an older cataclasite (relative age) can also be observed, in sizes typically 1-2 mm across.

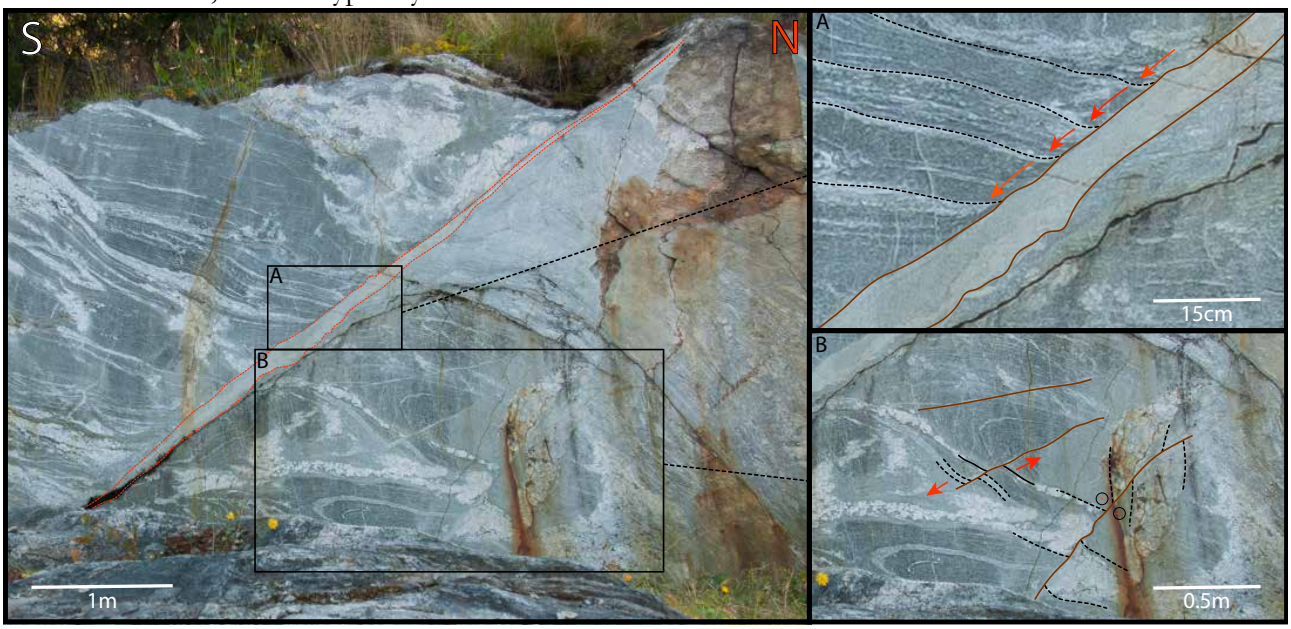

Figure 5.28: Compilation of figures related to the cohesive fault core in the southern part of outcrop A. **A)** Fault zone and drag folds in the hanging wall, dictating a normal top towards the south movement. **B)** Synthetic small faults in the foot wall. The fault in the middle has a top to the south movement. The lowermost fault is interpreted to have a top to the east movement, not captured by the two dimensional cross section.

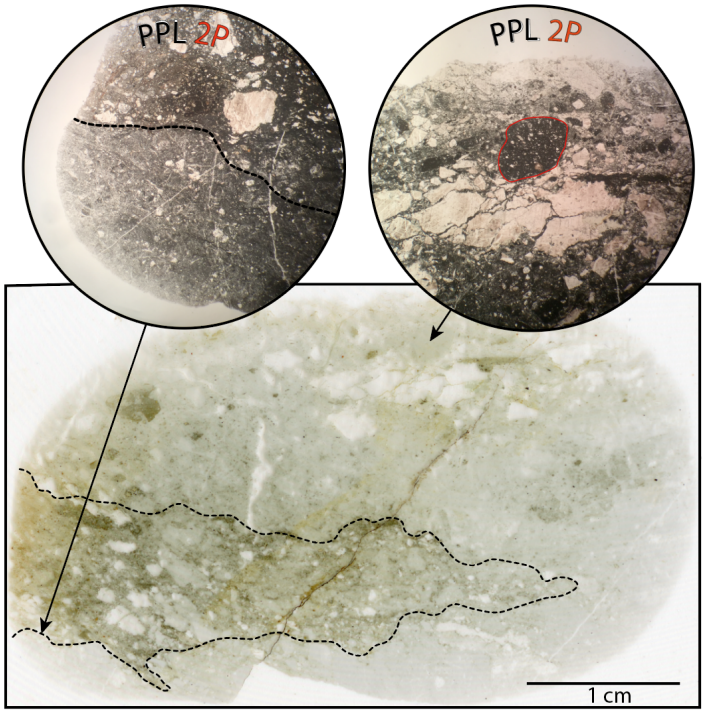

Figure 5.29: Thin section scan of the ultracataclasite sample (BN15-08), from the fault sone studied in outcrop A. Inset picture to the **left** shows the boarder between the crushed base of the fault core and the slightly less crushed zone above it. Inset picture to the **right** shows a lens of an older fault rock, marked with red. Both inset picture also shows light fragments of less deformed material from neighboring rocks.

In outcrop B and C, more examples of normal faults containing a cohesive fault-rock with a dip towards the south are observed. These faults have a thinner fault core than the fault observed in the southern part of outcrop A, and display big variations in the thickness of the damage zone connected to changes in dip. The fault presented in figure **5.30** is located in outcrop B. It has a dip varying between 48° and 53°, and a thickness of the fault core varying from 1 cm to 5 cm. The fault rock is less deformed than that seen in the fault in outcrop A, and several drag folds suggest normal movement. The faults contain lenses of less deformed material **(fig 5.30)**. The fault presented in figure **5.31** is located in the southern part of outcrop C. It has a dip of 60° at the top and bottom of the observable section, and 40° in the middle. In association with the slightly more gentle dip in the middle, a big fault lens can be observed, and in association with the steepening at the bottom, a dramatic thickening of the damage zone is observed.

Faults dipping towards the north are also observed, and two examples from outcrop C have been selected. The first fault, has a dip of 16°-20° towards north, which is close to parallel to the foliation in the surrounding biotite gneiss. This normal fault cuts through a small garnet amphibolite vein, indicating a 16 cm displacement of the hanging-wall towards north **(fig 5.32A)**. The second fault, has a dip of 20° towards north, but is surrounded by heavily folded biotite gneiss **(fig 5.32B)**. The folding in the hanging-wall indicates a thrust movement toward the south, making the structure a fold propagation fault.

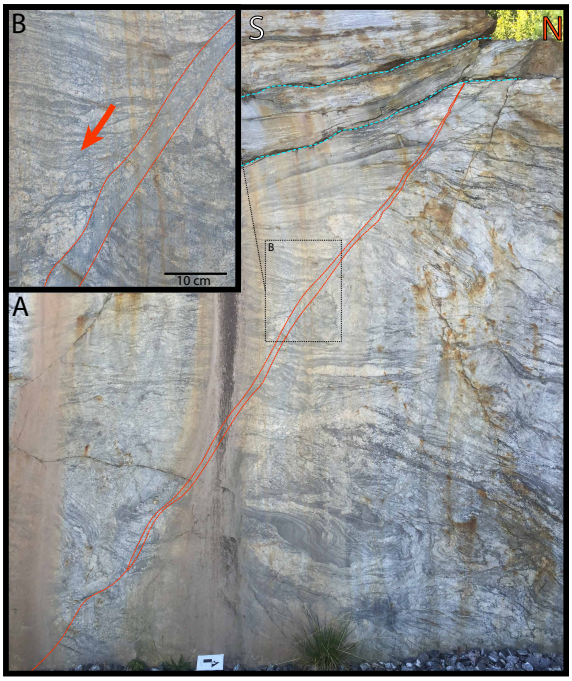

Fig 5.30: Composite figure of fault observed in section B. **A)** The whole fault zone as it is observed in the outcrop. **B)** Close-up section of the fault zone, showing drag folds in the hanging wall, dictating a top towards south movement.

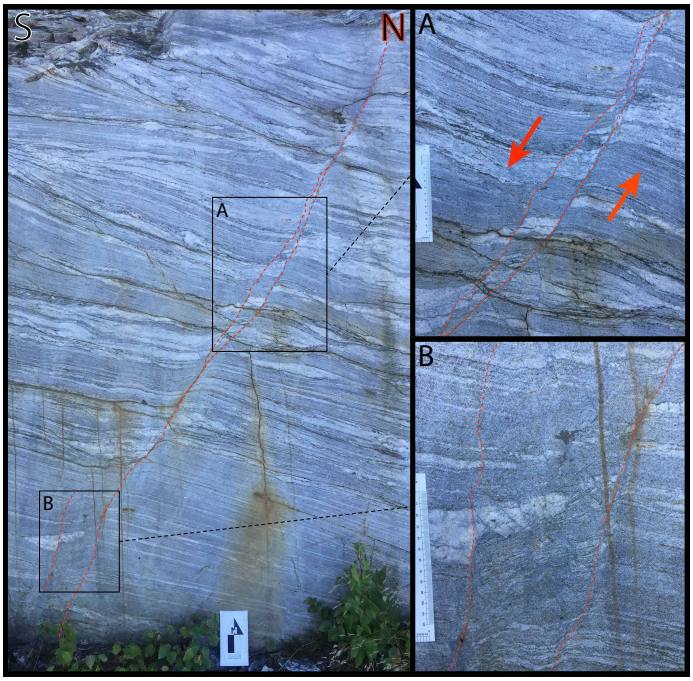

Fig 5.31: Composite figure of the fault observed in the southern part of outcrop C . **A)** Close up section of the large lens in the middle of the observed section. Drag folds in both hanging- and foot-wall indicate normal movement. **B)** Close up section of the dramatic thickening of the damage zone associated with steeping of the fault zone, near the bottom of the section.

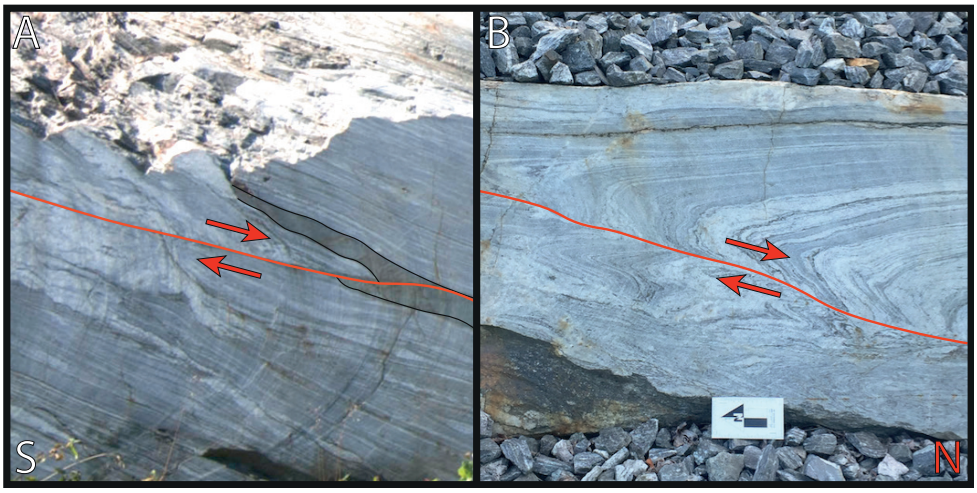

Figure 5.32: Faults seen in southern parts of outcrop C. **A)** Normal fault with top towards north movement, displacing a garnet-amphibolite vein 16 cm. **B)** Normal fault with top toward north movement.

Faults with a uncohesive fault-rock

Faults with a core containing a fault gouge, can be seen in all outcrops. Their fault planes are in general irregular and undulating compared to the planar-faults containing cohesive fault rocks. Two examples will be described, one in outcrop A and one in outcrop C.

In the center of outcrop A, a low-angle normal fault can be seen as it cuts through the lithologies. At one location, the fault displaces the contact between a garnet amphibolite body and the surrounding biotite gneiss **(fig 5.33A)**. The displacement is 30 cm, top-to-the-north,. The dip of the plane in the observed section, oriented north-south, is 20°. The actual dip of the fault is estimated to be steeper, as the dip direction is NW.

In the center of outcrop C, a normal fault is observed, down faulting the entire northern part of the outcrop **(fig 5.33B).** It strikes 206° SW and dips 44°. The fault core is 2-5 cm wide and dominated by a fault gouge. It cuts across several pegmatite veins in both hanging- and foot-wall, yet no information to pinpoint absolute displacement is observed.

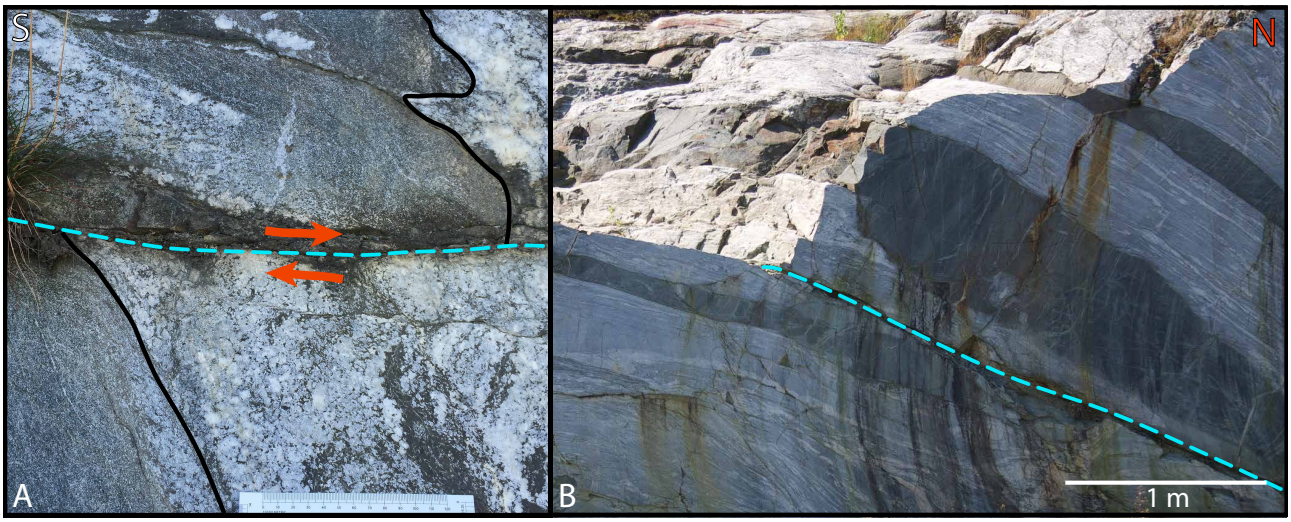

Figure 5.33: Faults containing cores dominated by an uncohesive fault-rock. **(A)** Contact between the garnet-amphibolite and the biotite-gneiss being displaced with 30 cm, top towards the north (normal movement). Picture from outcrop A. **(B)** Fault plane of normal-fault observed in center of outcrop C.

5.3.7 Summary plot

A summary plot of the structural data can be seen in **figure 5.34**. The plot contains poles of the foliation measurements from biotite-gneiss I and II, poles with great circles with displacement vectors for the faults measured and the data from the fold-axes (population FA) measured at the top of outcrop C **(fig 5.25)**. The great circles plotted for the faults containing cohesive fault rocks **(fig: 5.28, 5.30, 5.31 & 5.32A)** appears to form a gently rotated conjugate fault set oriented W-E.

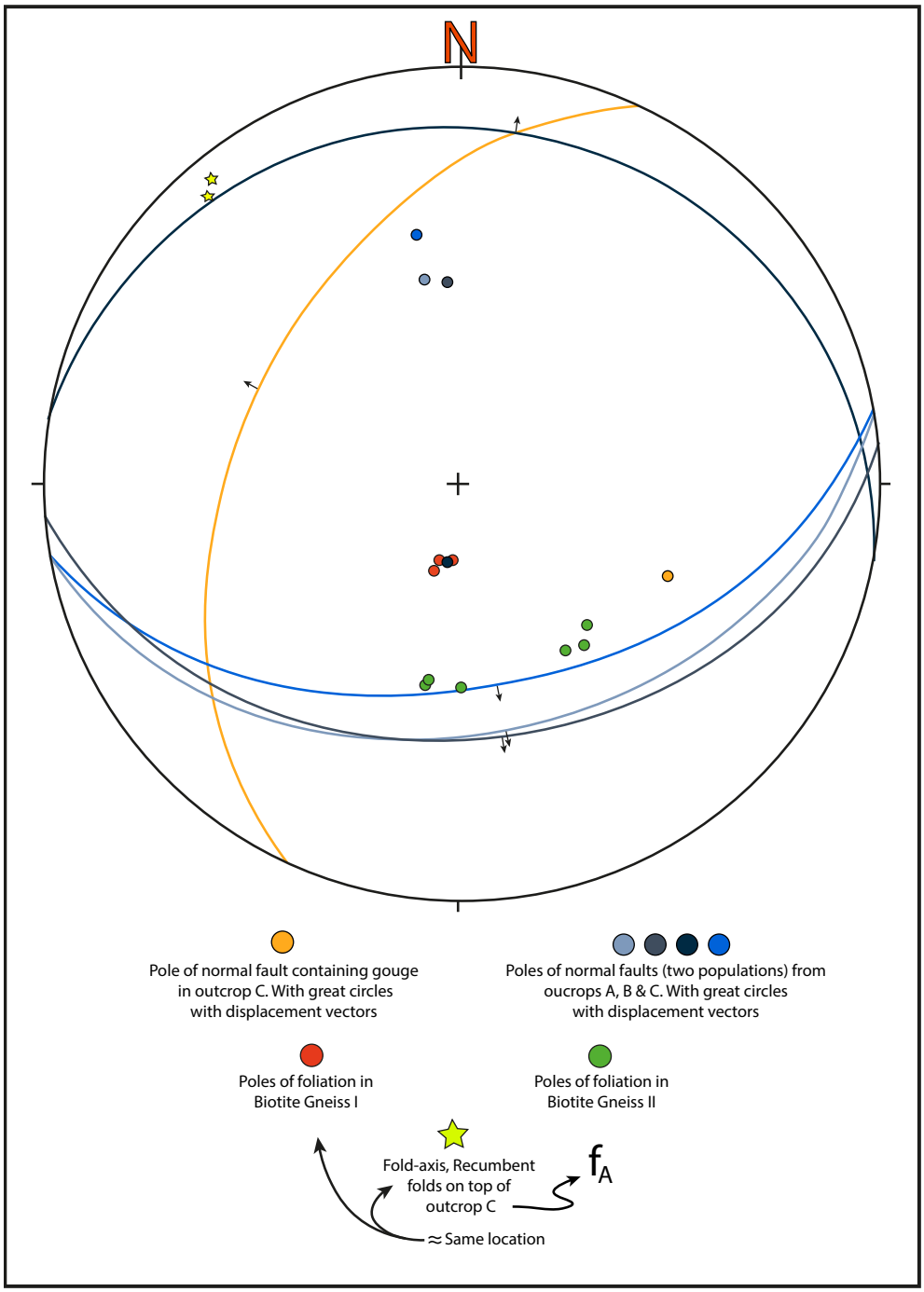

Figure 5.34: Plot of structural data recorded in the outcrops. Including poles of the foliation in the biotite-gneisses, poles and great circles for three fault populations, and the orientations of fold-axes of population FA.

Chapter 6: U/Pb-chronology results

6.1 Introduction

In this chapter the results of the geochronological work will be presented. The process was initiated with rock crushing on 18. December 2015, and the last measurements were completed on 12. October 2016. The samples were analysed using the Isotope Dilution-Thermal Ionization Mass Spectrometry (ID-TIMS) method, and the work was carried out at the laboratory facilities of the Department of Geoscience at the University of Oslo.

In **table 6.1** the complete dataset from the geochronological work is presented, and all values commented in this chapter can be found in this table. The first column shows sample identification followed by a number on the form «**457/s.49**» referring to fractions analyzed, including an «**s.**» if the sample was dissolved in a teflon savillex-vial. Samples were run on the mass spectrometer in three separate series, **457**, **469** and **489**. This was done to get as complete results as possible. Samples that produced insufficient data in the first run could be redone in the second and so on.

The results are presented in concordia plots. These plots contain ellipses representing the age and absolute error for each individual fraction analyzed, of either singular and multiple grains, with labels referring to the calculated fractions of importance to the plot. The ellipses are also color-coded to get an overview of which sample the data point is derived from, or what mineral it represents. A picture overview of all analyzed grains can be seen in **Appendix A**. The pictures in the appendix are helpful since they give a perception of the morphology of each grain, which is important when interpreting the results. The field of view in each picture presented is one square millimeter (mm^2), except for one picture of rutile in the BN15-06 (garnet-amphibolite) sample, where millimeter paper seen in the background can be used as scale.

Interpretations of the results and following discussion can be sees in **chapter 7**.

Fraction Analysed		No. of grains	Abrasion	Weight [ug]	Pbt [ppm]	U [ppm]	Th/U	Pbc [ppm]	Pbcom [pg]	206/204	207/235	2 sigma [abs]	206/238	2 sigma [abs]	rho	207/206	2 sigma [abs]	206/238	2 sigma [abs]	207/235	2 sigma [abs]	207/206	2 sigma [abs]	Disc. [%]
Biotite-gneiss I																								
BN15-02R	457/18	**Zr** 1 gr	CA	1	91	301	0,51	0,00	0,7	8055	3,84	0,01	0,28	0,00	0,89	0,10	0,00	1593,1	3,7	1602,1	2,5	1613,9	2,7	1,5
BN15-02A	457/17	**Zr** 1 gr	CA	1	59	190	0,60	0,00	0,6	5805	3,95	0,02	0,28	0,00	0,97	0,10	0,00	1611,0	8,1	1624,7	4,8	1642,4	2,6	2,2
BN15-02A	457/16	**Zr** 1 gr	CA	1	73	308	0,22	7,57	9,8	440	2,76	0,01	0,21	0,00	0,58	0,09	0,00	1255,0	3,1	1343,6	3,7	1487,6	7,7	17,2
BN15-02	489/S.102	**Mo** 1 gr	NA	1	406	613	5,71	0,00	2,2	4572	3,59	0,01	0,27	0,00	0,89	0,10	0,00	1545,4	2,9	1546,7	2,1	1548,4	2,3	0,2
BN15-02	489/S.103	**Mo** 1 gr	NA	1	903	1285	6,52	0,00	2,6	8150	3,48	0,01	0,27	0,00	0,95	0,10	0,00	1518,9	3,2	1523,6	2,2	1530,1	1,6	0,8
Biotite-gneiss II																								
BN15-10	469/50	**Zr** 1 gr	CA	1	27	92	0,67	0,26	2,3	686	3,56	0,02	0,27	0,00	0,66	0,10	0,00	1519,3	3,8	1540,9	4,8	1570,6	8,8	3,7
BN15-10	469/49	**Zr** 2 gr	CA	1	93	360	0,39	0,00	0,4	12665	3,23	0,01	0,25	0,00	0,87	0,09	0,00	1430,9	3,4	1463,2	2,5	1510,4	3,1	5,9
BN15-10	457/19	**Zr** 1 gr	CA	1	29	147	0,01	0,00	0,7	2669	2,54	0,01	0,21	0,00	0,86	0,09	0,00	1239,4	3,2	1283,8	2,9	1358,9	4,0	9,7
BN15/10	457/20	**Zr** 1 gr	CA	1	40	137	0,73	0,00	0,6	3867	3,45	0,01	0,26	0,00	0,91	0,10	0,00	1498,7	4,7	1515,7	3,3	1539,5	3,3	3,0
Cataclasite from outcrop A																								
BN15-08	469/28	**Zr** 1 gr	AA	1	63	260	0,32	0,00	1,2	3153	3,00	0,01	0,24	0,00	0,90	0,09	0,00	1367,1	3,8	1408,6	2,9	1472,0	3,3	7,9
BN15-08	469/S.82	**Ti** 1 gr	AA	9	17	0,4	11,89	16,00	155	17														
BN15-08	469/S.83	**Ti** 4 gr	AA	5	14	1,2	3,49	13,20	71,9	18														
Garnet amphibolite outcrop C																								
BN15-06	469/30	**Zr** 2 gr	CA	1	36	225	-0,01	0,00	1,4	1720	1,76	0,01	0,17	0,00	0,78	0,07	0,00	1027,3	3,5	1030,6	3,5	1037,6	6,9	1,1
BN15-06	489/26	**Zr** 1 gr	CA	1	12	72	0,02	0,00	0,5	1624	1,80	0,01	0,18	0,00	0,86	0,07	0,00	1040,1	3,0	1044,2	2,7	1053,0	4,3	1,3
BN15-06	489/27	**Zr** 1 gr	CA	1	11	65	0,04	0,00	1,7	436	1,80	0,01	0,17	0,00	0,62	0,08	0,00	1035,0	3,9	1045,9	4,8	1068,6	11,6	3,4
BN15-06	469/54	**Ru** 8 gr	AA	23	2	11	0,00	0,28	8,8	318	1,71	0,02	0,17	0,00	0,61	0,07	0,00	1007,9	5,5	1012,7	6,9	1023,0	17,3	1,6
BN15-06	489/25	**Ru** 7 gr	AA	14	2	12	0,03	0,13	7,6	252	1,76	0,02	0,17	0,00	0,46	0,07	0,00	1018,9	3,4	1030,0	6,0	1053,8	16,5	3,6
BN15-06	489/S.106	**Ti** 5 gr	NA	38	1	1	0,23	1,29	55,1	23	1,43	0,19	0,16	0,00	0,28	0,07	0,01	933,5	11,8	900,8	76,0	821,5	248,5	-14,6
BN15-06	469/S.89	**Ti** 1 gr	NA	3	8	42	0,24	1,16	5,6	237	1,44	0,06	0,15	0,01	0,82	0,07	0,00	928,2	28,3	906,3	24,2	853,2	48,0	-9,4
Garnet amphibolite outcrop A																								
BN15-09	457/S.49	**Ti** 4 gr	AA	28	24	122	0,37	1,82	54,4	705	1,78	0,01	0,17	0,00	0,60	0,07	0,00	1036,2	2,2	1037,1	2,8	1038,9	6,8	0,3
BN15-09	457/S.56	**Ti** 5 gr	AA	27	21	106	0,41	2,38	68,2	476	1,78	0,01	0,17	0,00	0,46	0,07	0,00	1036,7	2,3	1036,8	3,6	1037,1	9,8	0,0
BN15-09	489/28	**Zr** 1 gr	AA	3	141	608	0,29	1,72	11,0	2319	3,04	0,01	0,23	0,00	0,92	0,10	0,00	1315,6	2,8	1418,3	2,4	1576,1	2,5	18,3
BN15-09	489/29	**Zr** 1 gr	AA	13	108	387	0,63	0,00	3,8	20291	3,27	0,03	0,25	0,00	1,00	0,09	0,00	1452,7	13,6	1473,5	8,2	1503,5	1,5	3,8
Pegmatite gen. B																								
BN15-11	489/53	**Zr** 1 gr	AA	1	106	659	0,01	0,00	0,5	14713	1,78	0,01	0,17	0,00	0,87	0,07	0,00	1037,2	2,4	1038,3	2,1	1040,6	3,2	0,4
BN15-11	489/52	**Zr** 1 gr	AA	7	101	631	0,01	0,00	1,1	43198	1,76	0,01	0,17	0,00	0,96	0,07	0,00	1025,1	2,5	1030,0	1,9	1040,3	1,8	1,6
BN15-11	489/51	**Zr** 1 gr	AA	6	100	660	0,01	0,41	8,2	4836	1,65	0,00	0,16	0,00	0,93	0,07	0,00	977,2	2,0	991,1	1,7	1022,2	2,0	4,8
Pegmatite gen. C																								
BN15-07	469/25	**Zr** 1 gr	AA	1	1149	19368	-0,01	92,12	96,9	769	0,49	0,02	0,06	0,00	0,94	0,06	0,00	375,9	11,6	408,0	11,3	594,0	24,1	37,8
BN15-07	469/26	**Zr** 1 gr	AA	1	1038	15131	-0,01	82,67	87,2	774	0,56	0,01	0,07	0,00	0,93	0,06	0,00	434,0	7,8	449,8	7,2	531,3	15,8	18,9
BN15-12	489/S.104	**Mo** 1 gr	NA	8	2283	3320	11,17	0,24	7,7	36954	1,77	0,00	0,17	0,00	0,97	0,07	0,00	1036,6	2,3	1033,5	1,8	1026,8	1,4	-1,0
BN15-12	489/S.105	**Mo** 3 gr	NA	1	6717	8530	13,29	0,00	4,7	19371	1,77	0,00	0,17	0,00	0,96	0,07	0,00	1036,0	2,4	1033,0	1,8	1026,6	1,6	-1,0
BN15-12	489/S.116	**Mo** (*)	AA	12	592	739	13,64	1,05	18,5	5107	1,76	0,01	0,17	0,00	0,95	0,07	0,00	1030,4	2,3	1029,5	1,9	1027,6	2,0	-0,3
BN15-12	489/S.110	**Ti** 3 gr	AA	20	7	42	0,11	0,61	18,0	455	1,48	0,01	0,15	0,00	0,46	0,07	0,00	920,5	2,6	924,1	4,7	932,7	14,1	1,4
Pegmatite vein																								
BN15-3/4/5	469/53	**Zr** 1 gr	AA	1	15	61	0,29	0,00	1,2	784	3,04	0,02	0,23	0,00	0,68	0,09	0,00	1356,4	3,9	1417,2	4,9	1509,8	9,1	11,3
BN15-3/4/5	457/15	**Zr** 1 gr	AA	1	71	294	0,07	0,00	1,3	3695	3,24	0,01	0,25	0,00	0,82	0,09	0,00	1451,3	3,0	1465,8	2,4	1486,8	3,4	2,7
BN15-3/4/5	469/52	**Zr** 1 gr	AA	1	104	775	0,45	0,00	1,3	4734	1,47	0,01	0,13	0,00	0,92	0,08	0,00	770,3	3,2	919,9	3,1	1298,2	4,0	43,1
BN15-3/4/5	457/S.44	**Mo** 2 gr	AA	1	1063	1576	10,82	7,85	10,1	1716	1,77	0,02	0,17	0,00	0,98	0,07	0,00	1033,6	12,5	1033,8	8,7	1034,1	4,8	0,1

Table 6.1: The complete analytical results from the study. Sample identifications are listed to the left, followed by a number on the form «457/s.49» referring to the fraction analyzed. Which mineral and how many grains of the respective mineral is being analyzed is presented in the following column. Three calculated ages are shown for each mineral, 206/238, 207/235 and 207/206. Errors are given as absolute errors at the 2σ level. Error in weight is 1 µg (0.001 mg). Abbreviations: Pbt = total Pb, Pbc = common Pb, Disc = discordancy (in percent), Zr = Zircon, Mo = Monazite, Ru = Rutile, Ti = Titanite, NA= No Abrasion, CA= Chemical Abrasion, AA= Air Abrasion.

6.2.1 Biotite Gneiss I

BN15-02

Three single grains of zircon **(457/16, 457/17 & 457/18)** and two single grains of monazite **(489/s. 102 & 489/s.103)** have been dated from the biotite-gneiss I, sample BN15-02

The zircon population in the sample was split in two fractions, based on morphologically difference. The fraction labeled A, consist of angular or prismatic zircons. The fraction labeled R, consist of sub-rounded to rounded zircon grains. The grains in both fractions are homogenous, transparent and colorless, with no indications of older cores. On the basis of the information above, all zircon grains were chemically abraded. The **457/17** grain and the **457/18** have low common lead (<0.01 ppm), Th/U >0.5 and U-content varying from c.190 - 300 ppm. The apparent ages calculated from the analysis of the **457/17** zircon yields between c.1610-1640 Ma, and c.1590-1615 Ma for the **457/18** grain. The analysis are 2.2% and 1.5% discordant, respectively. The **457/16** grain has a U-content of 308 ppm, and a common lead content of 7.57. The analysis is 17.2% discordant. Two lines have been calculated through the data point, and the results can be seen in **figure 6.1** below.

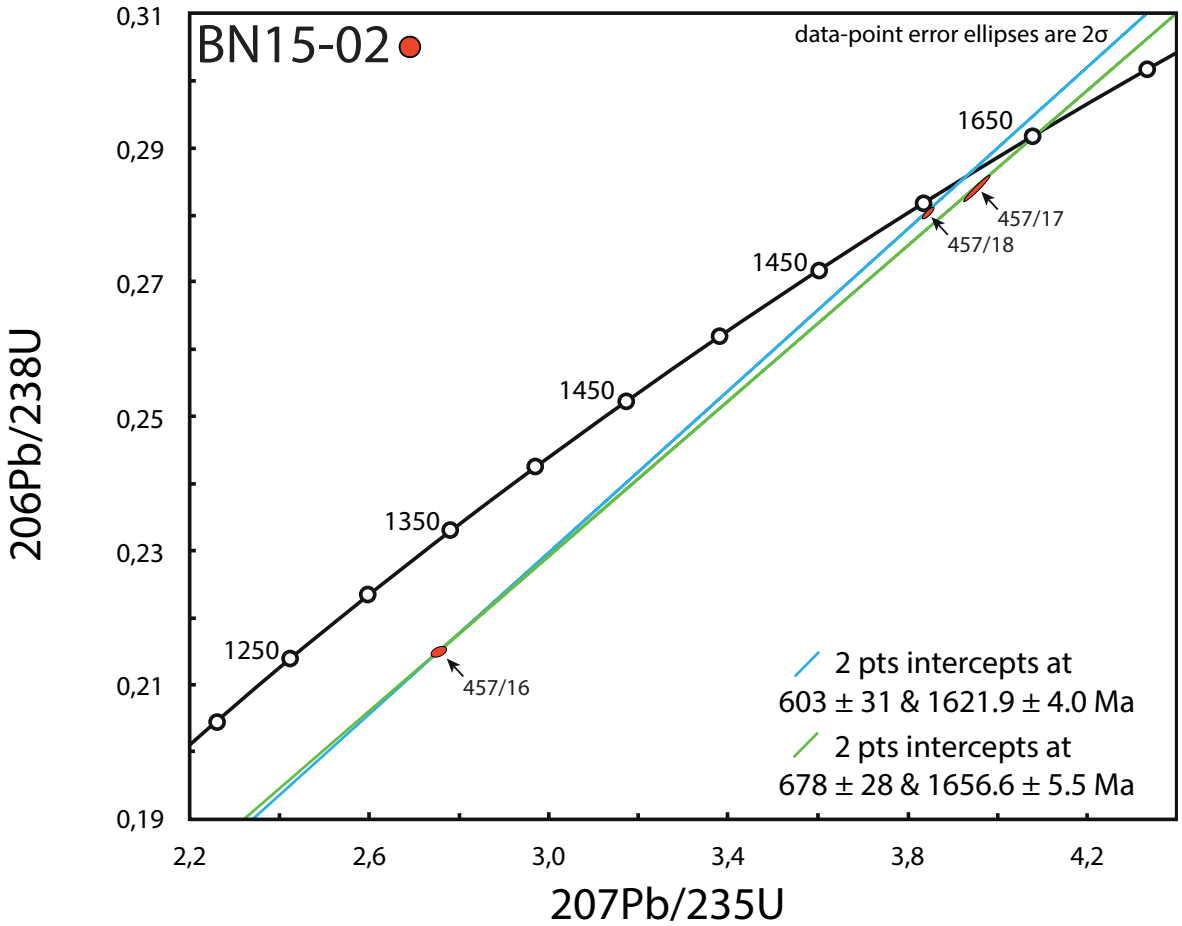

Figure 6.1: Concordia plot of analysis results from the three single grains 457/16, 457/17 and 457/18, found in sample BN15-02, biotite-gneiss I. The blue line represents a calculated line through 457/16 and 457/18, while the green line represents a calculated line through 457/16 and 457/17.

The two single grains of monazite, **489/s.102** and **489/s.103**, are small, transparent and weakly yellow to colorless. The **489/s.102** grain has a U-content of 613 ppm, and Th/U >5.0. The **489/s.103** has more than double the U-content, 1285 ppm, and a Th/U = 6.52. The high Th-content is characteristic for monazite. Both grains have low common lead (<0.01 ppm) and both are close to concordia, with a discordance of 0.2% for the **489/s.102** grain, and 0.8% for the **489/s.103** grain. The two grains have been fitted on a calculated line, intercepting concordia at 1554±11 Ma **(fig 6.2)**.

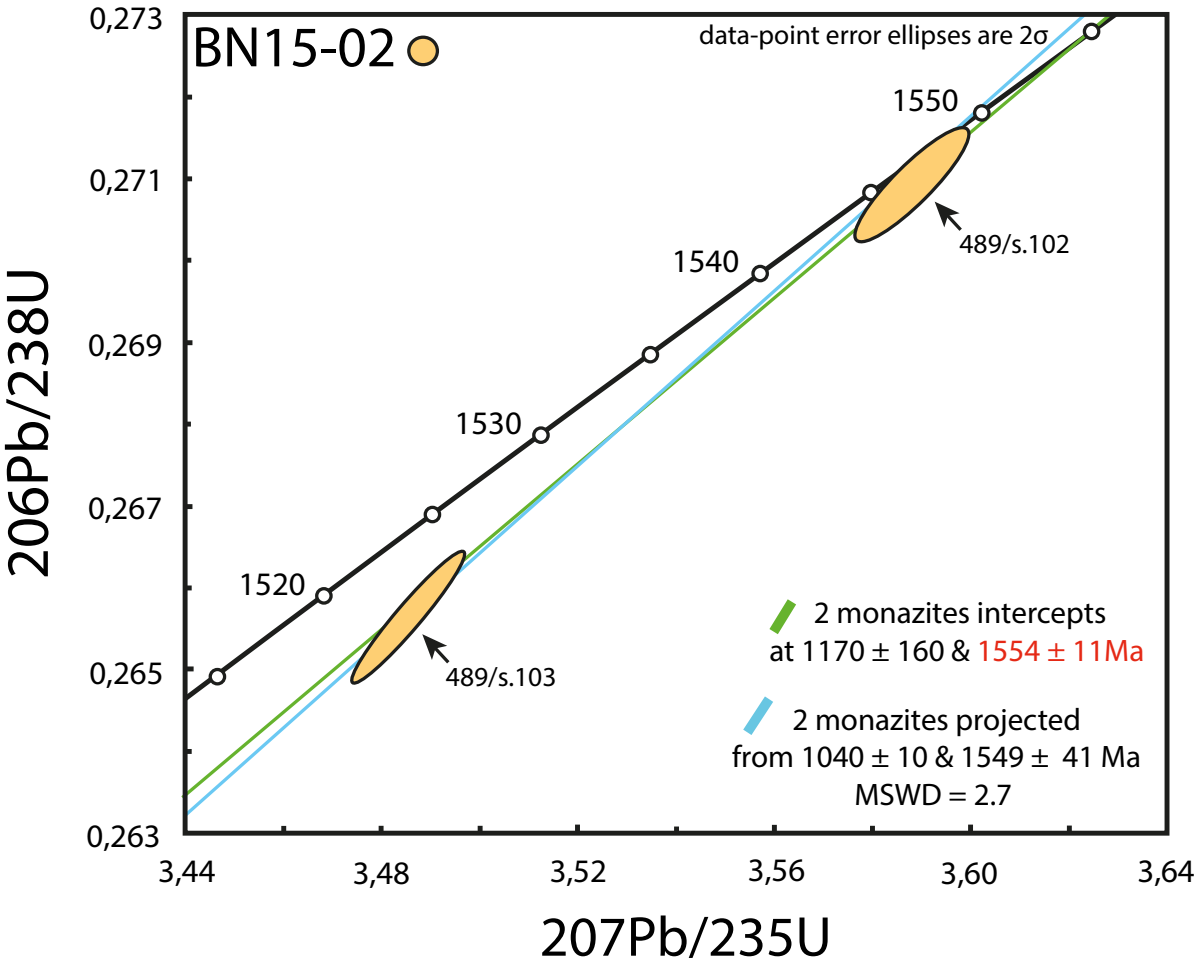

Figure 6.2: Concordia plot of the analysis results from the two single grain monazite fractions, 489/s.102 and 489/s.103, found in sample BN15-02, biotite-gneiss I. The green line represents a calculated line through two points, while the blue line represents a three point calculation where the first is fixed at 1040 ± 10 Ma.

6.2.2 Biotite Gneiss II

BN15-10

Four fractions of zircon have been dated from the biotite-gneiss II, sample BN15-10. Three of the fractions analyzed were single grains (**457/19, 457/20** & **469/50**), and one fraction contained two grains (**469/49**).

The zircon population in the sample was in general sub-rounded, and several grains contained smaller inclusions. The analyzed grains were homogenous, transparent, and weakly yellow or colorless. Based on this information, the grains were chemically abraded. The two fractions from the first analysis series **(457/19 & 457/20)** has low common lead (<0.1 ppm), and a U-content c.140 ppm. The **457/19** grain have low Th (Th/U = 0.01). The analysis is 9.7% discordant. The analysis of the **457/20** grain is 3% discordant. On the basis of these results, a second round of zircons were selected from the already chemically abraded grains, and were analyzed **(469/49 and 469/50)**. The **469/49** fraction has a U-content of 360 ppm, and a low Th-content. The **469/50** zircon has a low U-content of 92 ppm, and is slightly higher in Th compared to the **469/49.** It also has more common lead than the other grains analyzed, with 0.26 ppm. The analysis of the **469/49** fraction is 5.9% discordant. The analysis of the **469/50** zircon is 3.7% discordant.

In **figure 6.3** a concordia plot containing the analyses for zircon can be seen (blue), accompanied by the zircon analyses from biotite-gneiss I (BN15-02, red). One line has been fitted through **469/49**, **469/50** and **457/15** (from BN15-02). The line intercepts concordia at 1638.3 ± 5.5 Ma, the lower intercession is fixed. The MSWD is very low but several outliers were not considered.

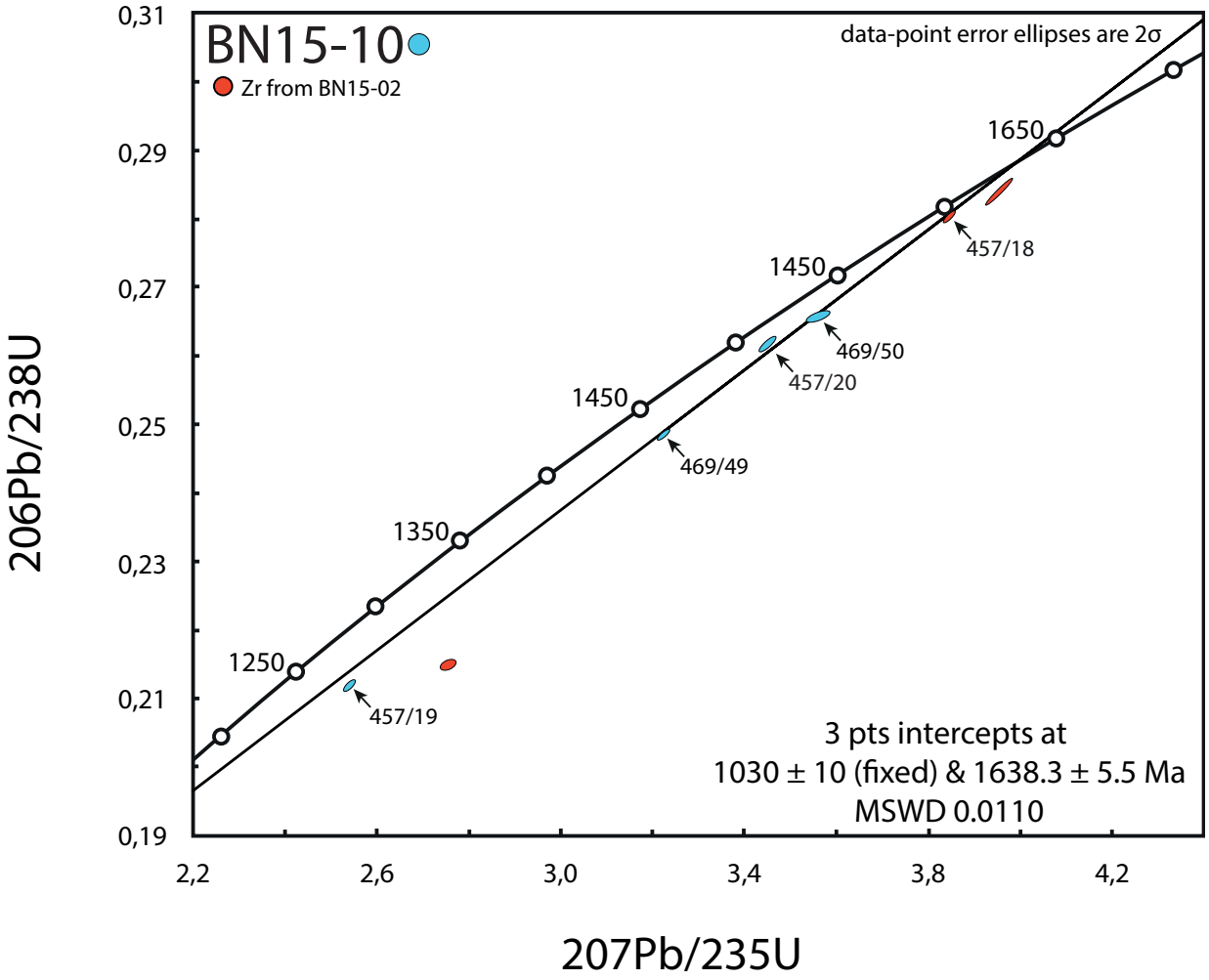

Figure 6.3: Concordia plot of the analysis results from the zircon fractions 457/19, 457/20, 469/49 and 469/50, from sample BN15-10, biotite-gneiss II (blue). Accompanied by three zircon analyses from BN15-02, biotite I (red).

6.2.3 Garnet-amphibolite

BN15-09

Two fractions of zircon **(489/28 & 489/29)** and two fractions of titanite **(457/s.49 & 457/s.56)** have been analyzed from the garnet amphibolite in outcrop A, sample BN15-09. Both zircon fractions consist of single grains, while the titanite fractions **457/s.49** and **457/s.56** consist of four and five grains, respectively.

The zircons analyzed were metamict, with gray to dark gray color, and no transparency. Due to their high degree of metamictization they were air-abraded, as they would likely dissolve during chemical abrasion. The grains vary in U-content from 387 ppm in **489/29** to 608 ppm in the **489/28**, but has a similar Th-content (0.3-0.6). The **489/28** grain is relatively high in common lead (1.72 ppm) compared to the **489/29** grain (<0.01 ppm). The **489/28** grain is 18.3% discordant, and the **489/29** grain is 3.8% discordance. The analysis of the **489/28** grain gives apparent ages of c. 1315 - 1580 Ma, while the analysis of the **489/29** grain gives ages c. 1450-1500 Ma. The analyses are plotted in **figure 6.4**, together with zircon data from the surrounding biotite gneiss, sample BN15-10 (biotite-gneiss II) in blue color.

The titanites analyzed were quite big, rounded, transparent, homogenous and with a weak yellow tint. The fractions vary in U-content from 106 to 122 ppm, and both contain between 1.8 and 2.3 ppm common lead. Both fractions are concordant, with less than 0.3% discordance. Fraction **457/s.49** yields ages c. 1036 - 1038 Ma, while fraction **457/s.56** yields ages c. 1036 - 1037 Ma. **Figure 6.4** show how the analysis plot on the concordia curve, with a MSWD = 0.22.

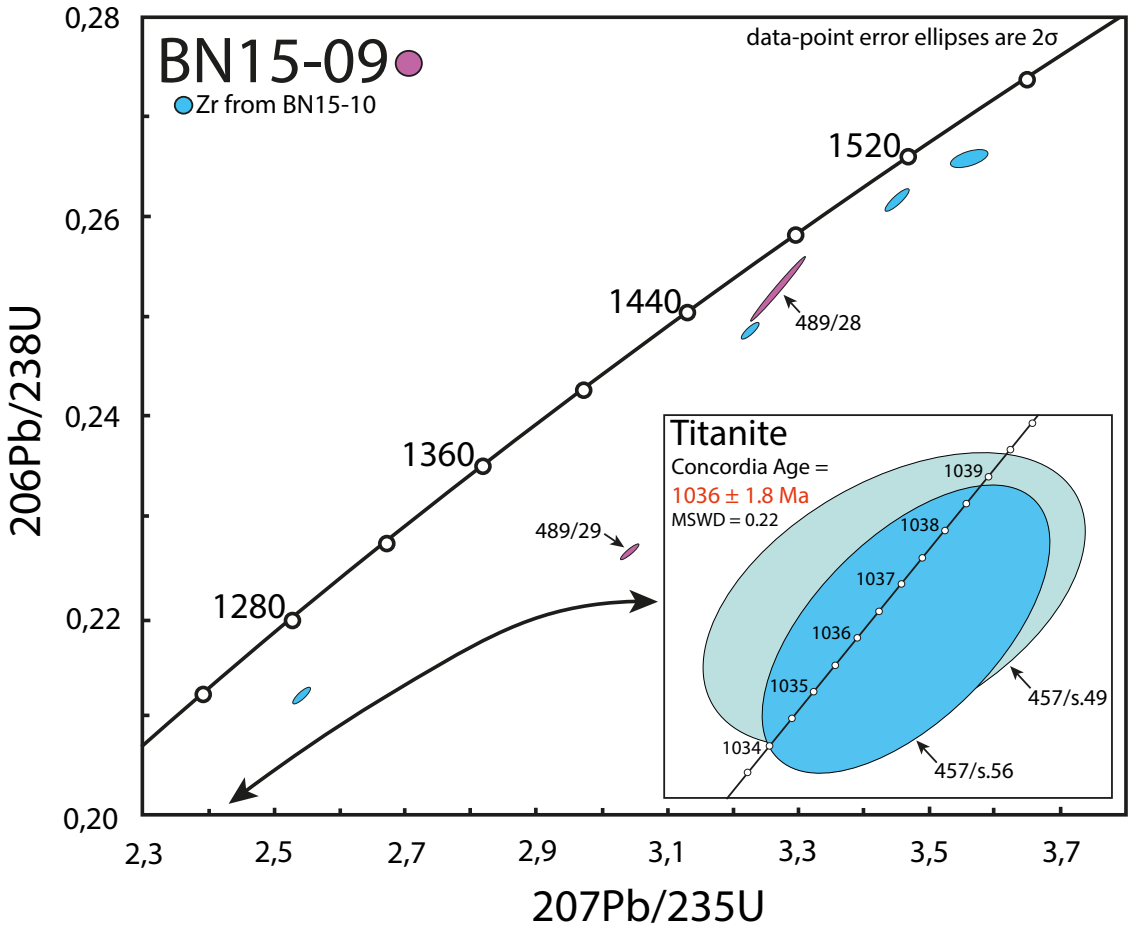

Fig 6.4 (previous page): Two concordia plot of the analysis results from sample BN15-09, garnet amphibolite. **(Big)** Concordia plot of the zircon fractions 489/28 and 489/29 from BN15-09(pink), accompanied by data points from the zircons in sample BN15-10 (biotite gneiss II). **(Small)** Concordia plot of the analysis results from the two titanite fractions 457/s.49 and 457/s.56 from BN15-09.

6.2.4 Cataclasite

BN15-08

One single grain analysis of zircon **(469/28)**, and two fractions of titanite **(469/s.82 & 469/s.83)** has been dated from the ultracataclasite fault rock in the southern part of outcrop A. The zircon grain has a U-content of 260 ppm, and <0.01 ppm common lead. The grain is 7.9% discordant and yields ages between c. 1370-1470 Ma. The titanite fractions has U-contents <1.3 ppm, and common lead content >13 ppm. Because of that, no meaningful ages can be calculated for this titanite. The result from the zircon analysis can be seen in the plot below, **figure 6.5**.

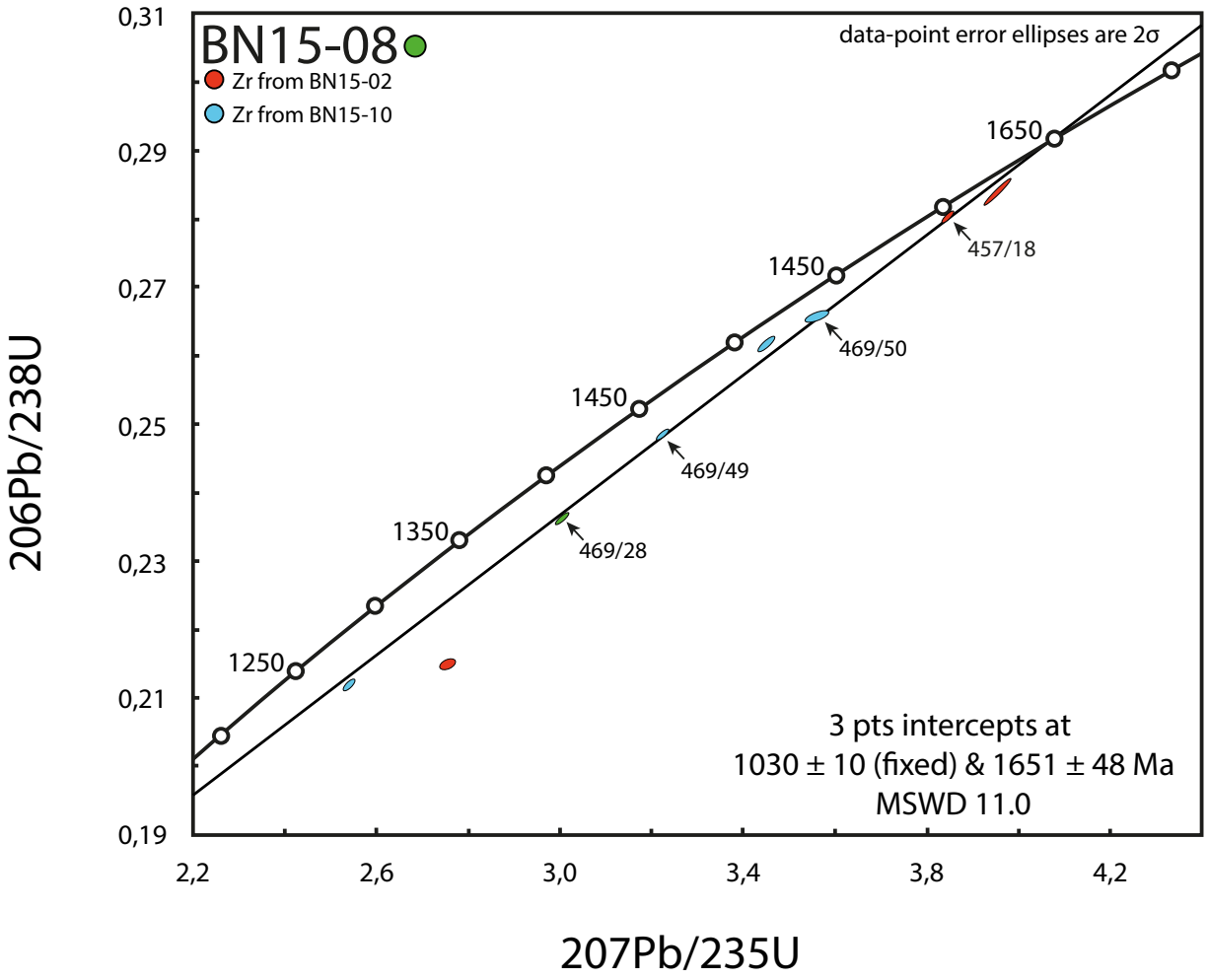

Figure 6.5: Concordia plot of the analysis result from zircon 469/28 (green) from sample BN15-08, accompanied by analysis results from BN15-02 (biotite-gneiss I, red) and BN15-10 (biotite-gneiss II,blue). A line has been calculated through the labeled ellipses, with fixed lower interception at 1030 ± 10 Ma, and a upper interception at 1651 ± 48 Ma. MSWD = 11.0

6.2.5 Garnet-amphibolite

BN15-06

Three fractions of zircon **(469/30, 489/26 & 489/27)**, two fractions of rutile **(469/54 & 489/25)**, and two fractions of titanite **(469/s.89 & 489/s.106)** have been analyzed from the garnet amphibolite in outcrop C (BN15-06).

The zircon population in the sample in general consists of small, colorless, homogenous and sub-rounded grains. Two single grain analyses were performed **(489/26 & 489/27)** and one fraction of two grains **(469/30)**. The U-content varies from 65 to 225 ppm, low Th content (Th/U <0.05) and low content of common lead (<0.01 ppm). The three fractions analyzed plots under the concordia curve, with a discordance of 1.1-1.3% for the **469/30** and **489/26** fractions, and 3.4% for the **489/27** fraction, yielding ages between c. 1030-1040 Ma, and c. 1040-1070 Ma for the slightly more discordant **489/27** fraction.

The rutiles were analyzed in fractions of 7 and 8 grains **(469/54 & 489/25,** respectively**)**. The grains displayed variance in appearance, from rounded to elongated prismatic, with a deep brownish to red color, transparent and small dark spots of impurities or inclusions. The rutiles display a low U-content, with c.12 ppm. They have a slightly higher content of common lead than the zircon fractions analyzed, with 0.13-0.28 ppm. The **469/54** fraction is 1.6% discordant, and yields ages slightly younger than the zircons, between c.1005-1025 Ma. The **489/25** fraction is 3.6% discordant, and yields ages between 1020-1050 Ma.

The titanites were analyzed in two fractions, where one was a single grain **(469/s.89)** and the other consisted of five grains **(489/s.106)**. The titanites in both fractions were colorless, transparent and without inclusions. The **489/s.106** fraction has 1 ppm U-content, c. 1.3 ppm common lead. The **469/s. 89** fraction has 42 ppm U-content, and c. 1.2 ppm common lead, and is slightly reverse discordant. Both fractions yields ages around c.920 with large absolute errors for the 207/235- and 207/206-ages.

In **figure 6.6** two concordia plots of the results from the garnet-amphibolite sample BN15-06 can be seen, with data from sample BN15-09 (garnet-amphibolite) and BN15-12 (pegmatite gen.B) as well.

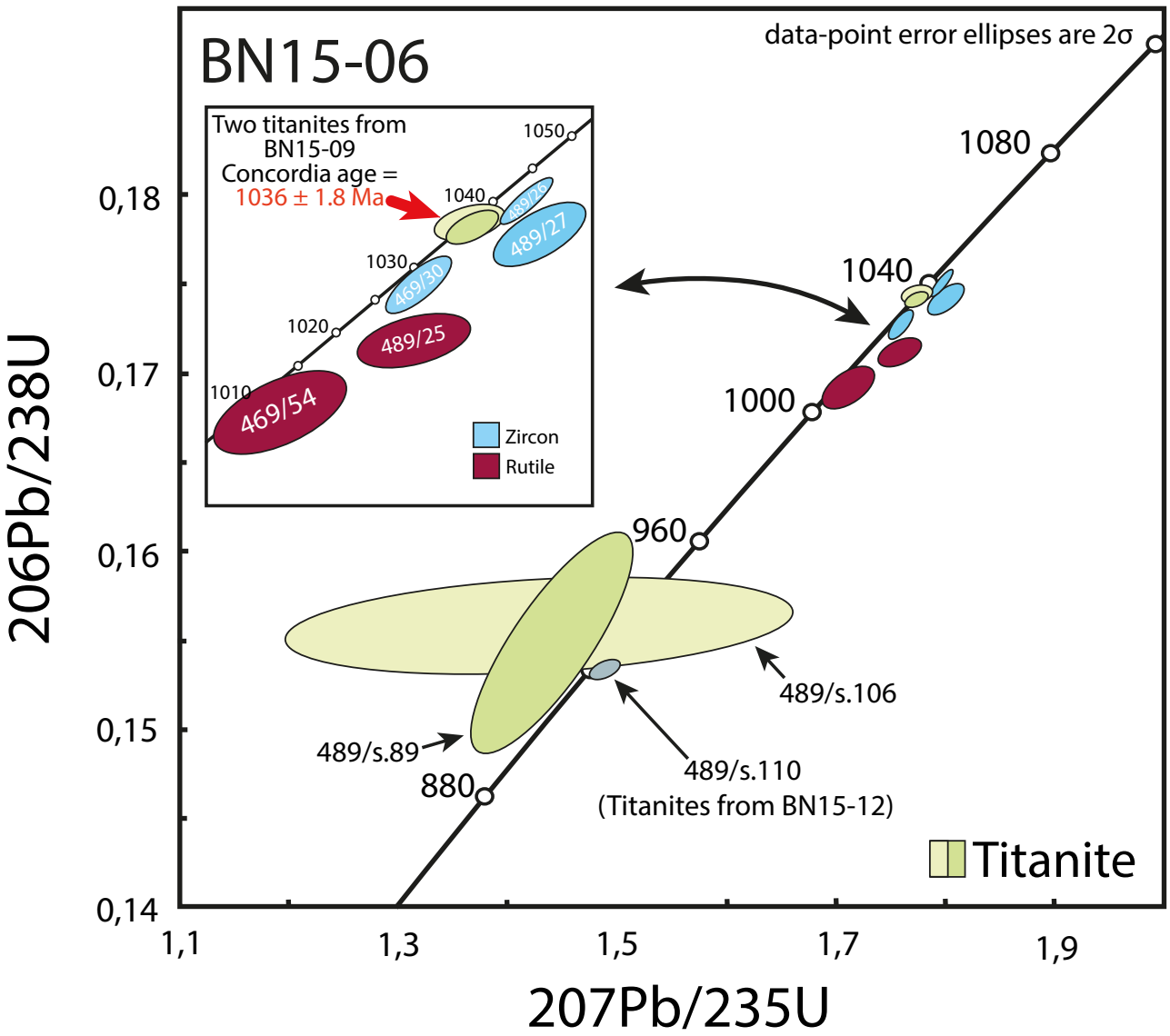

Figure 6.6: Concordia plots of analysis results from the garnet amphibolite sample from outcrop C, sample BN15-06. Accompanied by titanites from both BN15-09 (garnet-amphibolite) and BN15-12 (pegmatite gen. B).

6.2.6 Pegmatite gen. B

BN15-11

Three single grain analyses of zircon **(489/51, 489/52 & 489/53)** were produced from the generation B pegmatite, sample BN15-11 from outcrop C. The **489/51** and **489/52** zircons are gray to colorless, non transparent, sub-rounded and quite big. Due to their metamictization they were air-abraded. The **489/53** zircon was smaller than the other grains, transparent and colorless. The fractions have similar U-content, ranging from 631-660 ppm, and Th/U = 0.01 for all samples. All fractions contain low common lead (<0.01 ppm), except fraction **489/51** that contains 0.41 ppm common lead. Fraction **489/51** is the most discordant, with 4.8%. Fraction **489/52** is 1.6% discordant, and fraction **482/53** is 0.4% discordant. Shown in **figure 6.7**, two calculated lines are seen. The lowermost is calculated through the **489/52** and **489/53** projecting the age 1040.7 ± 4.2 Ma in the upper interception.

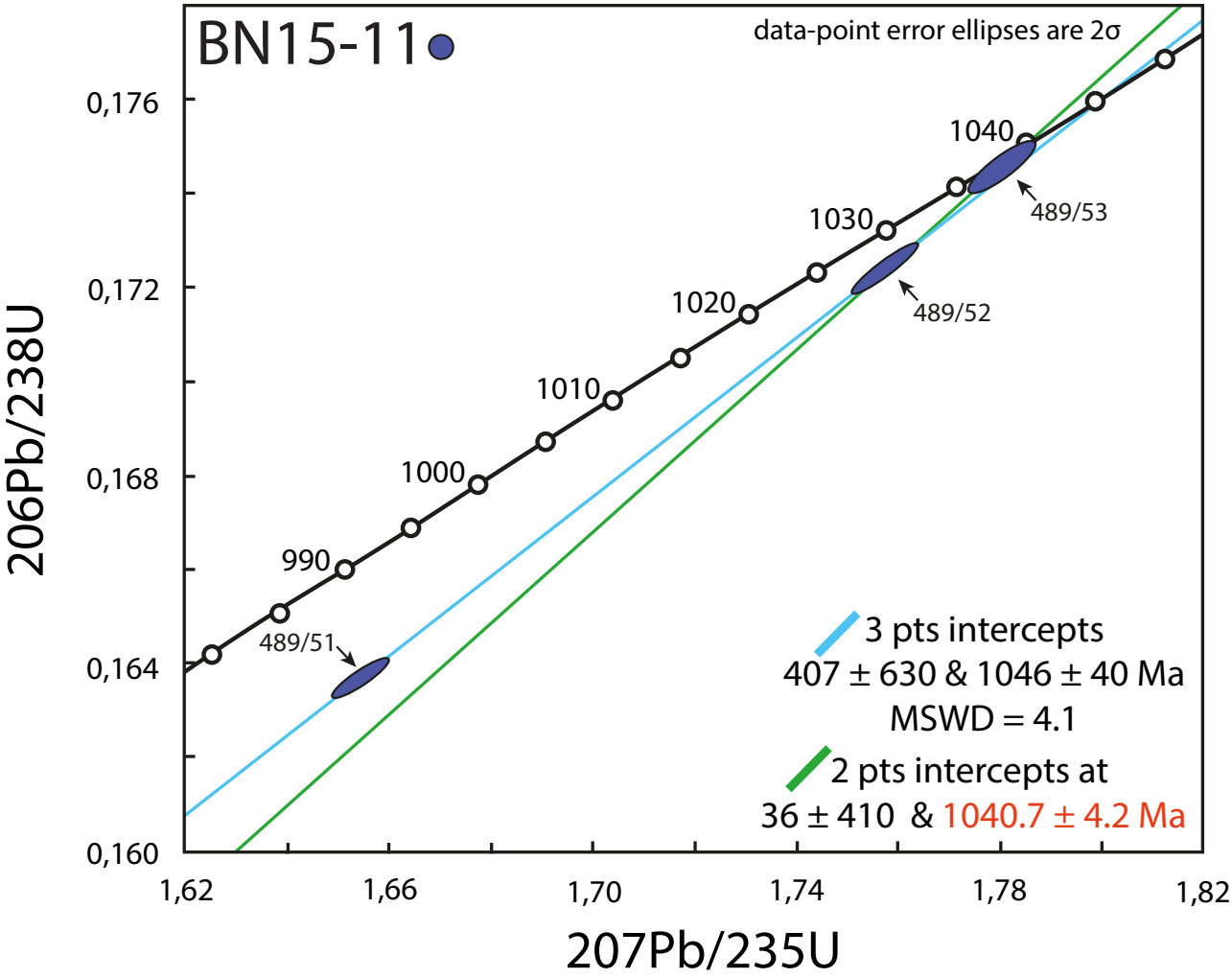

Figure 6.7: Concordia plot of the results from the analyzed zircon grains in the generation B pegmatite from outcrop C, sample BN15-11. With two calculated lines, with 3 and 2 data points.

6.2.7 Pegmatite gen. C

BN15-07 & BN15-12

Two single grains of zircon (**469/25** & **469/26**) were analyzed from the pegmatite vein referred to as generation C, sample BN15-07 in outcrop C. Both grains were highly metamict, with reduced transparency and turbidity. The **469/26** grain was grey and angular, while the **469/25** grain was dark gray to brown, with dark inclusions and sub-rounded crystal shape. The analyzed U-contents of both samples are very high (>15000 ppm), and common lead content above 80 ppm. The **469/25** grain is 37.8% discordant, and the **469/26** grain is 18.9% discordant, so that the data are inconclusive and cannot reliably be extrapolated to the primary age. Because of these results a new sample, BN15-12, was collected from the same pegmatite vein in outcrop C.

Three fractions of monazite (**489/s.104**, **489/s.105** & **489/s.116**) and one fraction of titanite (**489/s.110**) were analyzed from this second sample, BN15-12. The monazite grains in the **489/s.104** and **489/s.105** fractions, were in general transparent with a yellow tint, with a variance in size from 0.05-0.3 mm. The analysis of the single grain of monazite **489/s.104**, and the three grains of monazite in fraction **489/s.105**, gives almost identical results. Both have very high U-content, 3320 ppm and 8530 ppm

respectively. They also have high Th/U ratios of 11.17 for the **489/s.104** grain and 13.29 for the **489/s.105** fraction, and low common lead (<0.25 for both). The calculated age for both analyses are between c. 1026-1036 Ma, with reverse discordance of 1% for both. The calculated mean $^{207}Pb/^{235}U$ age is 1033.2 ± 1.2 Ma, see **figure 6.8.** This age is chosen because the $^{206}/_{238}$ age is likely affected by the initial ^{230}Th disequilibrium.

Other grains present in the sample had the appearance of clear titanite. The analysis of a fraction of 3 grains (**489/s.116**), however, yielded a high U-content of 739 ppm, and a calculated Th/U = 13.64, strongly suggesting that at least one of the grains was monazite. The position of this data point below that of the two first monazite analysis suggest that they represent a mixture with titanite **(fig 6.8)**.

The analysis of the titanite fraction **489/s.110**, shows a U-content of 42 ppm, common lead of 0.61 and a discordance of 1.4%. The 206/238 age of this fraction is 920.5 ± 2.6 Ma, similar to that of the titanite in sample BN15-06 **(fig 6.4)**.

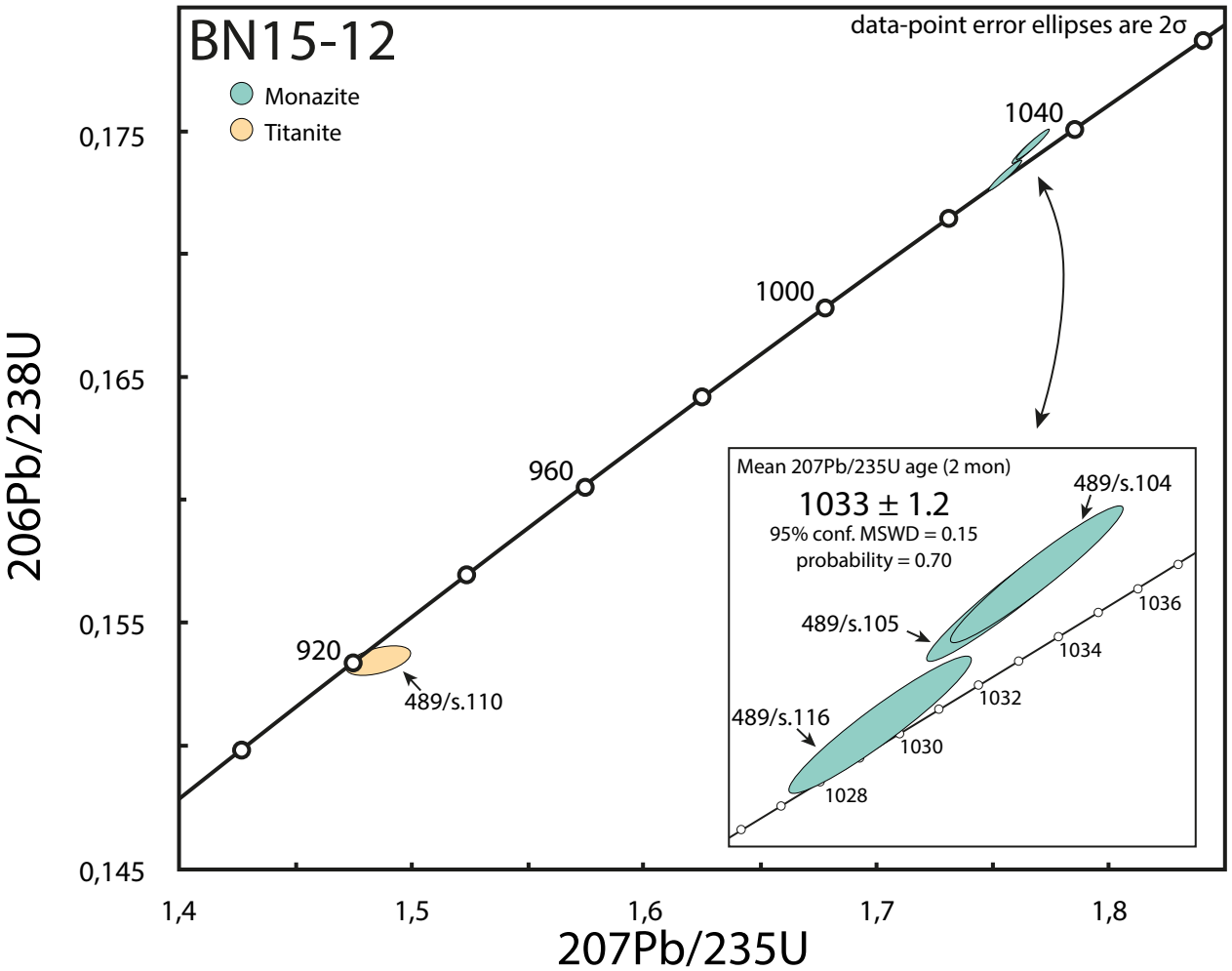

Figure 6.8: Concordia plot of the analysis results from monazite fractions 489/s.104, 489/s.105, 489/s.116, and titanite fraction 489/s.110 from pegmatite sample BN15-12, referred to as pegmatite generation C. A calculated mean 207Pb/235U age of 1033.2 ± 1.2 Ma can be seen in the bottom right corner.

6.2.8 Pegmatite vein

Outcrop C: BN15-3/4/5

Three single grains of zircon **(457/15, 469/52 & 469/53)** and one fraction of monazite **(457/s.44)** were analyzed from a small vein of pegmatite in outcrop C, sample BN15-3/4/5. The zircon fractions were all single grains, while the monazite fraction consisted of two grains.

The two single grains of zircon analyzed, **457/15** and **469/53,** were small, transparent, sub-rounded, colorless and seemingly homogeneous. Many of these characteristics count for the **469/52** grain as well, but it is slightly bigger and has a matt gray hue. The three grains range in U-content from 61-775 ppm, where the **469/52** zircon has the highest U-content. All fractions are low in common lead (>0.01 ppm). The analysis of the **457/15** grain is 2.7% discordant and gives ages c.1450-1490 Ma, while the analysis of the **469/52** grain and the **469/53** grain are 43.1% and 11.3% discordant, respectively. This results in calculations variating between c. 770-1300 Ma for the **469/52** grain, and 1350-1510 Ma for the **469/53** grain. The results from the analyses of the zircons **457/15** and **469/53** can be seen in **figure 6.9**. The figure display all zircon analysis older than 1200 Ma.
The monazite fraction analyzed, **457/s.44**, consisted of two rounded, colorless and transparent grains. Bigger than the zircons analyzed, but still weighing less than 1 microgram. The fraction has a high U-content of 1576 ppm, and a common lead content of 7.85 ppm. The analysis is concordant and gives a concordia age of 1034±6.0 Ma. In the inset-figure below, in **figure 6.9**, this is plotted together with the three monazites from the BN15-12 sample, pegmatite generation C.

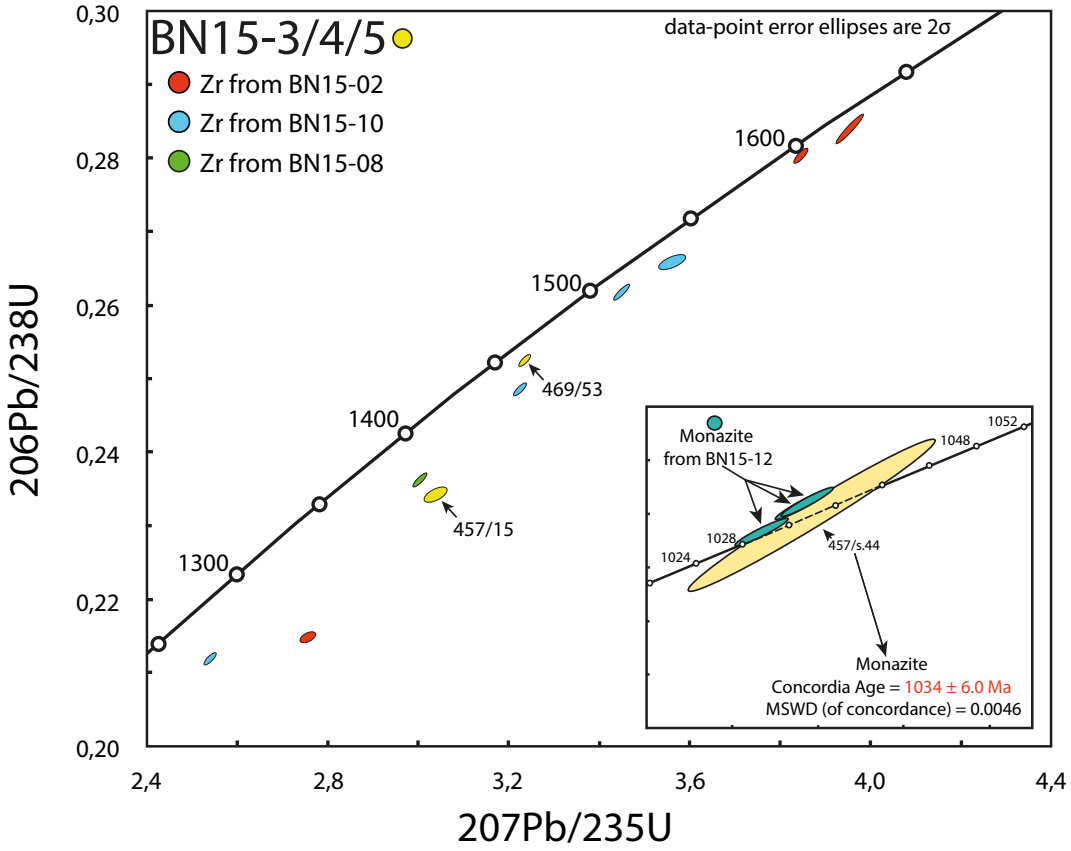

Figure 6.9: Concordia plots of the analysis result from the BN15-3/4/5 small pegmatite vein in outcrop C. **(Big)** Zircon fractions 457/15 and 469/53 (yellow) plotted together with zircons from BN15-02 (biotite-gneiss I, red), BN15-10 (biotite-gneiss II, blue) and BN15-08 (ultracataclasite, green). **(Small)** Monazite fraction 457/s.44 plotted together with three monazite calculations from sample BN15-12 (Pegmatite gen. C). The 457/s.44 fraction yields a concordia age = 1034 ± 6.0 Ma, MSWD = 0.0046.

Chapter 7: Discussion

7.1 Introduction

In the following, aspects from the lithological descriptions, structural observations and U/Pb-chronology results will be elaborated and set into a regional context. Firstly, the age and formation of the biotite-gneisses, garnet-amphibolites and the pegmatite generations will be discussed, followed by a presentation of the main metamorphic events as documented in the study. Interpretative remarks regarding the structural features observed in the outcrops will also be given, before an attempt to summarize the thermo-tectonic evolution (time-pressure/temperature-strain history) is made.

7.2 The age and formation of the lithologies

7.2.1 Introduction

From the U/Pb-chronology results presented in **chapter 6**, a short summary is sufficient before further discussion. The grains yield ages corresponding to main "events". These are the old, c. 1500-1650 Ma zircon analyses, the 1550 Ma monazites, the clustering of results around the intermediate event at c.1030-1040 Ma, and a younger event recorded by titanites around 920 Ma. We thus see four points in time of importance.

All analyzed grains older than the intermediate c. 1030-1040Ma event, share a common trend of discordance **(figure 7.1)**. This trend is interpreted to result from secondary lead loss induced by a major metamorphic event.

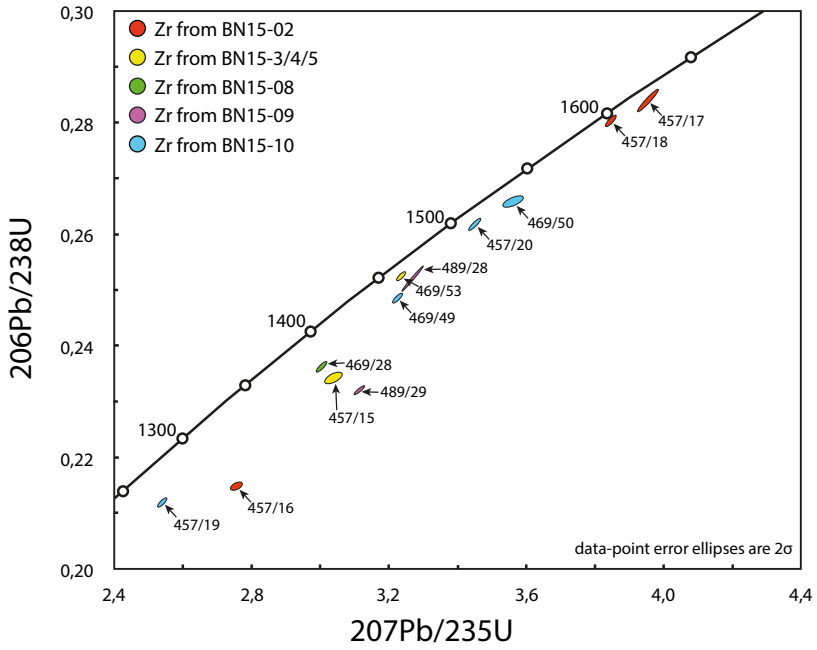

Figure 7.1: Plot of all analyzed zircon grains older than 1200Ma. Results collected from BN15-02 (biotite-gneiss I), BN15-3/4/5 (small pegmatite vein, outcrop C), BN15-08 (Ultracataclasite), BN15-09 (garnet-amphibolite outcrop A) and BN15-10 (biotite-gneiss II).

7.2.2 The biotite-gneisses

The origin of the biotite-gneiss is a central question in the discussion, and a vital question for the interpretation of the U-Pb data. According to the previous works **(i.e Skjernaa & Pedersen 1982, Åhäll and Connelly 2008)**, gneisses of both plutonic- and sedimentary-origin, orthogneiss and paragneiss, respectively, are found in the SLM-formation, or Østfold Complex to be more precise. To this point all statements concerning the origin of the gneiss have been avoided intentionally. In the lithological description of the biotite-gneiss **(chapter 5.2)**, the bulk rock composition (40% quartz, 20% alkali feldspar, 20% plagioclase) documents a granitic composition, but no distinct observations were made to determine the genesis.

The gray biotite-gneiss shows considerable textural and minor mineralogical variation, and on this basis samples were taken separately, and later named biotite-gneiss I (sample BN15-02) and biotite-gneiss II (sample BN15-10), where the biotite-gneiss II seemingly has a large component of deformation. A contact between the two biotite-gneisses was observed in outcrop B **(fig 5.8).** The contact is gradual rather than a sharp discontinuity. There are two possibilities, either the gneisses are different lithological units, or the observed differences are controlled by variations in deformation and metamorphism. From the U-Pb results **(table 6.1)** the zircon grains of biotite-gneiss I yield slightly older apparent ages than in biotite-gneiss II, but this might just be explained by increased lead loss as an effect of a higher grade of metamorphism. In **figure 7.2**, the results of the zircon analyses from both biotite-gneisses can be seen. A line has been fitted through three points belonging to both biotite-gneiss I and biotite-gneiss II, with a fixed lower intersection of concordia of 1030 ± 10 Ma and a upper intersection of concordia at 1638.3 ± 5.5 Ma. The other analyses deviate somewhat from the line, but not greatly, and thus there is no isotopic evidence that the biotite-gneiss I is significantly older than biotite-gneiss II. In further discussion the biotite-gneisses will therefore be treated as if the two have the same origin.

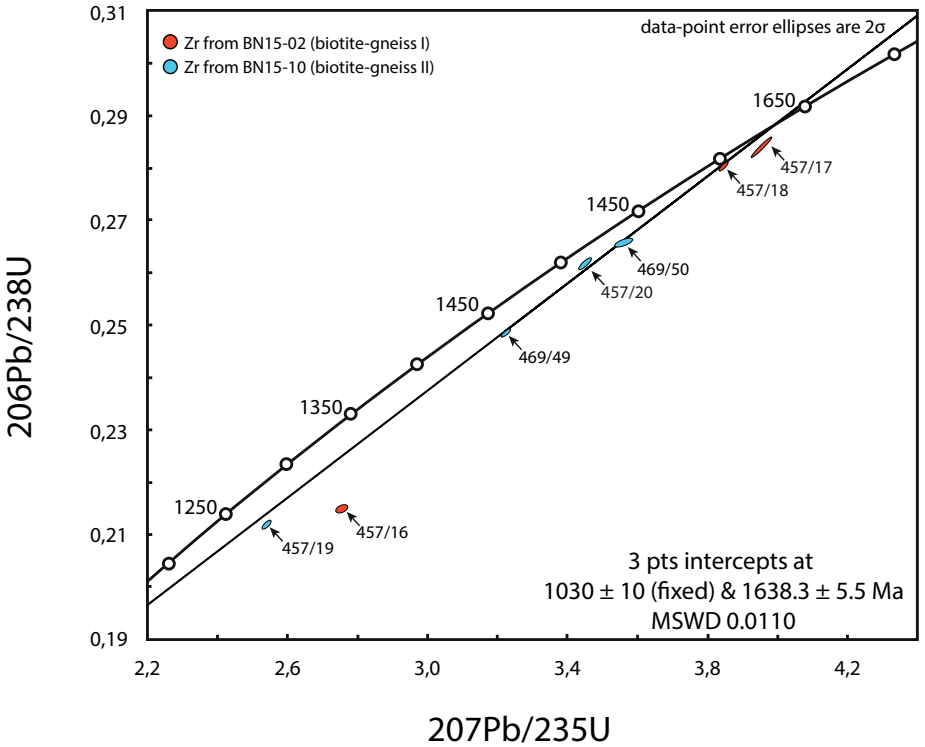

Figure 7.2: Results from zircon grains analyses in biotite-gneiss I and biotite-gneiss II plotted with an calculated line trough three points.

If the biotite-gneisses have an plutonic origin (orthogneiss), we could expect to see a well defined crystallization age if the grains analyzed were coherent, meaning that the geochronological data would point toward a single event in the concordia plot. If the biotite-gneisses have a sedimentary origin (paragneiss), we could expect to see a detrital zircon suite with a large range of ages, representing multiple protoliths, deposited in the same location.

The analytical results from the zircons in the biotite-gneiss I **(table 6.1)**, sample BN15-02, suggests different ages of 1622 and 1657 Ma. Analysis 457/17 plots below the regression line anchored at 1030 Ma **(fig 7.2)**, suggesting that the difference is not due to Pb loss, but to an older zircon component. This could be an inherited core in an intrusive rock, or a detrital grain. Sample BN15-10 also shows scatter in the zircon data, but in this case it could be due either to complex Pb loss or an heterogenous population.

Looking at the zircon grains themselves, and their characteristics, valuable information can be derived. By sorting the grains on the basis of how they look, two groups were distinguished in the BN15-02 sample (biotite-gneiss I), with significant differences. In **figure 7.3** (next page), these two groups can be seen. The BN15-02 (A) group contain prismatic, elongated and euhedral crystals, while the BN15-02 (R) group contain larger and more rounded (anhedral) crystals. If the gneiss is an paragneiss, the differences in the shapes of the grains are interpreted to reflect differences in the length of transportation for the sediment, and maybe more importantly, short transportation for the euhedral BN15-02 (A) zircons.

The analysis of two monazite grains from biotite-gneiss I, **489s.102** and **489/s.103**, become valuable in the pursuit of an origin for the biotite-gneisses. The two grains have been fitted on a calculated line, intercepting concordia at 1554 ± 11 Ma, which likely represents a metamorphic event (gneissification). This would mean that the formation of biotite-gneisses happened on the boarder between the SLM-2 and SLM-1 units, at a late stage in the Gothian orogeny (c. 1715 -1550 Ma; **Graversen and Pedersen (1999)**) in a period characterized by island arc volcanism in the northwest parts of the SLM **(Åhäll and Connelly 2008)**.

According to **Cawood (2012)** differences in age for detrital zircons reflect the tectonic setting of the basin in which they were deposited. Convergent plate margins are characterized by many zircon ages close to the depositional age, whereas sediments at passive plate margins of lower igneous flux are characterized by a large portion of zircon with older ages reflecting the history of the basement.

Based on these arguments, the biotite-gneisses are interpreted as paragneisses with a detrital zircon suite derived directly from the contemporaneous island arc yielding ages between c.1600-1660 Ma. The gneisses underwent metamorphism which produced monazite at 1554 ± 11 Ma.

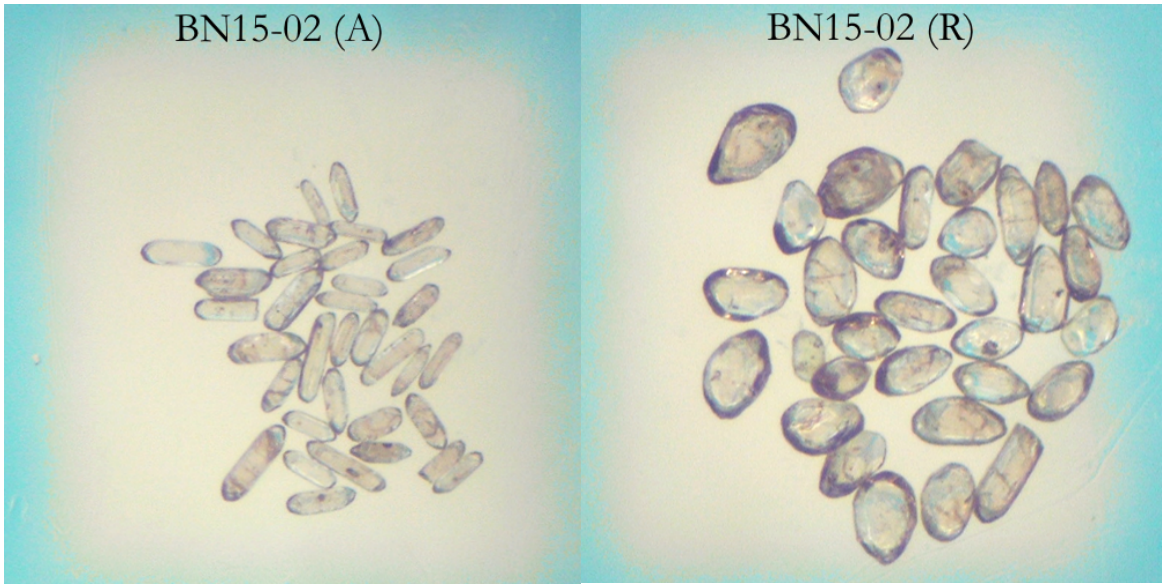

Figure 7.3: Comparison of two zircon populations seen in the biotite-gneiss I, sample BN15-02. Separated on the basis of morphological characteristics. The field of view in the pictures represent 1 mm^2, for scale. **(Left)** BN15-02 (A), prismatic, elongated and euhedral crystals. **(Right)** BN15-02 (R), large and rounded zircon grains.

7.2.3 The garnet-amphibolites

Based on the differences in appearance of the garnet-amphibolite bodies of outcrop A and outcrop C, they were sampled, described and dated separately, sample BN15-09 and sample BN15-06 respectively. According to **Winter (2010)**, garnet-amphibolites are crystalloblastic metamorphic rocks, with either a mafic igneous protolith (ortho-amphibolite) or a greywacke protolith (para-amphibolite).

The U/Pb zircon results for the garnet-amphibolite from outcrop A are discordant, but plot close to the discordia lines calculated for the data of the biotite-gneisses, suggesting a similar origin **(fig 7.4**, next page**)**. The titanite grains from the garnet-amphibolite **(457/s.49 and 457/s.56)** yields a concordia age at 1036 ± 1.8 Ma, interpreted as a metamorphic age.

The garnet-amphibolite from outcrop C **(fig 7.5,** next page**)**(sample BN15-06), lacks the old zircons seen in the BN15-09 sample. The zircons yield apparent ages c. 1030-1060 Ma, along with slightly younger rutile ages (c. 1010-1030 Ma). Titanites **(469/s.89 and 489/s.106)** yield apparent ages around 920 Ma. The apparent age derived from the zircons is interpreted to represent crystallization during a metamorphic event, and the age derived of the rutiles is interpreted to represent crystallization under retrograding metamorphic conditions. The apparent age from the titanites represent a late metamorphic event c.920 Ma that will be further investigated in subchapter **7.7**.

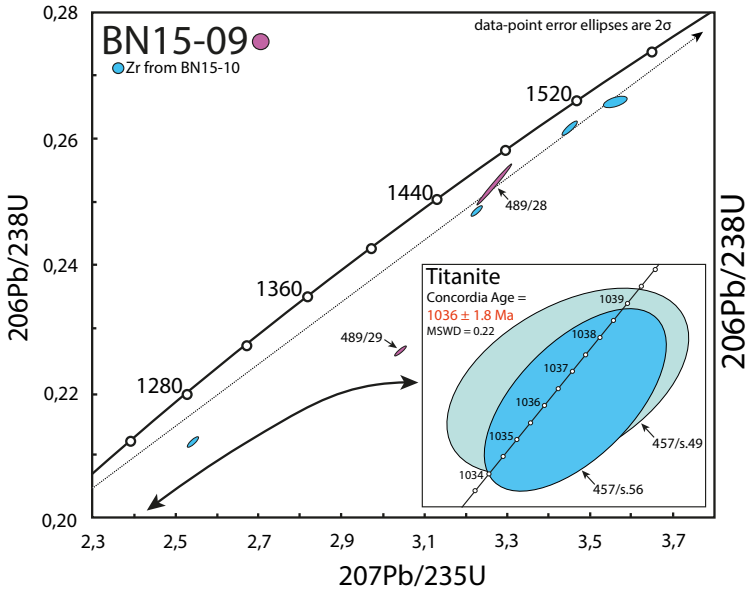

Figure 7.4: Concordia plot of results from the garnet-amphibolite in outcrop A (BN15-09). The 489/28 zircon fits a line ponting towards an old apparent age in the 1600 Ma region. **Inset figure:** Concordant age of two titanite grains from the same sample, yielding at 1036 ± 1.8 Ma, interpreted as an metamorphic age.

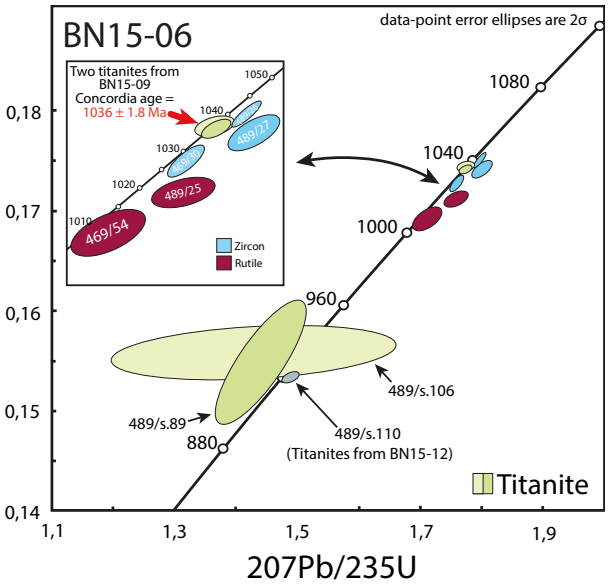

Figure 7.5: Concordia plot of results from the garnet-amphibolite in outcrop C (BN15-06). The clustering of results in the 1030-1040 Ma region is evident. **Inset figure:** zircon grains in the same sample yielding apparent ages 1030-1060 Ma, and rutile yielding apparent ages 1010-1030 Ma.

Based on the isotopic data, the possibility that the garnet-amphibolites sampled from outcrop A and C represent two separate lithologies, with different age, is certainly not excluded. But to say anything about their origin is a different exercise. If the old zircons found in the garnet-amphibolite sample from outcrop A (sample BN15-09) represents the age of formation, the rock formed in an island arc environment **(Åhäll and Connelly 2008)** close to the time of the formation of the protolithy of the biotite-gneiss. The garnet-amphibolite body sampled in outcrop A does not cut the foliation of the gneiss, but it does appear to have a steeper dip than the most of the surrounding biotite-gneiss. The geometry of the garnet-amphibolite body in outcrop A resembles a thick dyke, but without further whole-rock geochemistry no concluding remarks regarding the origin of the BN15-09 sample will be made.

The garnet-amphibolite sample from outcrop C (BN15-06), looks less internally deformed than the garnet-amphibolite from outcrop A (BN15-09). This is interpreted to be an indication that the garnet-amphibolite in outcrop C is younger. The zircons in the garnet-amphibolite sample from outcrop C (BN15-06) are interpreted to be metamorphic. Because mafic igneous rocks in general lack primary zircons, and those found tend to grow during a late metamorphism **(Kohn et al. 2015)**. The longest axis of the garnet-amphibolite bodies are oriented subparallel to the foliation of the biotite-gneiss. If the foliation is a preserved primary bedding (S_0) and the biotite-gneiss has not been extensively deformed before the intrusion, this indicates that the garnet-amphibolite sampled in outcrop C represents one of multiple sills intruding into the biotite-gneiss before c.1050-1060 Ma. A precise age for intrusion are not available in the data from this study. According to **Åhäll and Connelly (1998)** intraorogenic (pre-Sveconorwegian) magmatism was abundant and occurred episodically between 1.53 and 1.20 east of the Oslo Rift.

7.2.4 The pegmatites

The diversity in the appearance of the pegmatites and how they are related to the surrounding lithologies founded the concept of several generations of intrusions. The presumably oldest generation (gen.A, **fig 7.7**) consists of lenses within the garnet-amphibolite boudins in outcrop C. Due to their small size, any attempt at dating them were thought to be impossible with the used methods, without a large risk of contamination from the surrounding garnet-amphibolite. Therefore only pegmatite generation B, consisting of veins constrained within the northernmost rectangular boudin in outcrop C **(fig 7.8)**, and pegmatite generation C, consisting of a vein cutting through all the lithologies in the middle of outcrop C **(fig 7.9)**, were dated.

With the analysis results from zircon in sample BN15-11, pegmatite generation B, a line were fitted through the **489/52** and **489/53** zircons, giving an upper interception of concordia at 1040.7 ± 4.2 Ma. In sample BN15-12, pegmatite generation C, the calculated mean 207Pb/235U age of two monazite fractions **(489/s.104 and 489/s.105)** is 1033.2 ± 1.2 Ma. These results effectively proves the initial idea that the lithologies were intruded by pegmatite veins at multiple stages in time.

Another sample of pegmatite was analysed, sample BN15-3/4/5, consisting of three smaller specimens from a small pegmatite vein cutting through the lithologies in the southern half of outcrop C. The results from the zircon grains analyzed from this sample gives an old apparent age which can only be explained as inherited from the surrounding biotite-gneiss. A single analysis from monazite, fraction **457/s.44**, gives a concordia age of 1034 ± 6.0 Ma. This pegmatite vein is therefore considered to represent a late intrusion, and possibly simultaneous as pegmatite generation C (BN15-12).

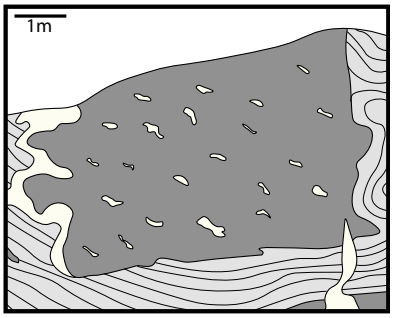

Figure 7.6: Sketch of «patch»-pegmatite constrained in a rectangular amphibolite boudin in outcrop C. Pegmatite generation A.

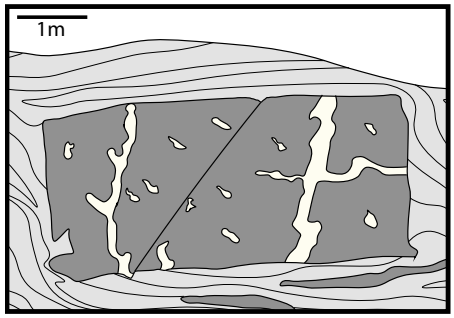

Figure 7.7: Sketch of pegmatite veins constrained in a rectangular amphibolite boudin in outcrop C. Pegmatite generation B.

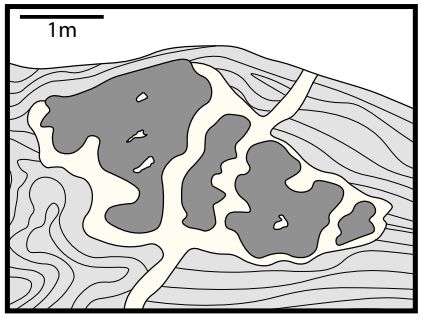

Figure 7.8: Sketch of observed pegmatite vein cutting through the lithologies in outcrop C. Pegmatite generation C.

7.3 The main metamorphic event

Indications of a major metamorphic event are evident in all analyses yielding apparent ages older than c. 1.0 Ga. As mentioned initially, all zircon analyses yielding apparent ages older than the intermediate period c.1030-1040 Ma shares the same discordant trend, which has been interpreted to relate to secondary lead loss induced by a metamorphic event. Another trend evident in the U/Pb results is the clustering of results in and around the c.1030-1040 Ma period. This is based on results derived from analyses of zircon, monazite, titanite and rutile, from both garnet-amphibolite samples (BN15-06 and BN15-09), the pegmatite generation B sample (BN15-11) and the pegmatite generation C sample(s) (BN15-12 and potentially BN15-3/4/5) **(fig 7.9)**.

The earliest evidence of this metamorphic event belongs to analyses of zircon, from the garnet-amphibolite in outcrop B **(fig 7.9B)** and the pegmatite generation B **(fig 7.9D)**, where two zircons from the pegmatite sample are fitted on a line intercepting concordia at 1040.7 ± 4.2 Ma. This pegmatite generation is constrained within the rectangular garnet-amphibolite boudins of outcrop C, hence the intrusion is pre- or syn-tectonic. The pegmatite veins referred to as generation C, cuts through both the garnet-amphibolite boudins and the surrounding biotite-gneiss matrix, hence these intrusion are interpreted as post-tectonic. A calculated mean $^{207}Pb/^{235}U$ age at 1033.2 ± 1.2 Ma is derived from two monazite grains **(489/s.104 and 489/s.105)** from the BN15-12 sample **(fig 6.8)**, which is overlapped by the concordant 1034 ± 6.0 Ma age derived from the BN15-3/4/5 sample **(fig 7.9C)**. This effectively brackets the time of the main deformation observed in the outcrops between 1040.7 ± 4.2 Ma and 1033.2 ± 1.2 Ma. In addition, a concordant age at 1036 ± 1.8 Ma is derived from two titanite grains in the garnet-amphibolite in outcrop A **(fig 7.9A)**, which could represent the age of this deformational event. At last, two rutile fractions yield slightly younger apparent ages in the BN15-06 sample, interpreted to represent crystallization during retrograde metamorphic conditions.

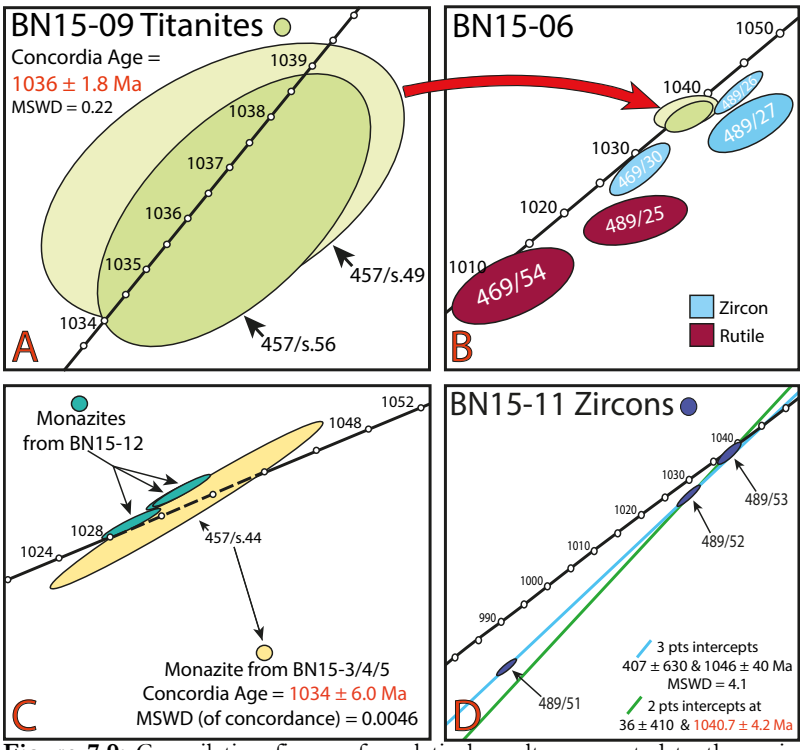

Figure 7.9: Compilation figure of analytical results connected to the main metamorphic event at c. 1030-1040 Ma. **A)** Garnet amphibolite outcrop A. **B)** Garnet-amphibolite outcrop C. **C)** Pegmatite gen. B. **D)** Pegmatite gen. C.

In a four phase model perspective **(Bingen et al. 2008b)**, this major metamorphic event, occured during a period considered as the main period of Sveconorwegian orogenesis, known as the Agder phase (1050-980 Ma). This phase is believed to result from continent - continent collision between Fennoscandia and possibly Amazonia, with crustal thickening in the center of the orogen. This led to deformation, metamorphism and magmatism in the Iddefjord (and Telemarkia) Terrane. The Iddefjord Terrane was at this point underthrust and buried to depths of at least 35km, resulting in high grade amphibolite- to granulite-facies metamorphism **(Bingen et al. 2008b)**.

7.4 Late metamorphic event

A late metamorphic event was associated with titanite crystallization around 920 Ma, seen in sample BN15-06 (garnet-amphibolite in section C) and sample BN15-12 (pegmatite gen. C). This age corresponds to the time of formation of the larger Bohus-pluton (Iddefjord granite), not far south of the outcrops. This event may have driven some fluids into the system, leading to the crystallization of titanite.

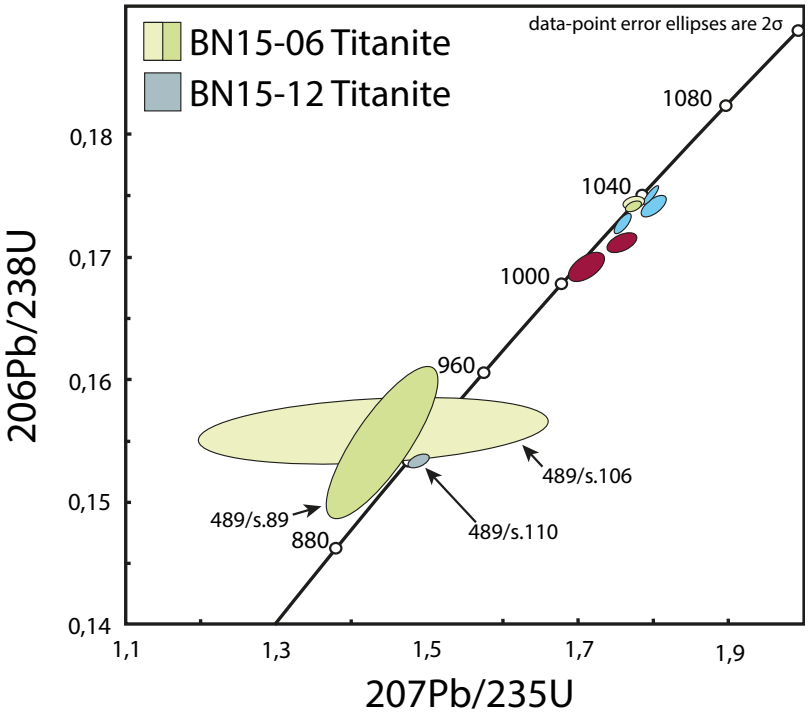

Figure 7.10: Titanite crystallization c.920 Ma. Fraction 489/s.89 and 489/s.106 from garnet-amphibolite in outcrop C (BN15-06). Fraction 489/s.110 from pegmatite generation C (BN15-12).

7.5 Structural interpretations

7.5.1 Shear-zones

The entire roadcut (outcrop A, B and C), is a large, relatively homogenous shear-zone. It includes, however, cm- to meter-scale tabular high-strain with characteristics suggesting formation under different pressure and temperature conditions **(figure 5.21 in chapter 5.3)**. The tabular ductile high-strain zones dipping towards north are interpreted to be oldest **(fig 5.21A)** while the semi-ductile cm-sale tabular high-strain zones of variating orientation **(fig 5.21B)**, are interpreted to be younger.

7.5.2 Small macroscopic shear indicators

The ductile tabular high-strain zones contain relict minerals that survived the shearing and reduction in grain size (porphyroclasts), S-C tectonites, and minerals indicating growth related to the metamorphism and deformation (porphyroclasts). These small macroscopic shear indicator displays a polarity in shear-sense, which may be explained by sub-simple shear. Porphyroblasts were also observed in the garnet-amphibolites, as garnets. These contain trains of quartz and opaque minerals likely relict from a initial foliation rather than indicating shear sense **(Twiss and Moores, 2006)**

7.5.3 Fold populations

The fold-populations outlined in the description chapter, FA & FB are interpreted to be a part of the large homogeneous shear-zone of which the outcrops represents a part of. The FA population, top-towards-north-contraction (fold axis 318-322° NW) contain parasitic folds whose asymmetry may be inverted around the larger folds **(Carreras et al. 2005)**. The FB population, consisting of disharmonic neck folds, was likely contemporaneous with the FA-population, but they were also effected by the stress-shadows formed along at the short edges of the larger garnet-amphibolite boudins, and possibly the relative movement of the boudin as well **(fig 7.11)**

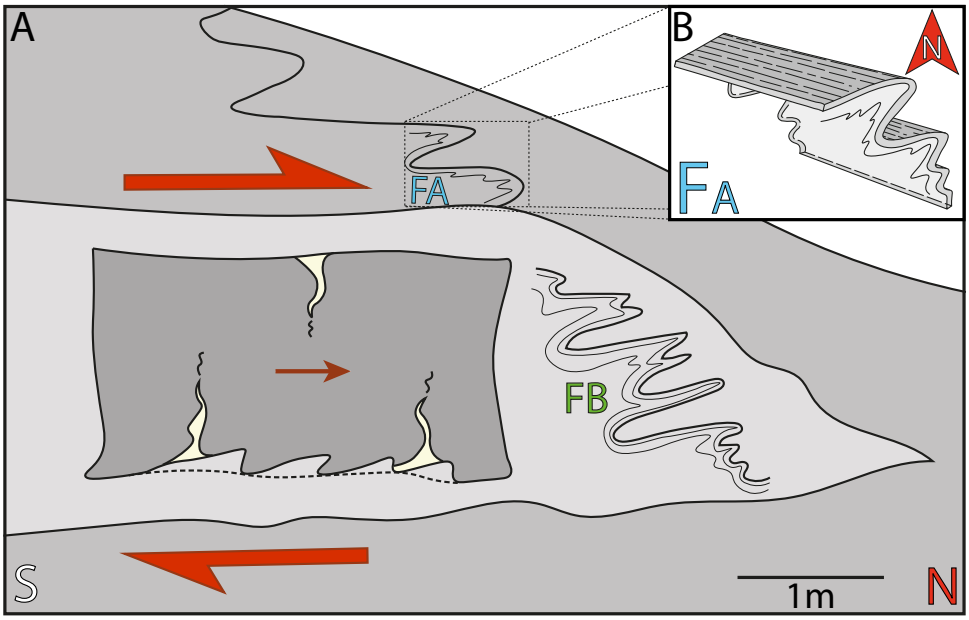

Figure 7.11: A) Conceptual sketch showing the relation between the two outlined fold-populations. The folds indication top-towards-north contraction underneath the rectangular boudin have an exaggerated amplitude. **B)** Close-up sketch of fold-population Fa.

7.5.4 Boudins

Garnet-amphibolite boudins are observed with a diversity of geometries in the outcrops, from rectangular to lozenge-shaped, exemplified in outcrop C **(fig 5.28, subchapter 5.3.5).** These differences in geometry are probably related to differences in mechanical strength due to contrasting primary thickness of the sills. The rectangular boudins, which measure 8x4 and 6x2.5 meters, were likely derived from thick (mechanically stronger) layers, which deformed dominantly by a brittle component when exposed to extension **(Ramsey et al. 1987)(fig 7.12)**. Several premature extensional fractures can be seen along the long-side of the rectangular boudins, indicating that if the extension had pursued we could have expected a higher frequency of boudins of reduced size. The strained lozenge-shaped garnet-amphibolite boudins were likely derived from a thinner (mechanically weaker) sills. The layer most likely split up upon initial extension and deformed with a greater component of visco-plasticity **(Ramsey et al. 1987)(fig 7.12)**.

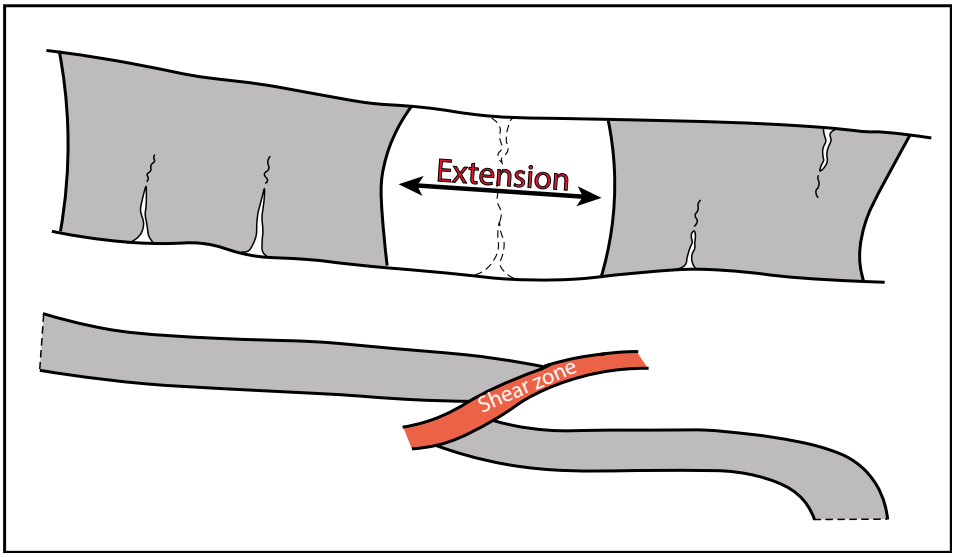

Figure 7.12: Conceptual sketch of the sills response to extension base on their primary thickness/mechanically strength, as observed in the outcrops. **(Top)** Thick mechanically strong sill. **(Bottom)** Thin mechanically weak(er) sill.

7.5.5 Faults

The faults observed represents the shallow part of the deformation history, with cores dominated by ultracataclasites to fault gouge fault rocks. Meaning burial depth at the time of faulting was less than c. 12 km, also known as the boarder between ductile and brittle deformation mechanisms. This is not synonymous with a young age, because some of the faults may very well be of Proterozoic age. The width of brittle shear-zones increase with depth **(Twiss and Moores, 2006)**, hence the fault-core containing an ultracataclasite (sample BN15-08) in outcrop A, likely is the oldest fault. To prove that faults of Proterozoic age were found in the roadcut, a zircon were analysed from the ultracataclasite. Unfortunately the zircons analysed, **469/28**, yielded an apparent age at c.1360-1470 Ma, which fits to the general trend of the old zircons derived from the biotite-gneiss, hence the age is inherited from the surrounding rock. Never the less, thin-section studies showed that the fault has had at least three episodes of movement. The old normal-faults observed in the outcrops, with a cores dominated by cohesive fault-rocks, seems to represent a gently rotated conjugate fault-set oriented close to W-E.

The faults with cores dominated by a fault-gouge, could be as young as Quaternary, and with that represents the youngest structures pointed out in the outcrops.

7.6 Regional implications

Extensive published data from south Norway and southwest Sweden **(i.e Berthelsen 1980, Åhäll et al 1998 and Andersen et al. 2004)** suggests that the western margin of the Baltican Shield was the site of a long lived active margin with continuous magmatism in the period c.1.66-1.50, Gothian magmatism and metamorphism. Both the protolith ages (zircon; 1600-1660 Ma) and metamorphic age (monazite; 1554 ± 11 Ma) for the biotite gneisses fall within this period, and the monazites are coeval with the last stage of the 1.55-1.52 Hisingen magmatism **(map; figure 2.4)(Åhäll and Connelly, 2008)** and several near coeval units in the SSD.

During the 1.15 - 0.9 Ga Sveconorwegian the SSD were extensively deformed, and referring to earlier discussion, the majority of the deformation observed were formed during this event. According to **Bingen et al. (2008)** the Iddefjorden Terrane displays a general NS to NW-SE structural grain, and contains several orogen-parallel shear-zones, and the outcrops likely represents one of these structures. Its dated at c. 1035 Ma in this study (last movement), similar in age to other Sveconorwegain shear zones, i.e Mandal-Ustaoset shear zone **(Bingen and van Breemen, 1998)**.

The emplacement of the different pegmatite generations between c.1040 - 1030 Ma, are not to different in age to pegmatite veins dated at the Nesodden Peninsula by **Bue (2008)**, where one of the pegmatite samples yielded a calculated concordia age at 1051 ± 5 Ma, possibly reflecting anatexis of the gneisses.

7.7 Time-pressure/temperature-strain history

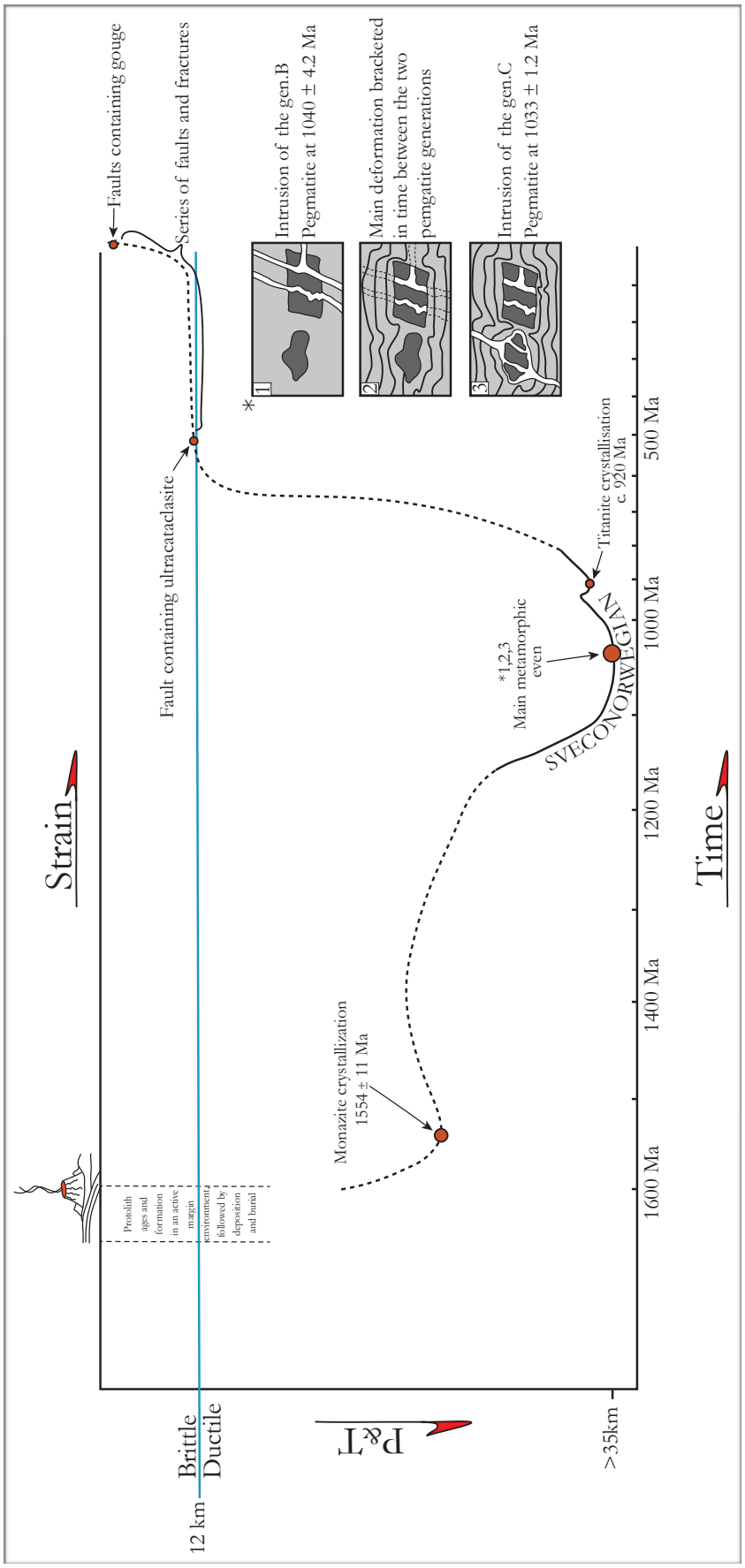

Figure 7.13: Summarizing graph displaying the results and how the interpretations could relate. Note, this is no blueprint, only a thought path between the three points of deformation (1554 ± 11 Ma, c.1040-1030 Ma event and 920 Ma event) derived from the analyses. The depth of the main event is interpreted from **(Bingen et al. 2008b)**.

Chapter 8: Conclusions

- The biotite-gneisses are likely of supracrutal origin, derived from protoliths with a restricted range of ages c. 1.66-1.60 Ga. It formed in the active continental arc setting of the Le-Marstrand belt, and underwent metamorphism resulting in monazite crystallization at 1554 ± 11 Ma.

- The garnet-amphibolite in outcrop A contains ca. 1.6 Ga zircon, pointing towards a formation coeval with, and by the same processes as the biotite-gneiss.

- The garnet-amphibolite boudins in outcrop B, originated as multiple sills that intruded into the rocks before c. 1040 Ma. The sills reacted differently upon deformation as a result of distinct individual mechanical strengths, hence differences in geometries are seen.

- Individual stages of pegmatite intrusions have been proven, as pegmatite generation B formed at 1040.7 ± 4.2 Ma and pegmatite generation C at 1033.2 ± 1.2 Ma.

- The main deformation is bracketed between the two pegmatite generations, based on field relations and isotope data. A concordant age for titanite crystallization in the garnet-amphibolite in outcrop A, at 1036 ± 1.8 Ma, likely represents this event. During this period the rocks were buried to at least 35 km **(Bingen et al. 2008b)**, during the Agder Phase.

- Rutile crystallization at 1010-1020 Ma recorded in the garnet-amphibolite boudins indicates formation during retrograde metamorphism.

- Titanite crystallization at c. 920 Ma reflect secondary processes, likely connected to emplacement of the Bohus-pluton.

- Faults represent the youngest outlined structures. The ones containing cohesive fault rocks may be of Proterozoic age, while the faults containing a gouge likely represents structures of Quaternary age.

Bibliography

ANDERSEN, T., GRIFFIN, W. L., JACKSON, S. E., KNUDSEN, T. L. & PEARSON, N. J. 2004. Mid-Proterozoic magmatic arc evolution at the southwest margin of the Baltic Shield. *LITHOS,* 73**,** 289-318.

ANDERSEN, T. 2005. Terrane analysis, regional nomenclature and crustal evolution in the Southwest Scandinavian Domain of the Fennoscandian Shield. *GFF,* 127**,** 159-168.

ANDERSSON, M., LIE, J. E. & HUSEBYE, E. S. 1996. Tectonic setting of post-orogenic granites within SW Fennoscandia based on deep seismic and gravity data. *Terra Nova,* 8**,** 558-566.

ASGER, B. 1980. Towards a palinspastic tectonic analysis of the Baltic Shield. Collogue C6: Géologie de l'Europe du Précambrien aux Bassins sédimemairespost-hercyniens**,** 5-21.

AUGLAND, L. E. & UNIVERSITETET I OSLO INSTITUTT FOR, G. 2012. Intercontinental interactions between Baltica and Laurentia : terrane identifications and correlations in the Caledonides. no. 1150, Department of Geosciences, Faculty of Mathematics and Natural Sciences, University of Oslo.

BERTHELSEN, A. 1980. Towards a palinspastic tectonic analysis of the Baltic Shield. Collogue C6: Géologie de l'Europe du Précambrien aux Bassins sédimemairespost-hercyniens**,** 5-21.

BERTHELSEN, A., OLERUD, S. & SIGMOND, E. M. O. 1996. Geologisk kart over Norge, berggrunnskart OSLO 1:250000. *Norges geologiske undersøkelse.*

BINGEN, B. & VAN BREEMEN, O. 1998. Tectonic regimes and terrane boundaries in the high-grade Sveconorwegian belt of SW Norway, inferred from U-Pb zircon geochronology and geochemical signature of augen gneiss suites. *J. Geol. Soc.,* 155**,** 143-154.

BINGEN, B., ANDERSSON, J., SOEDERLUND, U. & MOELLER, C. 2008**c**. The Mesoproterozoic in the Nordic countries - The Mesoproterozoic in the Nordic countries. *Episodes,* 31**,** 29-34.

BINGEN, B., DAVIS, W., HAMILTON, M. A., ENGVIK, A., STEIN, H., SKAR, O. & NORDGULEN, O. 2008**a**. Geochronology of high-grade metamorphism in the Sveconorwegian belt, S. Norway: U-Pb, Th-Pb and Re-Os data. *Norw. J. Geol.*

BINGEN, B., NORDGULEN, O. & VIOLA, G. 2008**b**. A four-phase model for the Sveconorwegian orogeny, SW Scandinavia. *Norw. J. Geol.*

BINGEN, B., SKAR, O., MARKER, M., SIGMOND, E., NORDGULEN, O., RAGNHILDSTVEIT, J., MANSFELD, J., TUCKER, R. D. & LIEGEOIS, J. P. 2005. Timing of continental building in the Sveconorwegian orogen, SW Scandinavia. *Norw. J. Geol.*

BREWER, T. S., DALY, J. S. & ÅHÄLL, K.-I. 1998. Contrasting magmatic arcs in the Palaeoproterozoic of the south-western Baltic Shield. *Precambrian Research,* 92**,** 297-315.

BRAATHEN, A., OSMUNDSEN, P. T. & GABRIELSEN, R. H. 2004. Dynamic development of fault rocks in a crustal-scale detachment: An example from western Norway. *Tectonics,* 23**,** 1-21.

BUE, E. P. 2008. Age and origin of the Mesoproterozoic basement of the Nesodden Peninsula, SE Norway : a geochronological and isotopic study. Oslo: E.P. Bue.

CARRERAS, J., DRUGUET, E. & GRIERA, A. 2005. Shear zone-related folds. *Journal of Structural Geology,* 27**,** 1229-1251.

CHERNIAK, D. J. & WATSON, E. B. 2003. Diffusion in Zircon. *Reviews in Mineralogy and Geochemistry,* 53**,** 113-143.

CORFU, F., HANCHAR, J. M., HOSKIN, P. W. O. & KINNY, P. 2003. Atlas of Zircon Textures. *Reviews in Mineralogy and Geochemistry,* 53**,** 469-500.

DAVIS, D. W., KROGH, T. E. & WILLIAMS, I. S. 2003. Historical Development of Zircon Geochronology. *Reviews in Mineralogy and Geochemistry,* 53**,** 145.

FAURE, G. & MENSING, T. M. 2005. Isotopes: principles and applications, New York,Wiley.

FOSSEN, H. 2010. *Structural geology,* Cambridge, Cambridge University Press.

GORBATSCHEV, R. & BOGDANOVA, S. 1993. Frontiers in the Baltic Shield. *Precambrian Research,* 64**,** 3-21.

GRAVERSEN, O. 1973. Structural interpretation of a double-folded gneiss-amphibolite sequence, Bunnefjorden, Akershus. *Bulletin. Norges geologiske undersøkelse,* 300**,** 73-82.

GRAVERSEN, O. & PEDERSEN, S. 1999. Timing of Gothian structural evolution in SE Norway: A Rb-Sr whole-rock age study. *Norsk Geologisk Tidsskrift,* 79**,** 47-56.

GAÁL, G. & GORBATSCHEV, R. 1987. An Outline of the precambrian evolution of the baltic shield. *Precambrian Research,* 35**,** 15-52.

HARRISON, T. M., CATLOS, E. J. & MONTEL, J.-M. 2002. U-Th-Pb Dating of Phosphate Minerals. *Reviews in Mineralogy and Geochemistry,* 48**,** 524-558.

HÖGDAHL, K., ANDERSSON, U. & EKLUND, O. 2004. The Transscandinavian Igneous Belt: a review. *Geol Surv Finland Sp Papers,* 37.

KOHN, M. J., CORRIE, S. L. & MARKLEY, C. 2015. The fall and rise of metamorphic zircon. *American Mineralogist,* 100**,** 897-907.

KOOIJMAN, E., MEZGER, K. & BERNDT, J. 2010. Constraints on the U–Pb systematics of metamorphic rutile from in situ LA-ICP-MS analysis. *Earth and Planetary Science Letters,* 293**,** 321-330.

KROGH, T. E. 1973. A low-contamination method for hydrothermal decomposition of zircon and extraction of U and Pb for isotopic age determinations. *Geochimica et Cosmochimica Acta,* 37**,** 485-494.

KROGH, T. E. 1982. Improved accuracy of U-Pb zircon ages by the creation of more concordant systems using an air abrasion technique. *Geochimica et Cosmochimica Acta,* 46**,** 637-649.

LAHTINEN, R. 2012. Main Geological Features of Fennoscandia. *Geological Survey of Finland, Special Paper,* 53**,** 13-18.

LARSSON, W. 1956: Beskrivning til kartbladet Vårvik. Berggrunden. *Sver. geol. Unders. Ser. A,* 187: 10-127.

LUNDEGÅRDH, P. H. 1958: Goteborgstraktens berggrund. *Sver. geol. Unders. Ser. C,* 553.

MATTINSON, J. M. 2005. Zircon U–Pb chemical abrasion ("CA-TIMS") method: Combined annealing and multi-step partial dissolution analysis for improved precision and accuracy of zircon ages. *Chemical Geology,* 220**,** 47-66.

MÖLLER, C., BINGEN, B., ANDERSSON, J., STEPHENS, M. B., VIOLA, G. & SCHERSTÉN, A. 2013. A non-collisional, accretionary Sveconorwegian orogen – Comment. *Terra Nova,* 25**,** 165-168.

PARRISH, R. R., PARRISH, R. R. & NOBLE, S. R. 2003. Zircon U-Th-Pb Geochronology by Isotope Dilution — Thermal Ionization Mass Spectrometry (ID-TIMS). *Reviews in Mineralogy and Geochemistry,* 53**,** 183.

PHILPOTTS, A. R. & AGUE, J. J. 2009. Principles of igneous and metamorphic petrology, Cambridge, Cambridge University Press.

RAMSAY, J. G. 1967. Folding and fracturing of rocks, New York, McGraw-Hill.

RAMSAY, J. G., HUBER, M. I. & LISLE, R. J. 1987. The techniques of modern structural geology : Vol. 2 : Folds and fractures, London, Academic Press.

ROBERTS, N. M. W. & SLAGSTAD, T. 2015. Continental growth and reworking on the edge of the Columbia and Rodinia supercontinents; 1.86–0.9 Ga accretionary orogeny in southwest Fennoscandia. *International Geology Review,* 57**,** 1582-1606.

SCHOENE, B. 2014. 4.10-U–Th–Pb Geochronology. Treatise on Geochemistry, Second Editionth edn. Elsevier, Oxford**,** 341-378.

SKJERNAA, L. & PEDERSEN, S. 1982. The effects of penetrative Sveconorwegian deformations on Rb/Sr isotope systems in the Römskog-Aurskog-Höland Area, SE Norway. *Precambrian Research,* 17**,** 215-243.

SLAGSTAD, T., ROBERTS, N. M. W., MARKER, M., RØHR, T. S. & SCHIELLERUP, H. 2013. A non-collisional, accretionary Sveconorwegian orogen. *Terra Nova,* 25**,** 30-37.

SPEAR, F. S. & PYLE, J. M. 2002. Apatite, Monazite, and Xenotime in Metamorphic Rocks. *Reviews in Mineralogy and Geochemistry,* 48**,** 293-335.

STEIGER, R. H. & JÄGER, E. 1977. Subcommission on geochronology: Convention on the use of decay constants in geo- and cosmochronology. *Earth and Planetary Science Letters,* 36**,** 359-362.

TWISS, R. J. & MOORES, E. M. 2006. *Structural Geology*, New York, W. H. Freeman.

VIOLA, G., HENDERSON, I., BINGEN, B. & HENDRIKS, B. 2011. The Grenvillian–Sveconorwegian orogeny in Fennoscandia: Back-thrusting and extensional shearing along the "Mylonite Zone". *Precambrian Research,* 189**,** 368-388.

WAHLGREN, C.-H., CRUDEN, A. R. & STEPHENS, M. B. 1994. Kinematics of a major fan-like structure in the eastern part of the Sveconorwegian orogen, Baltic Shield, south-central Sweden. *Precambrian Research,* 70**,** 67-91.

WETHERILL, G. W. 1956. Discordant uranium-lead ages, I. *Eos, Transactions American Geophysical Union,* 37**,** 320-326.

WINTER, J. D. 2010. Principles of igneous and metamorphic petrology, New York, Prentice Hall.
ÅHÄLL, K.-I. & CONNELLY, J. N. 2008. Long-term convergence along SW Fennoscandia: 330 m.y. of Proterozoic crustal growth [Precam Res 161 (2008) 452–472]. *Precambrian Research,* 163**,** 402-421.

ÅHÄLL, K.-I., PERSSON, P.-O. & SKIÖLD, T. 1995. Westward accretion of the Baltic Shield: implications from the 1.6 GaÅmål-Horred Belt, SW Sweden. *Precambrian Research,* 70**,** 235-251.

ÅHÄLL, K. I. & DALY, J. S. 1989. Age, tectonic setting and provenance of Östfold-Marstrand Belt Supracrustals: Westward crustal growth of the Baltic Shield at 1760 Ma. *Precambrian Research,* 45**,** 45-61.

Appendix A

Pictures of all analysed fractions of grains in the study, corresponding to **table 6.1** in the U/Pb-cronology results chapter. All pictures corresponds to 1x1 millimeter, except one picture of a rutile fraction from sample BN15-06. In this picture the millimeter paper in the back can be used for scale.

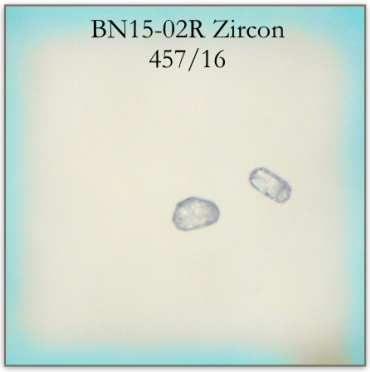

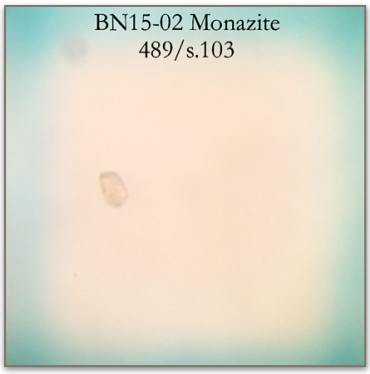

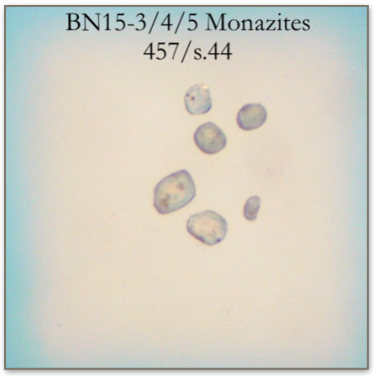

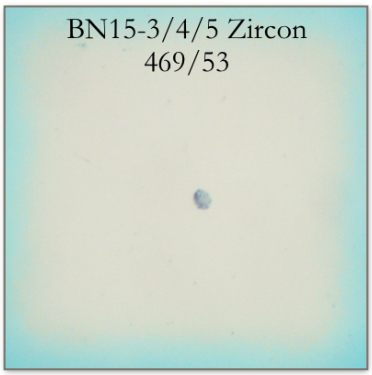

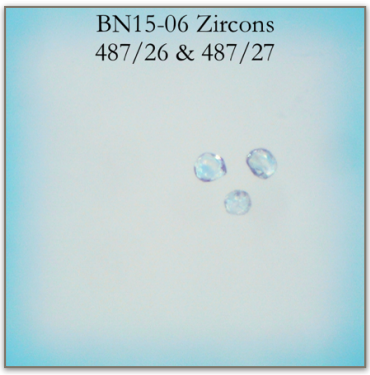

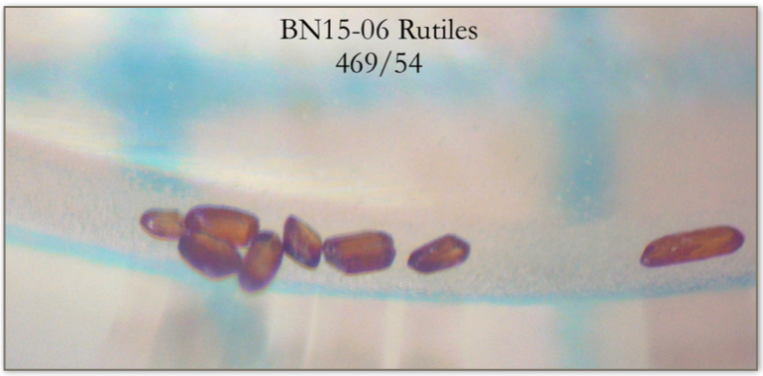


BN15-07 Zircons
469/25 & 469/26

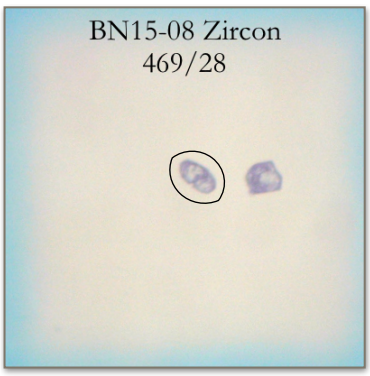
BN15-08 Zircon
469/28

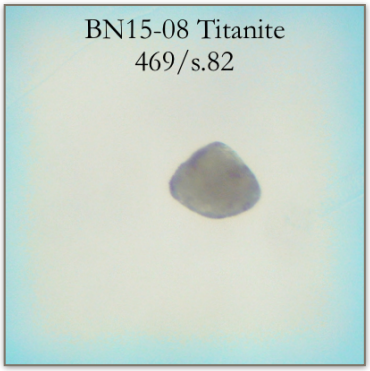
BN15-08 Titanite
469/s.82

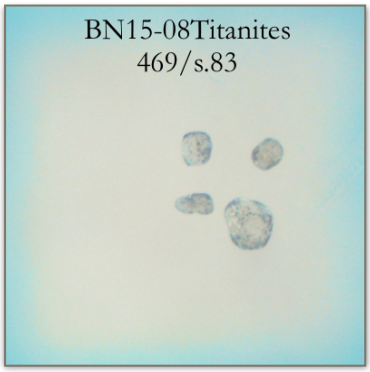
BN15-08Titanites
469/s.83

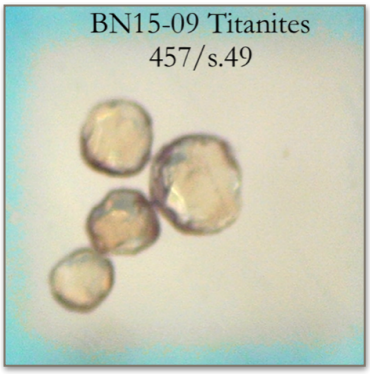
BN15-09 Titanites
457/s.49


BN15-09 Titanites
457/s.56


BN15-09 Zircons
489/28 & 489/29


BN15-10 Zircons
457/19 & 457/20

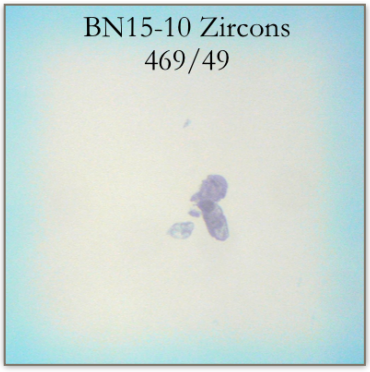
BN15-10 Zircons
469/49

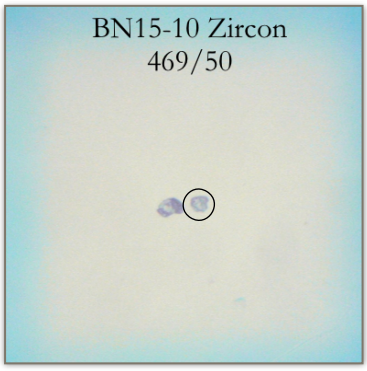
BN15-10 Zircon
469/50


BN15-11 Zircons
489/51, 489/52 & 489/53

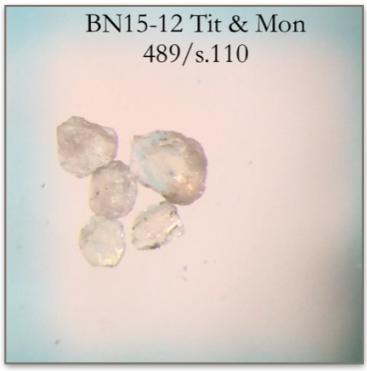
BN15-12 Tit & Mon
489/s.110


BN15-12 Monazites
489/s.104 & 489/s.105

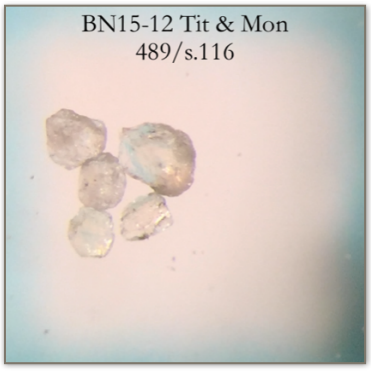
BN15-12 Tit & Mon
489/s.116

Appendix B

Scans of the thin sections investigated in the study.

Biotite-gneiss I
BN15-02

Garnet-amphibolite
BN15-06

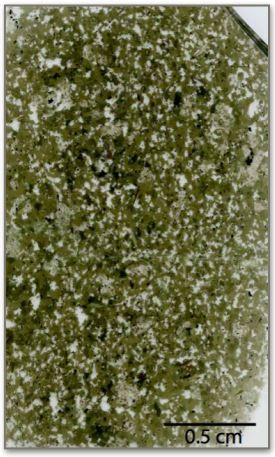

Ultracataclasite
BN15-08

Garnet-amphibolite
BN15-09

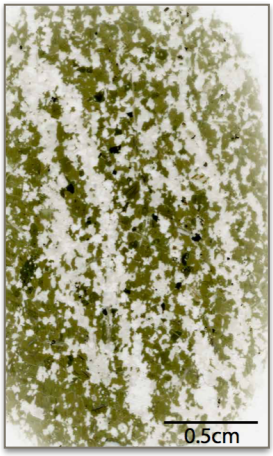

Biotite-gneiss II
BN15-10

Pegmatite gen B
BN15-11

Pegmatite gen. C
BN15-12

Pegmatite gen. A
BN15-13

Appendix C

The locations of key structures or elements presented in the lithological description, subchapter 5.2, and the structural description, subchapter 5.3.

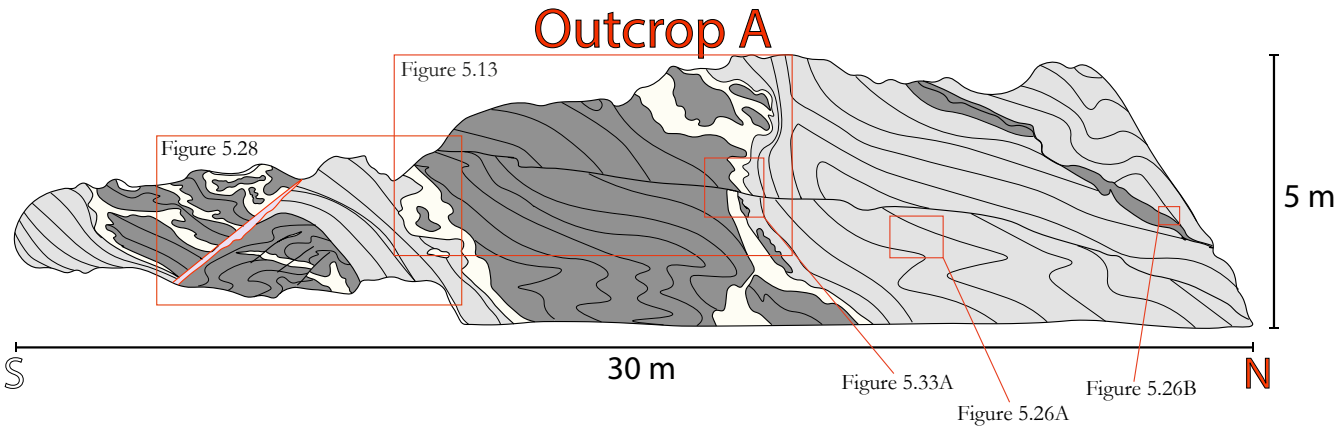

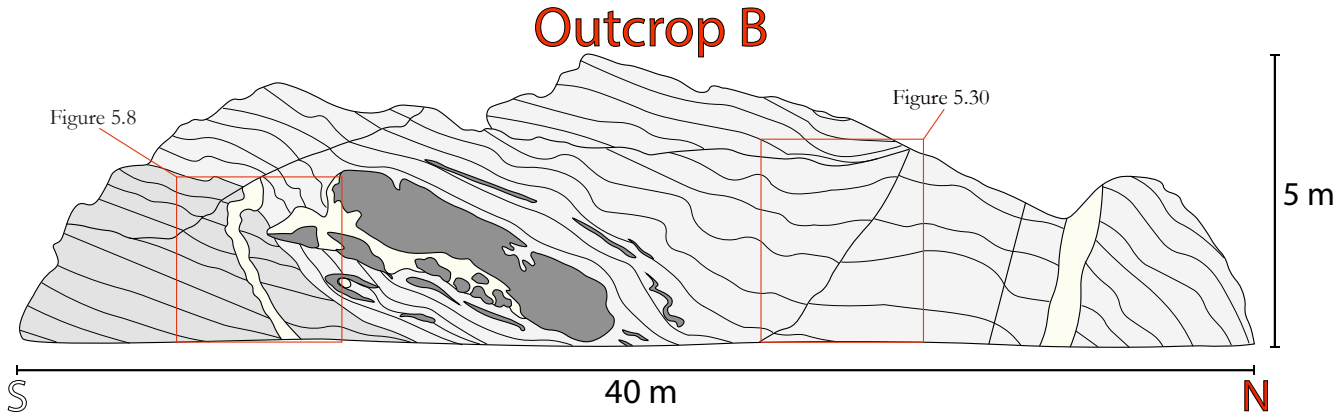

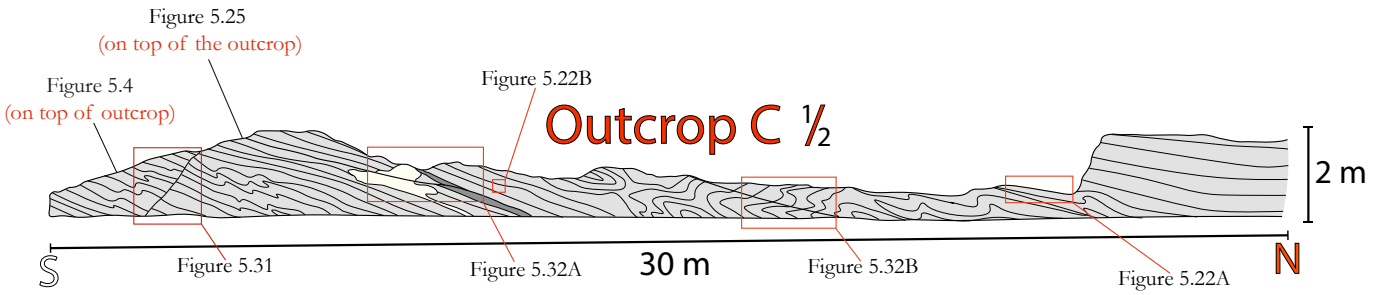

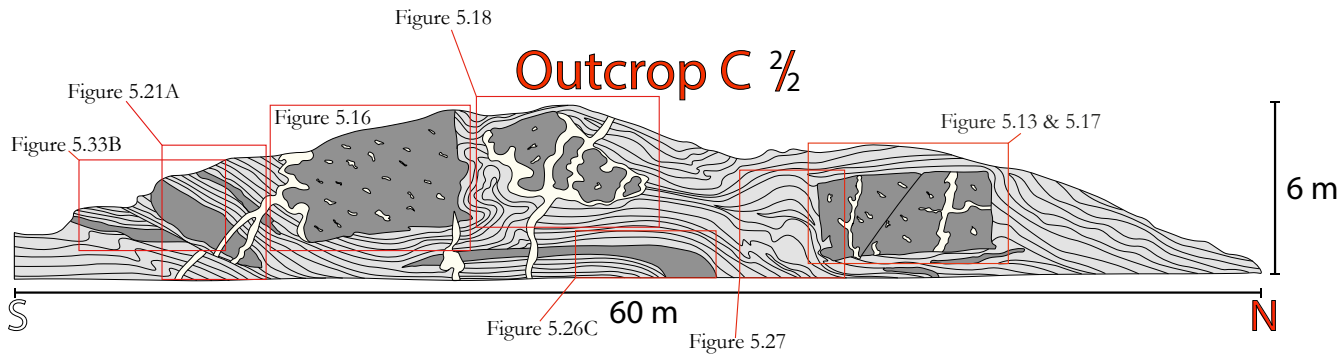

Appendix D

Overview of the field area